uOttawa

L'Université canadienne
Canada's university

FACULTÉ DES ÉTUDES SUPÉRIEURES ET POSTOCTORALES

uOttawa

L'Université canadienne
Canada's university

FACULTY OF GRADUATE AND POSDOCTORAL STUDIES

Igor Acimovic

AUTEUR DE LA THÈSE / AUTHOR OF THESIS

M.A.Sc. (Electrical Engineering)

GRADE / DEGREE

School of Information Technology and Engineering

FACULTÉ, ÉCOLE, DÉPARTEMENT / FACULTY, SCHOOL, DEPARTMENT

Improving Port Isolation in Dual-Polarized Microstrip Patch Antenna Arrays

TITRE DE LA THÈSE / TITLE OF THESIS

D. McNamara

DIRECTEUR (DIRECTRICE) DE LA THÈSE / THESIS SUPERVISOR

CO-DIRECTEUR (CO-DIRECTRICE) DE LA THÈSE / THESIS CO-SUPERVISOR

EXAMINATEURS (EXAMINATRICES) DE LA THÈSE / THESIS EXAMINERS

M. Yagoub

A. Petosa

Gary W. Slater

Le Doyen de la Faculté des études supérieures et postdoctorales / Dean of the Faculty of Graduate and Postdoctoral Studies

Improving Port Isolation in Dual-Polarized Microstrip Patch Antenna Arrays

by

Igor Acimovic, B. A. Sc.

A thesis submitted to the
Faculty of Graduate and Postdoctoral Studies
in partial fulfillment of the requirements for the degree of

Master of Applied Science
in Electrical Engineering

Ottawa-Carleton Institute for Electrical and Computer Engineering
School of Information Technology and Engineering
Faculty of Engineering
University of Ottawa

Aug 31, 2006

Your file Votre référence
ISBN: 978-0-494-25736-4
Our file Notre référence
ISBN: 978-0-494-25736-4

"I do not think there is any thrill that can go through the human heart like that felt by the inventor as he sees some creation of the brain unfolding to success. ..."

(Nikola Tesla, 1856 - 1943)

Abstract

In this thesis we present the design techniques mitigating the port isolation degradation in dual-polarized microstrip arrays. The advantages of using dual-polarized antennas are the frequency band reuse and simultaneous receive/transmit capability. To fully exploit these advantages the isolation between orthogonally polarized ports must be maximized and radiation cross-polarization minimized.

To prevent the port isolation degradation due to presence of the feed network lines surrounding the radiator the "folded" feed optimized to maximize the port isolation is introduced. The analysis of the port isolation dependence on radiating element positioning and grouping as well as the layout of the non-mirrored sections of the feed network within the array is performed. Based on the design guidelines introduced in this thesis the 4x4 element dual-polarized microstrip patch array was manufactured and port isolation in excess of 40dB was measured over the impedance bandwidth. The effects of excitation amplitude taper and excitation phase progression on port isolation performance of the array are examined and the results presented.

Publications

- I. Acimovic, D. M^{c}Namara, A. Petosa, "Mitigating the Port Isolation Degradation due to Feed Network Routing in Dual-Polarized Microstrip Antenna Arrays", 2006 IEEE AP-S International Symposium with Radio Science and AMEREM Meetings, Albuquerque, New Mexico, USA. July 2006

Acknowledgements

I owe gratitude to a number of people whose contributions were essential to the success of this research project.

First I would like to thank my thesis supervisor Dr. Derek McNamara for all the support with the research project and his excellent teaching of electromagnetic theory which played a key role in my choosing of this fascinating field of study.

My gratitude goes to Dr. Aldo Petosa, Dr. Apisak Ittipiboon, and Mr. Soulideth Thirakoune from the Communication Research Centre (CRC) for suggesting an interesting topic, for their theoretical and practical feedback on my research and for their material and technical support. Without them it would be impossible to translate the theoretical and simulation aspects of the project into an actual physical antenna.

I would like to thank my friend and colleague Paul Salem who has played the devil's advocate in many discussions on the subject; the discussions which made the two years of research truly enjoyable and provided valuable insights during the design project. One could not wish for a better research partner.

A well deserved thanks goes to Mr. Alain Le Hénaff without whose laboratory support the measured results for this project would be nonexistent.

Finally I would like to thank my brother and my parents for the inspiration, encouragement and support. You made all this possible.

Contents

Table of Figures

Chapter 1

Introduction

1.1 Introductory Remarks

A dual-polarized antenna is a two-port device capable of radiating orthogonally-polarized electromagnetic waves. We will be focusing on dual-polarized antennas that radiate orthogonally-polarized electromagnetic waves in the same frequency band. The advantages of dual-polarized antennas are the frequency band reuse and simultaneous receive/transmit capability (Figure 1). The two links in Figure 1a and Figure 1b are orthogonally-polarized.

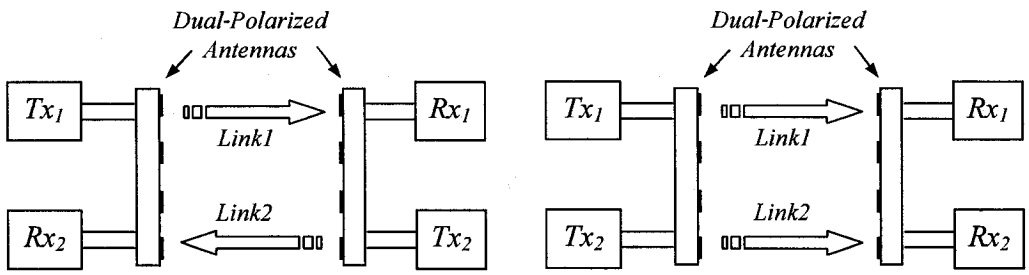

a) Simultaneous transmit/receive b) Frequency band reuse

Figure 1 Simultaneous transmit/receive and frequency band reuse capabilities of dual-polarized antennas

The two ports of a dual-polarized antenna are mutually isolated, and the level of the port isolation is obtained from scattering parameters (Figure 2).

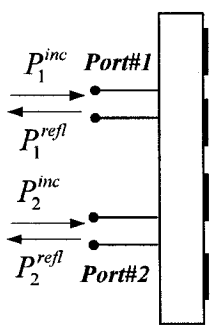

$$Isolation = -10\log\left(\frac{P_2^{refl}}{P_1^{inc}}\right)_{P_2^{inc}=0} = -20\log|S_{21}|$$

P^{inc} – *Power incident on a port*

P^{refl} – *Power leaving a port*

Figure 2 Dual-polarized antenna diagram and the port isolation definition

Dual-polarized antennas with high port isolation and low cross-polarization are self-duplexing/diplexing and as such do not require duplexers/diplexers. The polarization orthogonality of the radiated waves enables us to discriminate the orthogonally-polarized signals even though they share the same frequency spectrum thus making dual-polarized antennas instrumental in spectrum reuse. Dual-polarized antennas would provide doubling in the available channel capacity if only we could achieve perfect polarization orthogonality of the two signals transmitted/received. The difficulties in achieving perfect orthogonality preclude us from achieving full doubling of the channel capacity; however with a decrease in cross-polarization levels of the antenna we can achieve an increase in the channel capacity that comes close to doubling of the channel capacity. When the simultaneous transmit/receive capability of the dual-polarized antenna is employed to double the channel capacity the port isolation becomes critically important. If the port isolation is not sufficiently high the transmitter signal leakage will desensitize the receiver and thus disrupt the receive link. In this thesis we will focus on dual-polarized rectangular microstrip patch antennas with high port isolation. The microstrip patches will be excited using two separate feed mechanisms: the edge-coupled feed and the aperture-coupled feed. We exclusively used the corporate (parallel) feed network architecture in the design of our array antenna since it facilitates the implementation of excitation amplitude taper and phase progression, which in turn permit beam shaping, sidelobe suppression and beam squinting.

1.2 Thesis Overview

Dual-polarized antennas with their spectrum reuse capability that is achieved through use of orthogonally-polarized radiation can offer significant increase in spectral efficiency. They can obviate the need for a separate antenna for each polarization, thus providing savings in the space required, reducing weight, and reducing cost. The task at hand was to design a dual-polarized microstrip patch antenna with port isolation high enough to help prevent desensitization of the receiver in the case of simultaneous transmission and reception. In our case the port isolation of 40dB was deemed sufficient in conjunction with other measures to provide sufficient transmitter interference suppression implemented between the receiver and the antenna, and within the receiver itself.

Chapter 2 of the thesis contains a classification of the dual-polarized microstrip patch feeding mechanisms, two of which will be used in the design of our antenna. A short overview of the existing dual-polarized microstrip patch antenna designs (a single patch radiating elements and the arrays of patch radiating elements) with references to specific implementations and performances achieved is provided. The antenna geometries are presented in the order of the increasing feed design complexity as the antenna designers strived to attain the balance between the high port isolation performance and good cross-polarization performance.

In Chapter 3 we will discuss a design of a single dual-polarized microstrip patch radiator. Three layouts for the horizontal edge-coupled feed were implemented:

- Straight edge-coupled (horizontal) feed with a single quarter-wave transformer matching network
- Edge-coupled (horizontal) feed with a single bend in the quarter-wave transformer matching network
- Folded "U"-shaped edge-coupled (horizontal) feed with three bends in the matching network that consists of three cascaded quarter-wave transformers. The feed is designed and optimized to maximize the port isolation and facilitate the integration of the radiating element into arrays.

We will analyze the port isolation performance of all three cases and compare the measured and simulated results for both port isolation and cross-polarization performance. The port isolation of the radiating element with the folded "U"-shaped feed network exhibits an improvement of 20dB compared to the element with one bend in the horizontal feed. This feed network modification represents the first step in combating the port isolation degradation in dual-polarized microstrip patch arrays. In addition to these three cases a modified third case with a coaxial probe feeding the matching network instead of the 50Ω microstrip line is presented in order to study the cross-polarization performance degradation due to the radiation of the vertical 50Ω portion of the edge feed.

The focus of Chapter 4 is the integration of the single element into an array which is one of the main contributions of the thesis. We will discuss the effects of the array environment on the element. We will introduce the techniques mitigating the impact of the array environment on the port isolation performance of the antenna by means of appropriate element grouping and rerouting of cross-coupling susceptible portions of the feed network. The measured and simulated results will be presented for both port isolation and cross-polarization performance of the arrays. The methods and observations which were found to be useful in achieving the desired port isolation performance of the antenna and which could significantly accelerate the design process of dual-polarized microstrip patch arrays in the future will be presented. Using the above-mentioned techniques 2x4 and 4x4 element dual-polarized microstrip arrays with corporate feed networks were designed and their port isolation performance exceeded the targeted port isolation of 40dB. In the process of designing 2x4 and 4x4 arrays we identified the portions of the feed network most susceptible to the cross-coupling and devised specific routing for these sections of the feed network in order to lessen their impact on the port isolation performance. We also investigated the effects the excitation amplitude taper and the excitation phase progression have on the port isolation and found that by applying amplitude taper along certain axis has detrimental effects on port isolation while applying amplitude taper along the orthogonal axis actually improves the port isolation. By appropriately combining the amount of excitation of amplitude taper along these two axis one can suppress the sidelobe levels without sacrificing the port isolation performance.

Chapter 5 contains the conclusions drawn from the material in Chapters 3 and 4 and contributions, therein described, are summarized. The future development suggestions and ideas are also presented.

Chapter 2

Review of Dual-Polarized Microstrip Patch Radiators and Array antennas

2.1 Introductory Remarks

In this chapter we will review relevant aspects of the microstrip antenna design and how they affect the design of dual-polarized microstrip radiators with high port isolation. The electromagnetic wave polarization will be reviewed. We will mention and briefly discuss several analysis methods used to predict the performance of microstrip radiators. The review of the feed mechanisms commonly used to excite microstrip radiators with their advantages and drawbacks will be presented. Finally we will do a literature review of existing dual-polarized microstrip patch antenna designs for both single patch radiators and microstrip patch arrays. The literature review will be focused on the design layouts and port isolation performance of the dual-polarized microstrip patch antenna geometries. The antenna geometries are presented in the order of the increasing feed design complexity as antenna designers strived to attain the balance between the high port isolation performance and good cross-polarization performance.

2.2 Electromagnetic Wave Polarization

The state of polarization of an electromagnetic wave is defined according to the orientation of the electric field vector of the wave and its orientation variation with time. The electric field vector of the wave in the far zone of its source can always be decomposed into two orthogonal components in the plane transverse to the direction of the propagation. In general the polarization of the wave is elliptical, however, there are two special cases and these are linear and circular polarization. If the two components of the electric field vector are in phase then we have a case of linear polarization. The orientation of the linear polarization in space (horizontal, vertical, etc) is determined by the magnitudes of the

electric field vector components. If the two components of the electric field vector are of equal magnitude and 90° out of phase, then we have a case of circular polarization. In addition to the shape of the locus of the electric field vector tip we need to specify the sense of polarization in a case of circular or elliptical polarization. The sense of the polarization can be determined as either left hand or right hand depending on the direction of the propagation of the wave and the phase shift between the components of the electric field vector.

In the far field region the electric field vector has the dependency on r given by 2.2-1.

$$\overline{E}(r,\theta,\phi) = \overline{E}(\theta,\phi)\frac{e^{-jkr}}{r} \qquad 2.2\text{-}1$$

The longitudinal component of the field is negligible compared to the transverse components. Since the state of polarization is determined by the behavior of the electric field vector in the plane transverse to the direction of propagation we will analyze the $\overline{E}(\theta,\phi)$ and its components in 2.2-2.

$$\overline{E}(\theta,\phi) = E_\theta\hat{\theta} + E_\phi\hat{\phi} \qquad 2.2\text{-}2$$

An electric field of a wave of any polarization can be represented by a linear combination of two fields polarized such that their respective unit vectors satisfy $\hat{u}_1 \times \hat{u}_2^* \neq 0$ (or $\hat{u}_1 \cdot \hat{u}_2^* \neq 1$). Polarization unit vectors of the two components must be linearly independent. Given the electric field of an electromagnetic wave one can determine the magnitude of polarization component p simply by $E_p = \overline{E}(\theta,\phi)\cdot\hat{u}_p^*$.

Two polarizations are said to be orthogonal if the condition 2.2-3 is satisfied:

$$\hat{u}_1 \cdot \hat{u}_2^* = 0 \qquad 2.2\text{-}3$$

Since orthogonal polarizations have linearly independent unit vectors any state of polarization can be represented as a liner combination of two orthogonal polarizations as in 2.2-4.

$$\hat{u} = a\hat{u}_1 + b\hat{u}_2 \qquad 2.2\text{-}4$$

A circular polarization is a linear combination of the vertical and horizontal polarization with the vertical and horizontal components being equal in magnitude $E_H = E_V = E$ and $\pm 90°$ out of phase. $\overline{E}(\theta,\phi) = E_H\hat{u}_H \pm jE_V\hat{u}_V$ where $\hat{u}_V = \hat{\theta}$ and $\hat{u}_H = \hat{\phi}$

Similarly a linear vertical polarization is a linear combination of the right hand circular polarization (RHCP) and left hand circular polarization (LHCP) with $E_{RHCP} = E_{LHCP} = E$.

$$\bar{E}(\theta,\phi) = E_{RHCP}\hat{u}_R \pm E_{LHCP}\hat{u}_L \quad \text{where} \quad \hat{u}_R = \frac{1}{\sqrt{2}}\left(\hat{\theta} - j\hat{\phi}\right) \text{ and } \hat{u}_L = \frac{1}{\sqrt{2}}\left(\hat{\theta} + j\hat{\phi}\right)$$

This can be generalized to $\bar{E}(\theta,\phi) = E_1\hat{u}_1 + E_2\hat{u}_2$ where $\hat{u}_1$ and $\hat{u}_2$ are unit vectors of the two orthogonal polarizations with respective complex amplitudes E_1 and E_2. The polarization efficiency coefficient (e_p) in the Friis' link equation 2.2-5 is defined in 2.2-6.

$$P_R = P_T + G_T + 10\log(e_p) + 20\log\left(\frac{\lambda}{4\pi R}\right) + G_R \qquad 2.2\text{-}5$$

$$e_p = \left|\hat{u}_{Tx} \cdot \hat{u}_{Rx}^*\right|^2 \qquad 2.2\text{-}6$$

Antennas in the link with $e_p \approx 1$ are said to be co-polarized, and in the link with $e_p \approx 0$ antennas are said to be cross-polarized. The e_p concept will be used in the measurements described in Chapter 4.

2.3 Rectangular Microstrip Patch Radiator

A microstrip patch antenna consists of a grounded dielectric substrate and an arbitrarily shaped metallic patch etched on the top. In this thesis we will concentrate on a radiating patch of rectangular shape only. Microstrip patch radiators are resonant antennas and will resonate when the main dimension of the antenna is in the vicinity of a half guided wavelength ($\lambda_g = \lambda_0/\sqrt{\varepsilon_{eff}}$; λ_g -guided wavelength, λ_0 -freespace wavelength, ε_{eff} - effective relative dielectric constant) [1]. The dimensions of the radiating patch will affect the resonant frequency and input impedance of the antenna. Several feeding mechanisms are available and each mechanism has its advantages and disadvantages. The choice of a specific feeding mechanism will influence the impedance bandwidth, radiation efficiency and the complexity of fabrication. The substrate properties such as thickness and relative

permittivity will affect the impedance bandwidth, the radiation efficiency as well as the physical dimensions of the radiator. The performance of the microstrip patch can be approximately modeled using transmission line model, or cavity model.

The transmission line model of the microstrip patch [1] consists of a transmission line loaded with load Y_e at both ends as shown in Figure 3. The real part of each load represents the radiation losses and the imaginary part represents fringing capacitance of the microstrip patch open end.

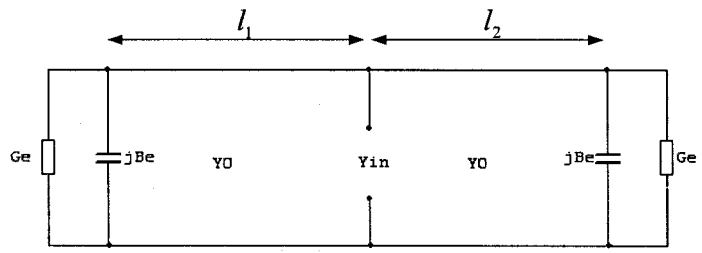

Figure 3 Transmission line model of the microstrip patch antenna with a coaxial probe feed or an inset edge feed

The input admittance of the microstrip patch fed by a coaxial probe or an inset edge-coupled feed as predicted by the transmission line model is given by 2.3-1.

$$Y_{in} = Y_0 \left[\frac{Y_e + jY_0 \tan \beta l_1}{Y_0 + jY_e \tan \beta l_1} + \frac{Y_e + jY_0 \tan \beta l_2}{Y_0 + jY_e \tan \beta l_2} \right] \qquad 2.3\text{-}1$$

For patches with edge-coupled feed the transmission line model is shown in Figure 4.

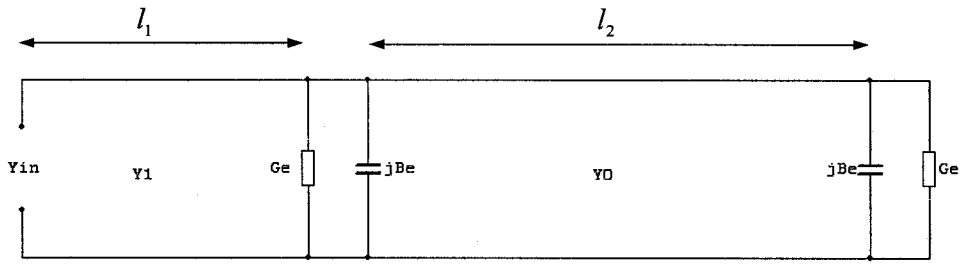

Figure 4 Transmission line model of the microstrip patch antenna with an edge feed

The input admittance of the edge-fed microstrip patch as predicted by the transmission line model is given by 2.3-2.

$$Y_{in} = Y_1 \frac{\left(Y_e + Y_0 \frac{Y_e + jY_0 \tan\beta_0 l_2}{Y_0 + jY_e \tan\beta_0 l_2} \right) + jY_1 \tan\beta_1 l_1}{Y_1 + j\left(Y_e + Y_0 \frac{Y_e + jY_0 \tan\beta_0 l_2}{Y_0 + jY_e \tan\beta_0 l_2} \right) \tan\beta_1 l_1} \qquad 2.3\text{-}2$$

The edge conductance and susceptance are given by empirical expressions [1] 2.3-3 and 2.3-4.

$$Y_e = G_e + jB_e \qquad G_e = 0.00836 \frac{W}{\lambda_0} \qquad B_e = 0.01668 \frac{\Delta l}{h} \frac{W}{\lambda_0} \varepsilon_e \qquad 2.3\text{-}3$$

$$\varepsilon_{eff} = \frac{\varepsilon_r + 1}{2} + \frac{\varepsilon_r - 1}{2} \left(\sqrt{1 + 12 \frac{h}{W}} \right)^{-1} \qquad \frac{\Delta l}{h} = 0.412 \frac{\left(\varepsilon_{eff} + 0.3 \right)\left(\frac{W}{h} + 0.264 \right)}{\left(\varepsilon_{eff} - 0.258 \right)\left(\frac{W}{h} + 0.8 \right)} \qquad 2.3\text{-}4$$

The TL model predicts the input impedance of the radiator and does not account for any other mode except for the fundamental mode.

The cavity model [2] is based on the assumptions that electric field underneath the patch is entirely perpendicular to the patch and the groundplane, and that the magnetic field tangential to the edges of the patch is negligible. Using these two assumptions we can replace the patch by a perfect electric conductor (PEC) wall, and we can enclose the volume underneath the patch from the sides by perfect magnetic conductor (PMC) walls. Using the image theory we will obtain the cavity that has PEC walls at the top and bottom and PMC walls on all four sides. The field distribution (Figure 5) along non-radiating edges (patch edges parallel to the direction of the current on the patch) is such that the contributions to the far field from equivalent magnetic currents along non-radiating edges cancel each other. The field distribution along the radiating edges (edges perpendicular to direction of the current on the patch) is such that the far field contributions from the equivalent magnetic currents along these edges combine constructively.

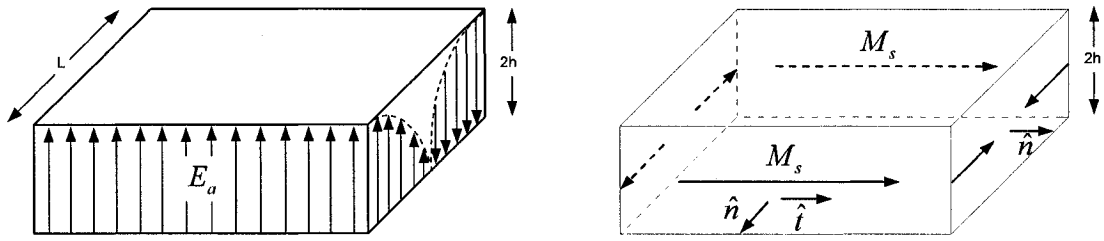

Figure 5 Cavity model of the microstrip patch antenna

The equivalent currents on the four side walls of the cavity are given by $\bar{J}_s = \hat{n} \times \bar{H}_a$ and $\bar{M}_s = -2\hat{n} \times \bar{E}_a$.

The components of the magnetic field $\bar{H}_a$ tangential to the PMC side walls vanish and thus $\bar{J}_s = \hat{n} \times \bar{H}_a = \hat{n} \times \left(\hat{n} H_{an} + \hat{t} H_{at}\right) = 0$.

The components of the electric field $\bar{E}_a$ tangential to the PMC side walls are nonzero, the magnetic current on the side walls is also nonzero and is given by $\bar{M}_s = -2\hat{n} \times \bar{E}_a$.

Electric vector potential $\bar{F}(r,\theta,\phi)$ is given in 2.3-5.

$$\bar{F}(r,\theta,\phi) = \frac{\varepsilon}{4\pi} \iiint_{V'} \bar{M}_s(r',\theta',\phi') \frac{e^{-jk|\bar{r}-\bar{r}'|}}{|\bar{r}-\bar{r}'|} dV' \qquad 2.3\text{-}5$$

Electric and magnetic fields due to magnetic current distribution $\bar{M}_s(r,\theta,\phi)$ in each of the slots are given by 2.3-6 and 2.3-7

$$\bar{E}_F = -\frac{1}{\varepsilon} \nabla \times \bar{F} \qquad 2.3\text{-}6$$

$$\bar{H}_F = -j\omega\bar{F} - \frac{j\nabla\left(\nabla \cdot \bar{F}\right)}{\omega\mu\varepsilon} \qquad 2.3\text{-}7$$

In the far field region the transverse field components (radial components are negligible) due to electric vector potential $\bar{F}$ are given in 2.3-8 and 2.3-9.

$$H_\theta \approx -j\omega F_\theta \qquad E_\theta \approx -j\omega\eta F_\phi = \eta H_\phi \qquad 2.3\text{-}8$$

$$H_\phi \approx -j\omega F_\phi \qquad E_\phi \approx j\omega\eta F_\theta = -\eta H_\theta \qquad 2.3\text{-}9$$

Radiation fields of the microstrip patch are the superposition of the fields of the two individual slots with magnetic current distribution $\bar{M}_s = -2\hat{n} \times \bar{E}_a$. The cavity model offers

moderate prediction accuracy and has the advantage of closed form solution that allows for computational efficiency [1].

The transmission line model and the cavity model are based on a number of assumptions that limit the prediction accuracy. With widespread availability of powerful personal computers numerical methods such as Method of Moments (MoM), Finite Element Method (FEM), and Finite Difference Time Domain method (FDTD) became the prevalent tools in predicting the performance of microstrip antennas. These numerical methods are used to solve Maxwell's equations under the boundary conditions imposed by the antenna geometry, thus eliminating the simplifying assumptions on which transmission line and cavity model relied in order to solve the problem. In this thesis all the simulations were done using Zeland IE3D software [3] that employs MoM as a numerical method for solving Maxwell's integral field equations. The excellent agreement between simulation and measurement in Chapter 3 and 4 will be seen to support this choice.

2.4 Microstrip Patch Feed Mechanisms

The methods of exciting the microstrip patches can be divided into two groups:

Direct Contact Methods

- Edge-coupled feed
- Probe-coupled feed

Non-Contact Methods

- Proximity-coupled feed
- Aperture-coupled feed

These excitation mechanisms affect the performance of the antenna and the complexity of its manufacturing process. Feed mechanism diversity will enable us to achieve higher isolation performance compared to the designs where only one type of the feed mechanism is used. In sections 2.4.1 through 2.4.4 we will describe the above-mentioned feed mechanisms and based on their properties we will select two of them for the design of our antenna.

2.4.1 Edge-Coupled Feed

One of the most basic excitation methods used to feed the microstrip patch is the edge-coupled feed or microstrip feed shown in Figure 6. In the edge-coupled feed scenario microstrip line is in the direct contact with one of the edges of the microstrip patch. The edge-coupled feed excitation mechanism of the microstrip patches falls into the category of direct contact feeds.

The advantages [4] of this type of feed include:

- Simplicity of fabrication
- Simple easy-to-implement matching networks
- Relatively high efficiency
- Ease of integration into arrays

Disadvantages [4] of this type of feed are:

- Radiation from the feed network,
- Narrow bandwidth,
- Relatively high cross-polarization levels.

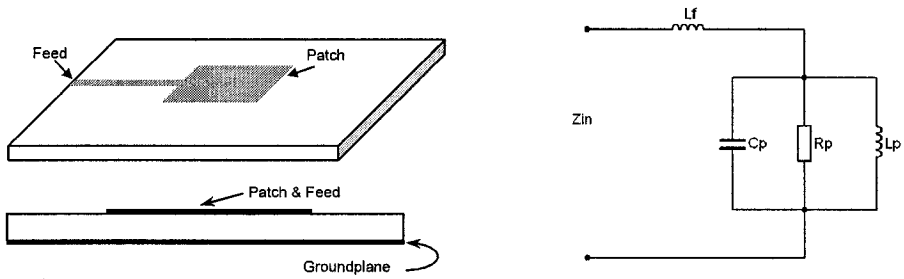

Figure 6 Edge-coupled feed and its equivalent circuit (after [4])

The input impedance of the edge-coupled fed microstrip patch [4] is given by 2.4.1-1.

$$Z_{in} = j\omega L_f + \frac{j\omega L_p R_p}{R_p\left(1-\omega^2 L_p C_p\right) + j\omega L_p} \qquad 2.4.1\text{-}1$$

2.4.2 Probe-Coupled Feed

The probe-coupled feed method of excitation shown in Figure 7 is when a coaxial transmission line directly feeds the microstrip patch. The coupling efficiency is better than in other coupling methods due to inherent low radiation from the coaxial feed (especially when used with thin substrates). A proper probe positioning provides good impedance match and circumvents the necessity of matching networks thus simplifying the circuit design. The feed network is separated from the radiating element by the groundplane which allows for increased flexibility in the feed network design and removes detrimental effects of spurious feed radiation present in edge-coupled feed arrangement. However probe-coupled feed requires usage of vias in the substrate. Also, the other components of the feed network, couplers and splitters, must be built using coaxial transmission lines which complicates the manufacturing process. The probe-coupled feed microstrip patches suffer from narrow bandwidth due to limitation on thickness of the substrate. The substrate thickness needs to be limited in order to avoid the resonance problems with probe-coupled feed which occur when substrate thickness is increased. [4]

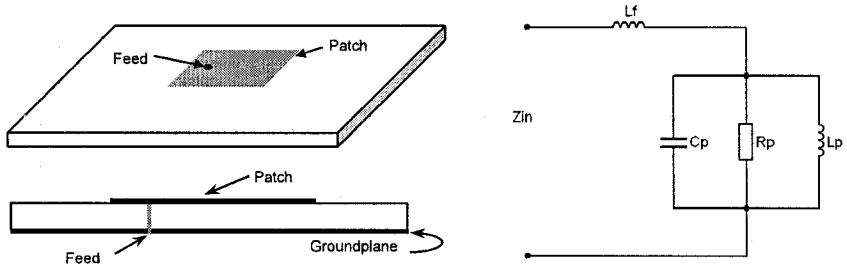

Figure 7 Probe-coupled feed and its equivalent circuit (after [4])

The input impedance of the probe fed microstrip patch [4] is given by 2.4.2-1.

$$Z_{in} = j\omega L_f + \frac{j\omega L_p R_p}{R_p\left(1-\omega^2 L_p C_p\right) + j\omega L_p} \qquad 2.4.2\text{-}1$$

2.4.3 Proximity-Coupled Feed

The proximity-coupled feed shown in Figure 8 falls into the category of non-contact feeds and it was conceived in order to alleviate the drawbacks suffered by contact feed excitation methods. The proximity-coupled feed allows for an additional degree of freedom

in the design by separating the feed network assembly from the radiating element. The feed line is etched on the grounded substrate of relatively high permittivity in order to prevent radiation from the feed and to reduce the physical size of the microstrip circuitry in the feed network. The radiating element is etched on a dielectric sheet of lower permittivity with thickness selected in accordance with bandwidth requirements. This arrangement makes feed network design more independent from the design of the radiating element and vice versa. Knowing that feed network parameters and radiating element parameters are conflicting in terms of optimum performance, extra degree of freedom introduced by proximity-coupled feed helps optimize the feed and the radiating element separately to enhance the overall performance of the antenna. [4]

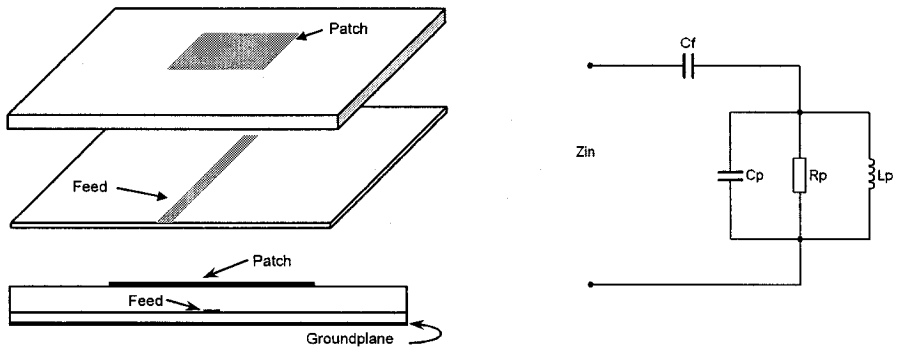

Figure 8 Proximity-coupled feed and its equivalent circuit (after [4])

The input impedance of the proximity-coupled microstrip patch [4] is given by 2.4.3-1.

$$Z_{in} = -\frac{j}{\omega C_f} + \frac{j\omega L_p R_p}{R_p\left(1-\omega^2 L_p C_p\right) + j\omega L_p} \qquad 2.4.3\text{-}1$$

2.4.4 Aperture-Coupled Feed

In response to drawbacks of direct contact feeding techniques, such as feed radiation, narrow bandwidth, and high surface wave losses, the aperture-coupled feed shown in Figure 9 was introduced. In the aperture-coupled feed scenario the feed and the radiating element are separated by the groundplane and energy from the feed is coupled through an aperture in the groundplane underneath the radiating element. This allows for separate selection of substrate for the radiator and the feed. The radiator substrate is selected in accordance with requirements of the radiation efficiency and bandwidth,

whereas the feed substrate is selected to prevent the feed radiation and in accordance with microstrip transmission line design guidelines. This structure enables the designer to optimize the radiating element and its feed network with a high degree of independence. The geometry requires no vias or vertical interconnections which simplifies the manufacturing process significantly. However the alignment between the feed, aperture and the radiating element becomes critically important. The aperture-coupled microstrip patches produce very purely polarized radiation which becomes very important in dual-polarized microstrip patches. Because this feeding mechanism features more design parameters than simple edge-coupled feed, it offers more flexibility in the design. [4]

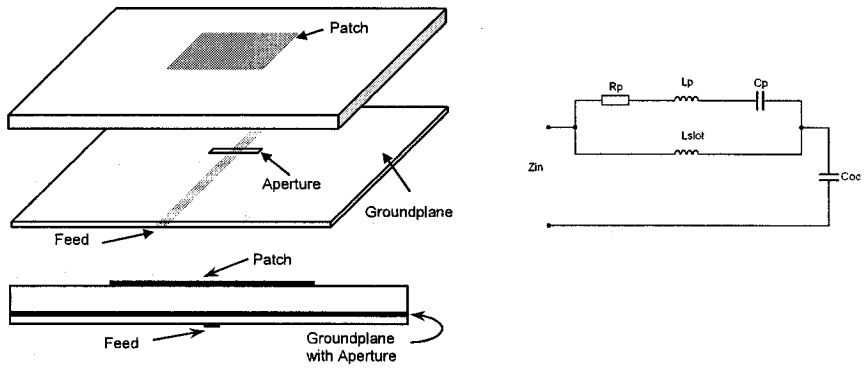

Figure 9 Aperture-coupled feed and its equivalent circuit (after [4])

The input impedance of the aperture-coupled microstrip patch [4] is given by 2.4.4-1

$$Z_{in} = j\omega L_s \frac{\omega R_p C_p + j\left(\omega^2 L_p C_p - 1\right)}{\omega R_p C_p + j\left(\omega^2 L_p C_p + \omega^2 L_p C_s - 1\right)} \qquad 2.4.4\text{-}1$$

2.5 Dual-Polarized Microstrip Patch

The state of polarization of an electromagnetic wave radiated by a microstrip patch radiator is dictated by the current distribution on the radiating element. The current distribution is determined by the geometry of the radiating element, the feeding mechanism, and the placement of one or more feeds. It is possible to excite a radiating element to produce orthogonal current distribution modes, which will then radiate orthogonally polarized spherical waves. We will now review the dual-polarized microstrip patch layouts reported in the literature in the order of increasing feed design complexity.

The simplest way of exciting the orthogonal current distribution modes on the microstrip patch radiator is shown in the Figure 10a.

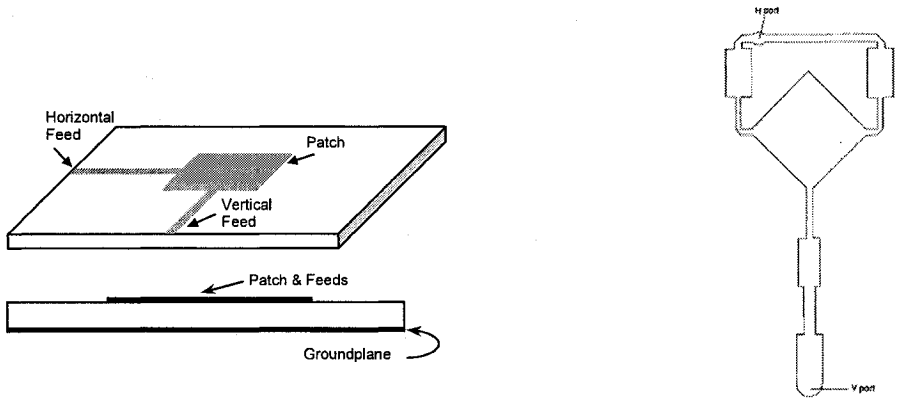

a) b) after [5]

Figure 10 Dual-polarized edge-coupled patches

A slightly more complicated dual-polarized patch feeding mechanism featuring balanced horizontal feed shown in Figure 10b was presented in [5] with reported port isolation of 35dB.

In order to improve the polarization purity, or in other words, to reduce the cross-polarization levels, the gridded microstrip patch radiator shown in Figure 11 was introduced [6] and the port isolation performance achieved at resonance is slightly better than 25dB.

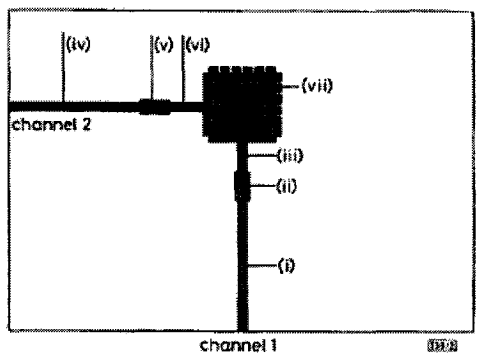

Figure 11 Gridded dual-polarized microstrip patch radiator (after [6])

Another way of exciting orthogonal current distribution modes is the gap-coupled dual-polarized microstrip patch presented in [7] and shown in Figure 12. The port isolation for this geometry measured at resonance frequency was 32dB.

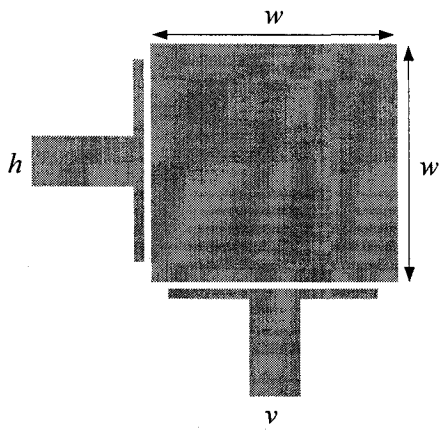

Figure 12 Gap-coupled dual-polarized microstrip patch radiator

Dual-aperture patches further improve the polarization purity and eliminate the spurious radiation contributions from the feed network, which is separated from the radiating element by the groundplane. The aperture-coupled patches require an additional substrate layer for the feed network. The alignment between the feed network, aperture in the groundplane, and the radiating element is a crucial design concern.

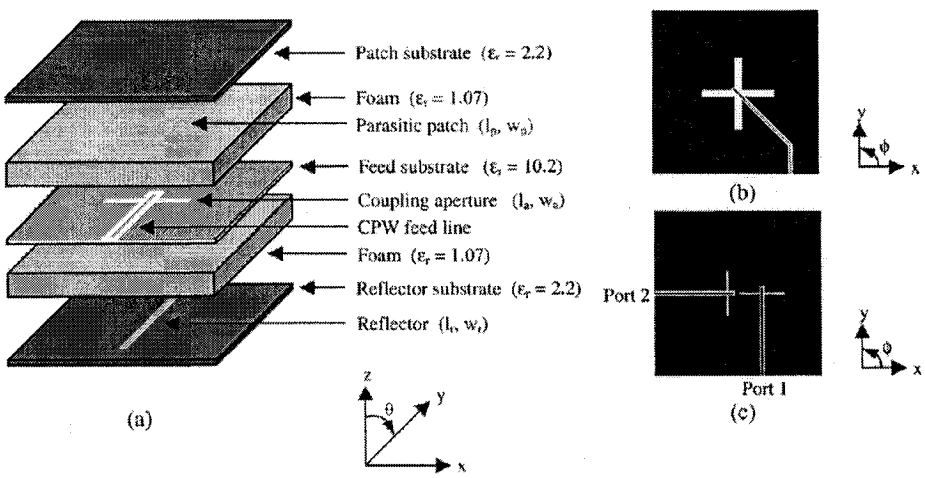

a) Layer stack-up

b) Dual-linearly-polarized single feed aperture-coupled microstrip patch

c) Dual-polarized aperture-coupled microstrip patch

Figure 13 Aperture-coupled microstrip patch radiator with coplanar waveguide feeds (after [8])

The layer stack-up of the dual-polarized aperture-coupled microstrip patch and the layout of the feed network [8] are shown in Figure 13. The port isolation at resonance reported for this geometry is better than 40dB.

To further improve the polarization purity many authors including Gao [9] optimized the relative positioning of the apertures, as well as their locations relative to the radiating element. Resulting optimized patch is shown in Figure 14.

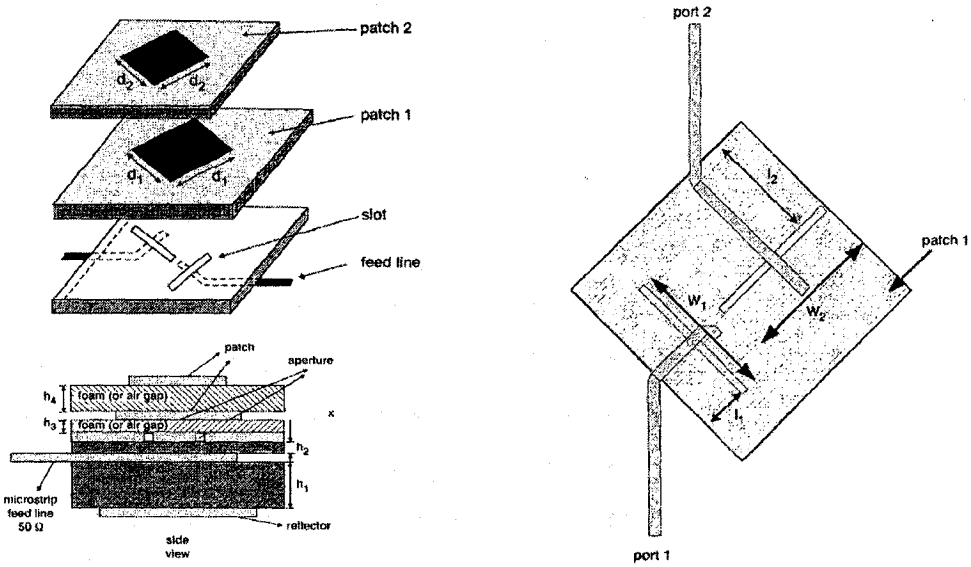

Figure 14 Dual-polarized aperture-coupled patch with optimized aperture positions (after [9])

Additional improvements in the port isolation performance were achieved by modifying the shape of the aperture [10] as shown in Figure 15.

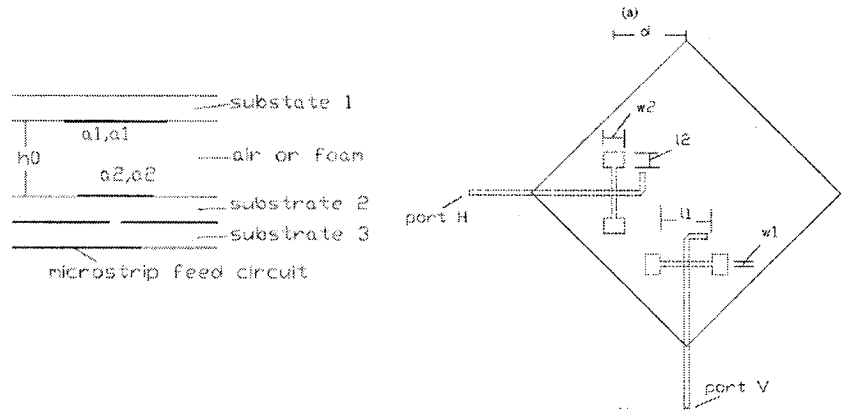

Figure 15 Dual-polarized microstrip patch with a modified aperture shape (after [10])

Geometries in Figure 14 and Figure 15 exhibit the port isolation of 40dB at resonance.

It is possible to improve the polarization purity of the dual-polarized patch by balancing one of the feeds in order to maintain the symmetry of the geometry [11]. The dual-polarized patch with balanced horizontal feed and the port isolation of 35dB at resonance is shown in Figure 16.

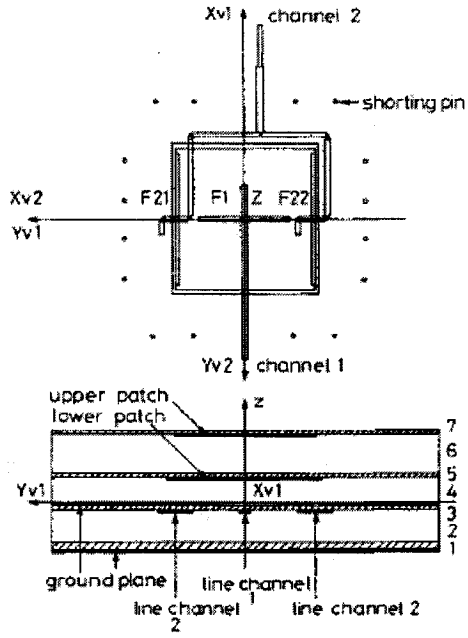

Figure 16 Dual-polarized aperture-coupled microstrip patch with a balanced horizontal feed (after [11])

The design [12] featuring two balanced feeds, with the port isolation better than 25dB is shown in Figure 17.

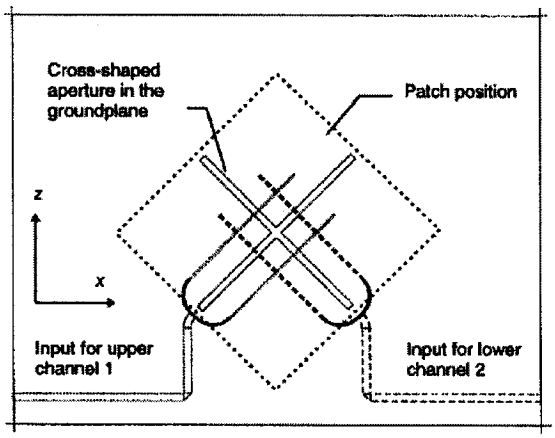

Figure 17 Dual-polarized aperture-coupled microstrip patch with two balanced feeds (after [12])

Modifications to the shape of the radiating element itself can also contribute to improvements in the polarization purity [13]. The gridded dual-polarized aperture-coupled microstrip patch with the port isolation of 35dB at resonance is shown in Figure 18.

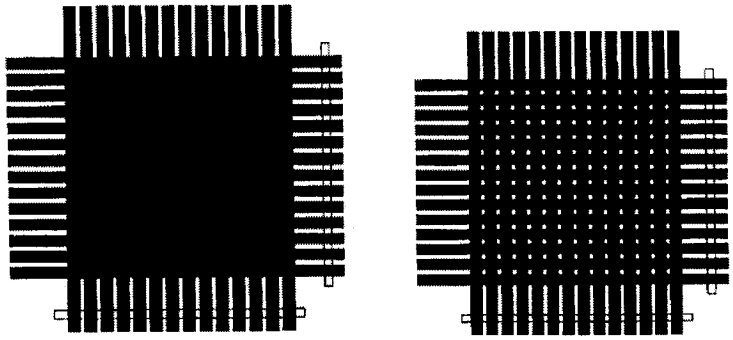

Figure 18 Gridded dual-polarized aperture-coupled microstrip patch (after [13])

The design of dual-polarized microstrip antennas is not limited to the rectangular shape of the radiating element. Many designers use ring [14], and circular radiators [15], examples of which are shown in Figure 19 and Figure 20, with respective port isolations of 35dB and 30dB.

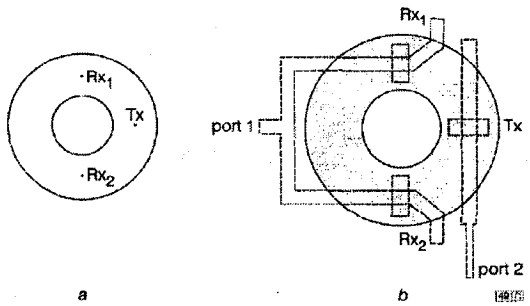

Figure 19 Dual-polarized aperture-fed ring microstrip antenna (after [14])

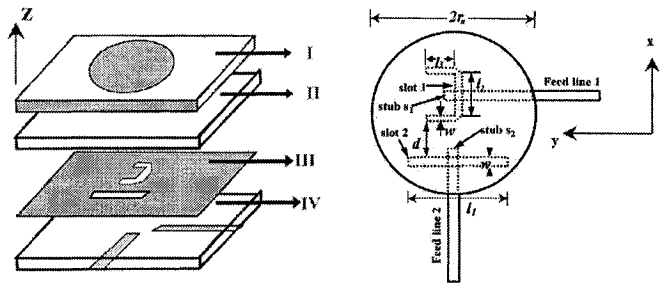

Figure 20 Dual-Polarized aperture-fed circular microstrip antenna (after [15])

In sections 3.2 and 3.4 we will show how a port isolation of better than 36dB can be achieved using a feed geometry simpler than those reviewed here.

2.6 Feed Networks and Microstrip Lines

A single microstrip radiating element has a low gain and a broad beam. If a higher gain and narrower beam are required, a number of elements need to be arranged into an array. In order to excite the radiating elements in an array a feed network is needed. The purpose of the feed network is to transport radio frequency (RF) power to/from individual radiating elements. In the transmit mode the feed network splits power coming from the transmitter and delivers it to individual radiating elements with amplitude and phase designated for each radiating element. In the receive mode the feed network combines RF power from individual radiating elements and delivers it to the receiver. Feed networks are designed to provide particular excitation amplitude and the phase distribution. They are often referred to as a beam forming network since the element excitation amplitudes and phases determine the beam shape and direction.

The feed networks can be divided into the following types:

- Series feed networks
- Corporate (parallel) feed networks
- Combined series-corporate feed networks

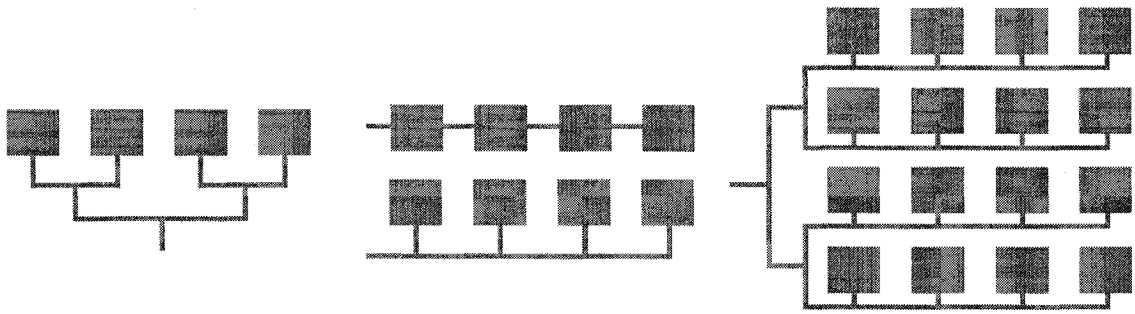

a) Corporate b) Series c) Corporate-series

Figure 21 Feed networks

In order to achieve beam squinting by means of phase progression with a corporate feed network, the length of the path to each element is designed to provide an appropriate excitation phase. This is done by appropriately shifting the positions of the power-splitting junctions within the feed network. To achieve a phase progression in a series network the path between the adjacent radiating elements is increased or decreased to achieve the desired phase shift. The radiating element spacing is done with respect to freespace wavelength and phase progression with respect to feed network guided wavelength. The

difference between guided and freespace wavelength increases the complexity of the series feed network design. When no phase progression is required the corporate network phase response is frequency independent. Corporate feed networks require less effort in power splitter design than series feed networks when the uniform amplitude excitation is implemented for maximum aperture efficiency. By varying power splitting ratio the tapered excitation amplitude can be realized, and through tapered excitation amplitude sidelobe level suppression can be achieved at the expense of lowering the aperture efficiency.

2.7 Dual-Polarized Microstrip Patch Arrays

Dual-polarized edge-coupled arrays consist of dual-polarized edge-coupled microstrip radiating elements arranged in a lattice (usually rectangular). The RF power is delivered to the individual elements by means of a feed network which resides on the same level with the radiating elements. Having the feed network and the radiating elements on the same level increases the difficulty of the design process. However, a single substrate layer design is sometimes desirable because it simplifies the manufacturing process and lowers the production cost. In a single substrate layer design the designer is forced to use, at least in part, the series feed network which limits the design options for beam shaping, and introduces unwanted frequency dependence. Also as we can see from the examples in Figure 22 and Figure 23 that it is difficult to design sub-arrays that are easy to integrate into larger arrays. Having the feed networks on the same level as the radiating elements will have detrimental effects on the array performance. Spurious radiation from the feed lines will contribute to an increase in cross-polarization levels, while mutual coupling between the feed lines, and coupling between the feed lines and radiating elements will decrease port isolation.

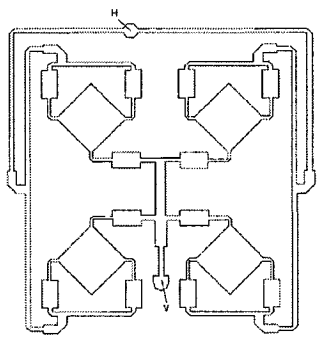

Figure 22 Dual-polarized edge-coupled microstrip patch array with a balanced horizontal feed (after [16])

The reported port isolation performance for geometries in Figure 22 and Figure 23 is 35dB.

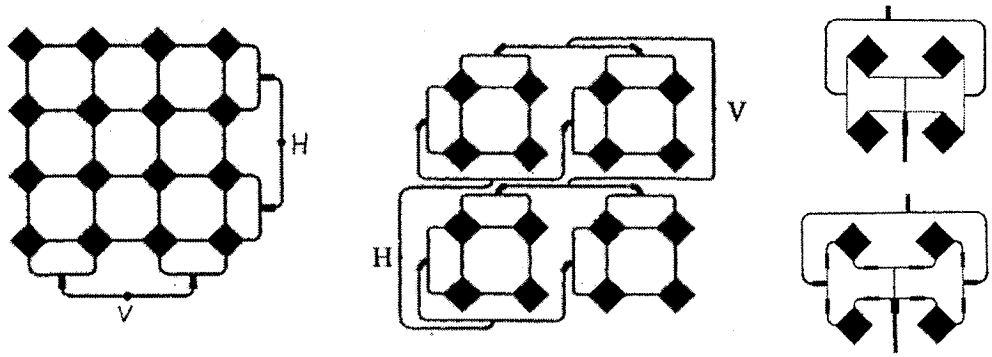

Figure 23 Dual-polarized edge-coupled microstrip patch array (after [17])

One can easily see that there is an incentive to separate the radiating elements and the feed networks by a ground plane, or at least remove the feed networks from the level of substrate on which the radiating elements reside. An example of an array with feed networks placed on a different level from that of the radiating elements is shown in Figure 24. The feed network in this array is proximity-coupled. The appropriate selection of the feed network substrate material will prevent spurious radiation from the feed network, but the difficulty of routing two feed networks on the same level remains.

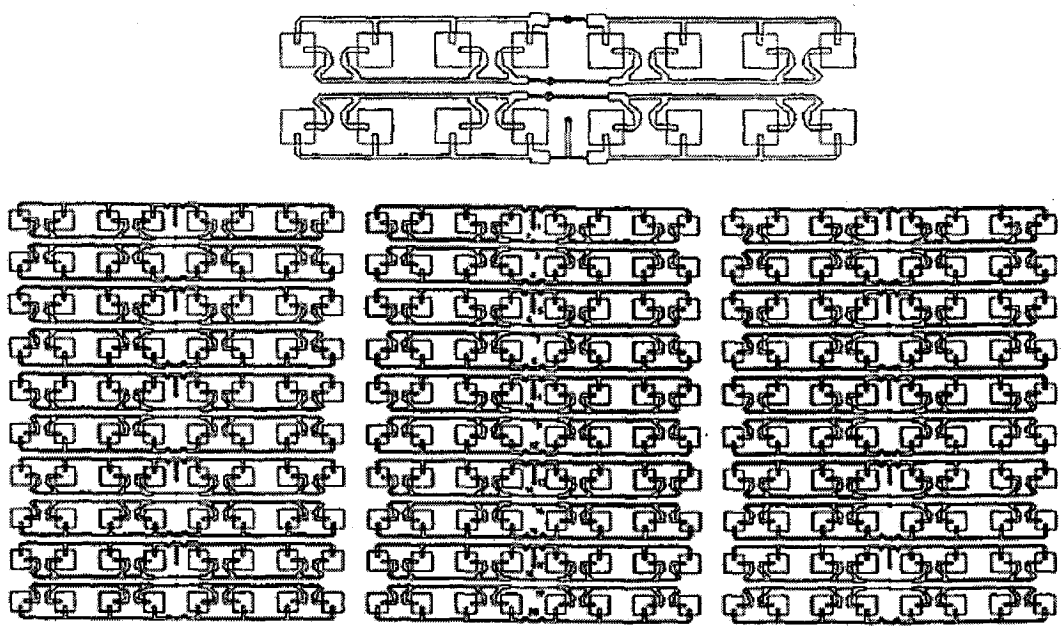

Figure 24 Dual-polarized proximity-coupled microstrip patch array (after [18])

In Figure 14 we have seen that dual-polarized aperture-coupled microstrip patch radiators have the advantage of having feed networks separated from radiating elements by a groundplane, thus eliminating unwanted coupling between the feed network and radiating elements, and allowing the designer more freedom in routing the feed networks [4]. But once again we have two feed networks residing on the same level forcing the designer to use series feed networks or the combination of corporate and series feed networks. An example of dual-polarized aperture-coupled microstrip patch array [19] with series feed networks and the port isolation better than 19dB is shown in Figure 25.

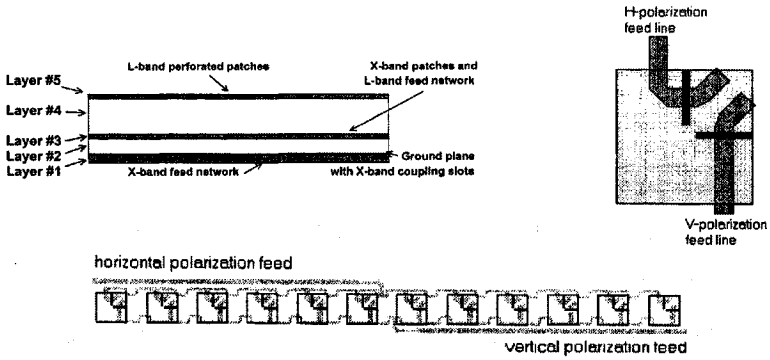

Figure 25 Dual-polarized aperture-coupled microstrip patch array with a series feed network (after [19])

Another example of a dual-polarized aperture-coupled microstrip array with series feed networks featuring cross-shaped radiating patches and "H"-shaped apertures [20] with port isolation slightly better than 35dB at resonance is shown in Figure 26.

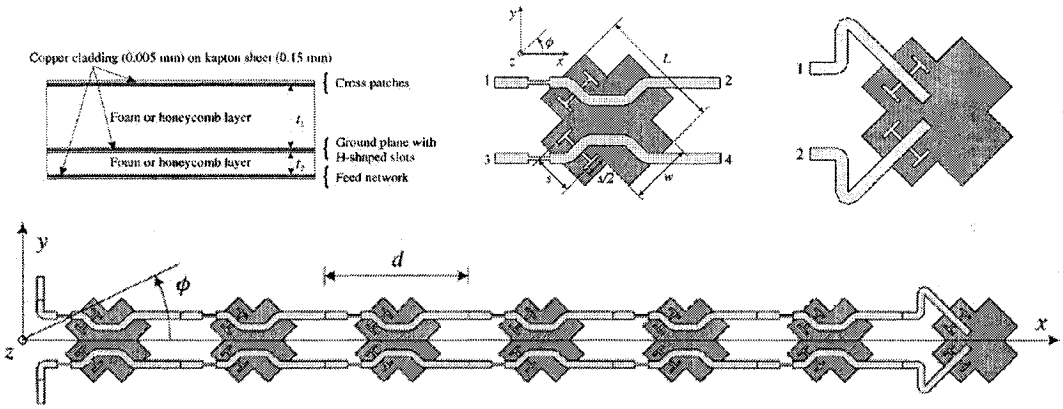

Figure 26 Dual-polarized aperture-coupled microstrip array with a series feed and cross shaped radiating patches (after [20])

The dual-polarized aperture-coupled linear microstrip patch array [22,[23] is shown in Figure 27.

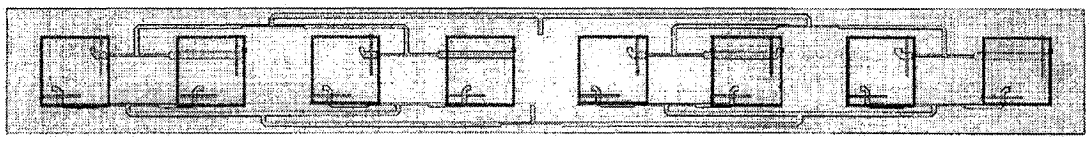

Figure 27 Dual-polarized aperture-coupled microstrip patch 8x1 element array with a corporate feed network (after [22, 23])

A dual-polarized aperture-coupled microstrip patch array with combined series-corporate feed networks shown in Figure 28 has a reported port isolation of just over 20dB at resonance [21].

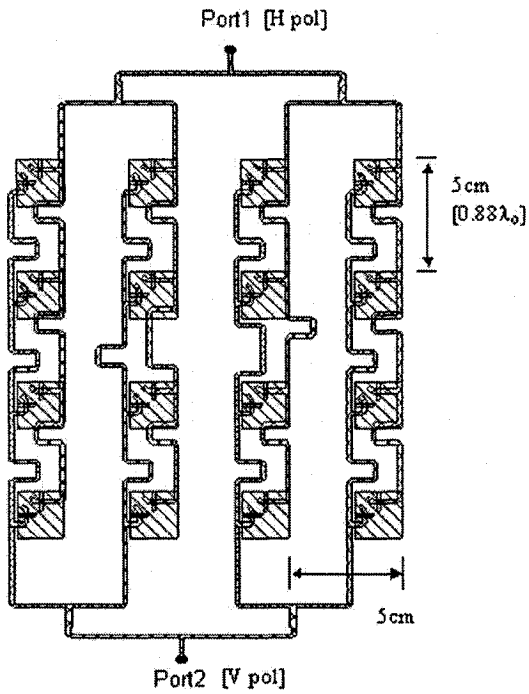

Figure 28 Dual-polarized aperture-coupled microstrip patch 4x4 element array with a combined series-corporate feed network (after [21])

If we were to use the linear array with corporate feed network from Figure 27 as a building block sub-array for a planar array, the mutual coupling between long sections of parallel feed lines belonging to adjacent sub-arrays would lower the port isolation level to less than 35dB. This is the most likely reason the port isolation of the planar array in Figure 28 is reduced to 20dB.

2.8 Integral Equation Solver (IE3D)

The simulations of dual-polarized microstrip antennas in this thesis were performed using Zeland IE3D full wave electromagnetic simulator [3]. This particular software package was selected for its efficiency and speed in solving multilayer planar structures such as microstrip antennas. IE3D uses Method of Moments (MoM) to solve Maxwell's equations taking into account: boundary conditions imposed by the structure geometry, port excitations, and material properties. The problem setup procedure steps include:

Geometry definition:	Defining the layer dimensions and material properties
	Creating the structure layout
	Excitation type
Solution Setup:	Meshing type and density
	Selecting matrix solver type
Post process:	S-parameters
	Current distribution
	Radiation patterns
	Near Field calculation

MoM is a numerical method for solving integral equations. The structure geometry is subdivided into cells each of which gets an unknown coefficient and a known expansion function assigned to it. The procedure is repeated for every cell and the integral equation is converted into a system of algebraic equations that can be solved. The values of the unknown coefficients are obtained by solving this system of algebraic equations. The solution of the initial integral equation is constructed using now known coefficients and previously known expansion functions. The meshing of the structure needs to be sufficiently dense to provide accurate results but not too dense to exceed the memory or processor resources available. For the structures in this thesis we balanced the requirements for precision and execution time without sacrificing the accuracy of the results obtained. All the simulations were performed on a PC with Dual Pentium IV 2.4GHz processor and 2GB of system RAM.

2.9 Concluding Remarks

We have introduced the aspects relevant to the design of the dual-polarized microstrip antennas such as: EM wave polarization, feed mechanisms, existing implementations of the single dual-polarized microstrip radiating element, existing implementations of the dual-polarized microstrip arrays and their port isolation performances.

The port isolation performance of reviewed single dual-polarized microstrip patches ranges from 25dB to 40dB and for the arrays between 19dB and 35dB. All the geometries use the same type of the feeding mechanism for both polarizations forcing the placement of the feed networks for both polarizations on the same physical level thus making these radiating elements difficult to integrate into large arrays capable of maintaining the high port isolation of the single radiating element building block.

In Chapter 3 we will show that using two different feeding mechanisms is essential in increasing the port isolation of a single dual-polarized microstrip patch. We will also examine the effects of feed routing in the immediate vicinity of the radiating element, which is unavoidable if the element is to be integrated into an array, on the port isolation of a single dual-polarized microstrip patch.

In Chapter 4 we will show that in order to enhance the array port isolation beyond that of the constituent microstrip patch radiating element special attention needs to be given to a manner in which the elements of the array are grouped together and to the routing of the certain sections of the feed network residing on the same physical level with radiating elements. Using the techniques that will be discussed in Chapter 4 we designed a 4x4 dual-polarized array with measured port isolation exceeding 50dB at resonance which is an improvement of more than 15dB compared to the designs presented in the review.

In the following chapters we will focus on the design of a dual-polarized microstrip array with high port isolation and we will emphasize the importance of the feed mechanism diversity in order to:

- Maximize the port isolation performance
- Be able to implement corporate feed networks for both polarizations
- Relax constraints on feed network routing.

References

[1] R. Bancroft, "Microstrip and Printed Antenna Design", Noble Publishing Co., Atlanta, GA, 2004

[2] I. J. Bahl, and P. Barthia, "Microstrip Antennas", Artech House, 1980 2nd Printing 1982, pp. 46

[3] IE3D, Zeland Software Inc., 48834 Kato Road - Suite 103A Fremont, CA, USA

[4] R. B. Waterhouse "Microstrip Patch Antennas: A Designer's Guide", Kluwer Academic Publishers, 2003

[5] S. C. Gao, L. W. Li, T. S. Yeo and M. S. Leong, "Low Cost, Dual Linearly Polarized Microstrip Patch Array", IEE Proc.-Microw. Antennas Propag., Vol. 148 No. 1. p21-24, February 2001

[6] J. M. Baracco, A. Roederer, and P. Brachat, "Dual-Polarisation Gridded Microstrip Radiating Element", Electronics Letters, Vol. 31, No. 6, p419-421, 16th March 1995

[7] D. G. Kurup, A. Rydberg and M. Himidi, "Compact Microstrip T-Coupled Patch for Dual Polarisation and Active Antenna Applications", Electronics Letters, Vol. 38, No. 21, p1240-1241, 10th October 2002

[8] Wayne S. T. Rowe, Rod B. Waterhouse, "Integratable Wide-Band Dual Polarized Antennas with Rear Field Cancellation", IEEE Transactions on Antennas and Propagation, Vol. 51, No. 3, p469-477, March 2003

[9] B. Lee, S. Kwon and J. Choi, "Polarization Diversity Microstrip Base Station Antenna at 2GHz Using T-Shaped Aperture-Coupled Feeds", IEE Proc.-Microw. Antennas Propag., Vol. 148 No. 5. p334-338, October 2001

[10] S. Gao, L. W. Li, M. S. Leong, and T. S. Yeo, "A Broad-Band Dual-Polarized Microstrip Patch Antenna with Aperture Coupling", IEEE Transactions on Antennas and Propagation, Vol. 51, No. 4, p898-900, April 2003

[11] P. Brachat, J. M. Baracco, "Printed Radiating Element with Two Highly Decoupled Ports", Electronics Letters, Vol. 31, No. 4, p245-246, 16th February 1995

[12] Björn Lindmark, Staffan Lundgren, John R. Sanford, and Claes Beckman, "Dual-Polarized Array for Signal Processing Applications in Wireless Communications". IEEE Transactions on Antennas and Propagation, Vol. 46, No. 6, p758-763, June 1998

[13] L. Habib, G. Kossiavas, and A. Papiernik, "Cross-Shaped Patch with Etched Bars for Dual Polarization", Electronics Letters, Vol. 29, No. 10, p916-918, 13th May 1993

[14] G. S. Parker, Y. M. M. Antar, A. Ittipiboon, and A. Petosa, "Dual-Polarized Microstrip Ring Antenna with Good Isolation", Electronics Letters, Vol. 34, No. 11, p1043-1044, 28th May 1998

[15] S. K. Padhi, N. C. Kamakar Sr., C. L. Law, and S. Aditya Sr., "A Dual-Polarized Aperture-coupled Circular Patch Antenna Using a C-Shaped Coupling Slot", IEEE Transactions on Antennas and Propagation, Vol. 51, No. 12, p3295-3298, December 2003

[16] S. C. Gao, L. W. Li, T. S. Yeo, and M. S. Leong, "Low Cost, Dual Linearly Polarized Microstrip Patch Array", IEE Proc.-Microw. Antennas Propag., Vol. 148, No. 1, p21-24, February 2001

[17] Shun-Shi Zhong, Xue-Xia Yang, Shi-Chang Gao, and Jun-Hai Cui, "Corner-Fed Microstrip Antenna Element and Arrays for Dual-Polarization Operation", IEEE Transactions on Antennas and Propagation, Vol. 50, No. 10, p1473-1480, October 2002

[18] Parbhu D. Patel, "A Dual-Polarized Microstrip Antenna with Low Cross-Polarisation for SAR Applications", Antennas and Propagation Society International Symposium, 1996. AP-S. Digest, Volume 3, 21-26 July 1996 p1536-1539 vol.3

[19] David M. Pozar, Steven D. Tagorski, "A Shared Aperture Dual-Band Dual-Polarized Microstrip Array", IEEE Transactions on Antennas and Propagation, Vol. 49, No. 2, p150-157, February 2001

[20] Andrea Vellecchi, and Guido Biffi Gentili, "Design of Dual-Polarized Series-Fed Microstrip Arrays with Low Losses and High Polarization Purity", IEEE Transactions on Antennas and Propagation, Vol. 53, No. 5, p1791-1798, May 2005

[21] Gobi Vetharatnam, Chung Boon Kuan, and Chuah Hean Teik, "Combined Feed Network for a Shared-Aperture Dual-Band Dual-Polarized Array", IEEE Antennas and Wireless Propagation Letters, Vol. 4, p297-299, 2005

[22] F. Rostan, E. Heidrich, W. Wiesbeck, "Dual-Polarized Multilayer Aperture-Coupled Patch Antennas for Space Borne Application in C and X Band", Antennas and Propagation Society International Symposium, 1994. AP-S. Digest, Volume 1, 20-24 June 1994 p476-479

[23] F. Rostan, W. Wiesbeck, "Dual-Polarized Microstrip Patch Array for the Next Generation of Space Borne Synthetic Aperture Radars", Geoscience and Remote Sensing Symposium, 1995. IGARSS '95. 'Quantitative Remote Sensing for Science and Applications', InternationalVolume 3, 10-14 July 1995 p2277-2279

Chapter 3

Single Dual-Polarized Microstrip Patch Radiating Element

3.1 Introductory Remarks

In this chapter we will consider three geometries of the single element dual-polarized microstrip patch. The only distinction between the geometries under consideration is the routing of the edge-coupled feed network. We will describe the implementation of the dual-polarized microstrip radiating element with maximized port isolation. As mentioned previously the port isolation performance of the microstrip radiating element is greatly affected by the choice of the feed mechanism. The radiating element we will be working with consists of a rectangular microstrip patch that is fed by two different feeding mechanisms (aperture-coupled feed and edge-coupled feed) and two feed networks (one for each of the two signals to be radiated as orthogonally polarized waves). Throughout the thesis we will maintain the following polarization association: edge-coupled feed will be referred to as the horizontally-polarized feed, and aperture-coupled feed will be referred to as the vertically-polarized feed. The matching network used in the edge-coupled feed network consists of an odd number of cascaded quarter wave transformers, while the matching network of the aperture feed consists of a shunt open circuited stub.

The feed network exciting the radiating element through an aperture in the ground plane, by the virtue of this feeding mechanism, is separated from the radiating element by a groundplane and will have an insignificant impact on the port isolation performance of the microstrip antenna element. On the other hand the feed network exciting the radiating element by means of direct contact to one of the edges of the radiating element will reside on the same surface of the substrate as the radiating element. Moreover when integrating the radiating element with this specific excitation arrangement into an array the feed network transmission lines will be routed between the radiating elements within the array, as we will see in Chapter 4, thus increasing the impact of coupling between the radiating

elements and the feed network lines on the isolation performance of the antenna. Having the two feed networks on the opposite sides of the groundplane makes the radiating element the only component via which the cross-coupling between the two orthogonal polarizations can occur (no feed network to feed network coupling). A special care in the feed network design needs only be taken when we are dealing with the edge-coupled feed network. We will investigate how the routing of the edge-coupled feed network lines in the immediate vicinity of the radiating element affects the port isolation levels (as defined in Figure 2) and the polarization orthogonality of the radiated signals by observing $|S_{21}|$ and the cross-polarized radiation patterns of the antenna respectively.

In sections 3.2 through 3.5 we will present the measured patterns for three single microstrip patch radiators with the same aperture-coupled feed layout but different edge-coupled feed layouts. Attention will be focused on the port isolation performance and the cross-polarization levels in the patterns for these three geometries.

3.2 Dual-Polarized Microstrip Patch Element with an Aperture-Coupled Port and an Edge-Coupled Port with a Straight Feed Line

The layout of the dual-polarized microstrip patch element is shown in Figure 29.

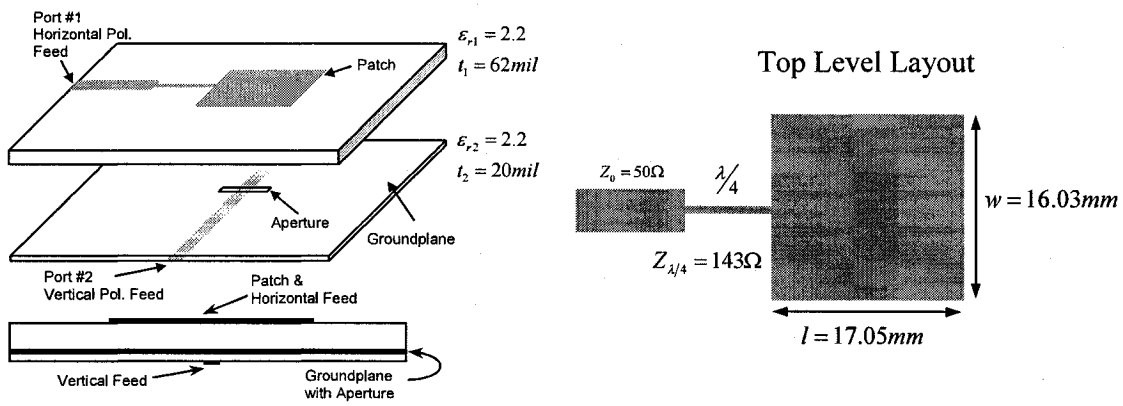

Figure 29 Dual-polarized microstrip patch with a straight edge-coupled feed

Both the edge-coupled feed and the aperture-coupled feed are straight and the directions of the currents on these transmission lines are such that the radiation produced by these lines has the same polarization as the corresponding fields radiated by the microstrip patch

radiator. This layout is symmetrical and it is expected to have good port isolation performance which was confirmed by measured and simulated results shown in Figure 30. In the case of straight edge-coupled feed the excitation current is of the same direction as the radiating current on the patch, therefore if there is some coupling mechanism between the feed network and the radiating patch other than the intended edge coupling the currents induced will be of the same direction as that of the edge-coupling mechanism. The current induced on the patch through coupling between the edge-coupled feed and the patch is parallel with longer dimension of the aperture in the groundplane and will not couple significantly onto the aperture-coupled feed therefore maintaining the high isolation between the ports.

The aperture-coupled feed is separated from the rest of the structure by a ground plane and has very little influence on port isolation or cross-polarization performance of the element. Simulated and measured S-parameters of the radiating element in Figure 29 are shown in Figure 30. The patch resonates at $5.49GHz$ and has impedance bandwidth of 2.6% calculated using $B_{\%} = \frac{B_{VSWR\leq 2}}{f_{res}} 100\%$. The measured port isolation performance is better than $42dB$ over the $1GHz$ frequency span centered at $5.5GHz$. In section 3.6 the performance of this radiating element will be used as a benchmark for the comparison against the performance of radiating element layouts in sections 3.3 and 3.4.

The radiation patterns of the antenna shown in Figure 29 were simulated and measured. The normalized simulated and measured E-plane radiation patterns for the polarization with aperture-coupling are shown in Figure 31. The normalized simulated and measured H-plane radiation patterns of the radiator in Figure 29 for the polarization with aperture-coupling are shown in Figure 32. The normalized simulated and measured E-plane radiation patterns of the radiator in Figure 29 for the polarization with edge-coupling are shown in Figure 33. The normalized simulated and measured H-plane radiation patterns of the radiator in Figure 29 for the polarization with edge-coupling are shown in Figure 34.

Measured and simulated magnitudes of S-parameters for the radiating element in Figure 29 are shown in Figure 30.

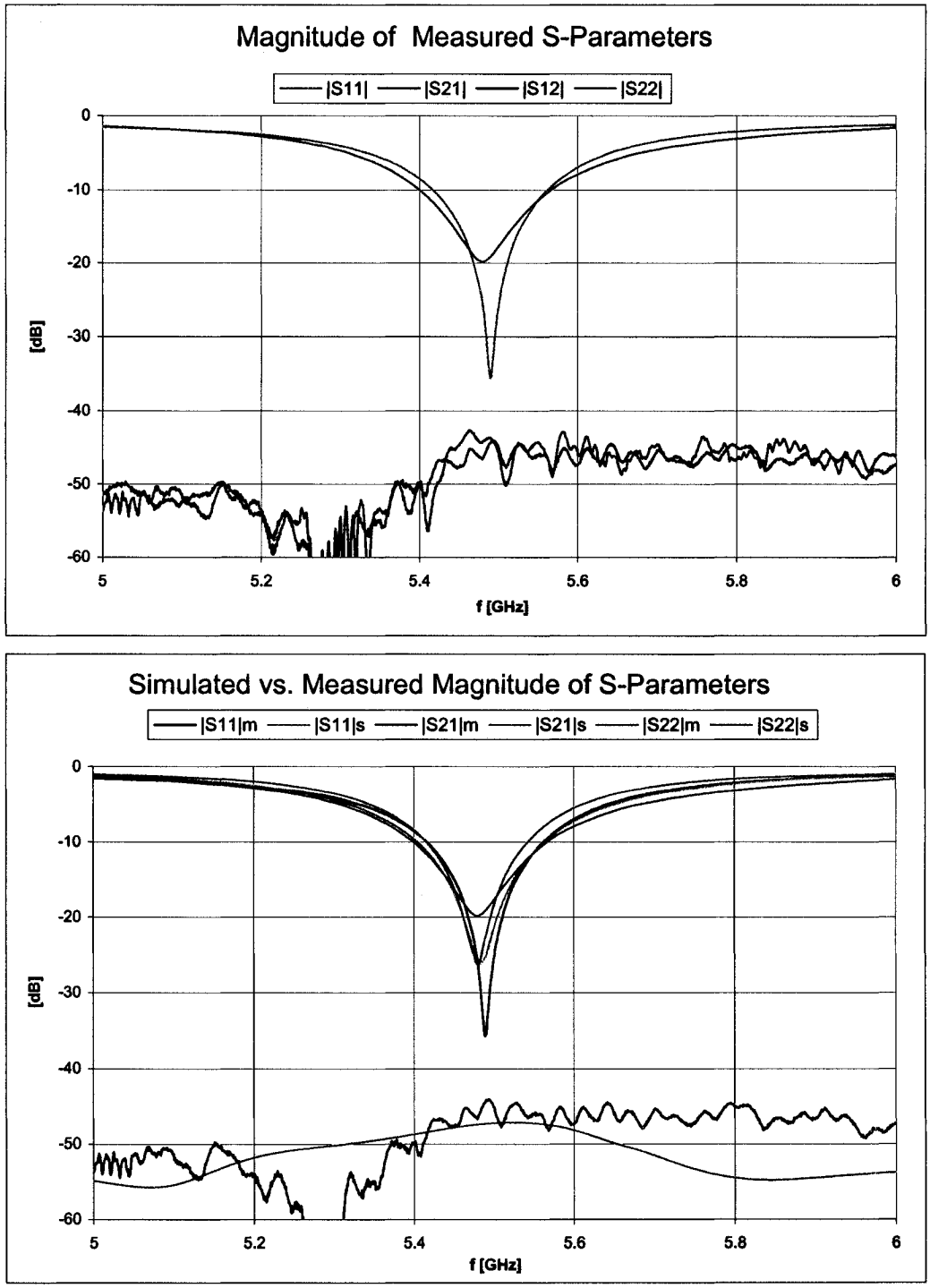

Figure 30 S-Parameters for dual-polarized microstrip patch with a straight edge-coupled feed

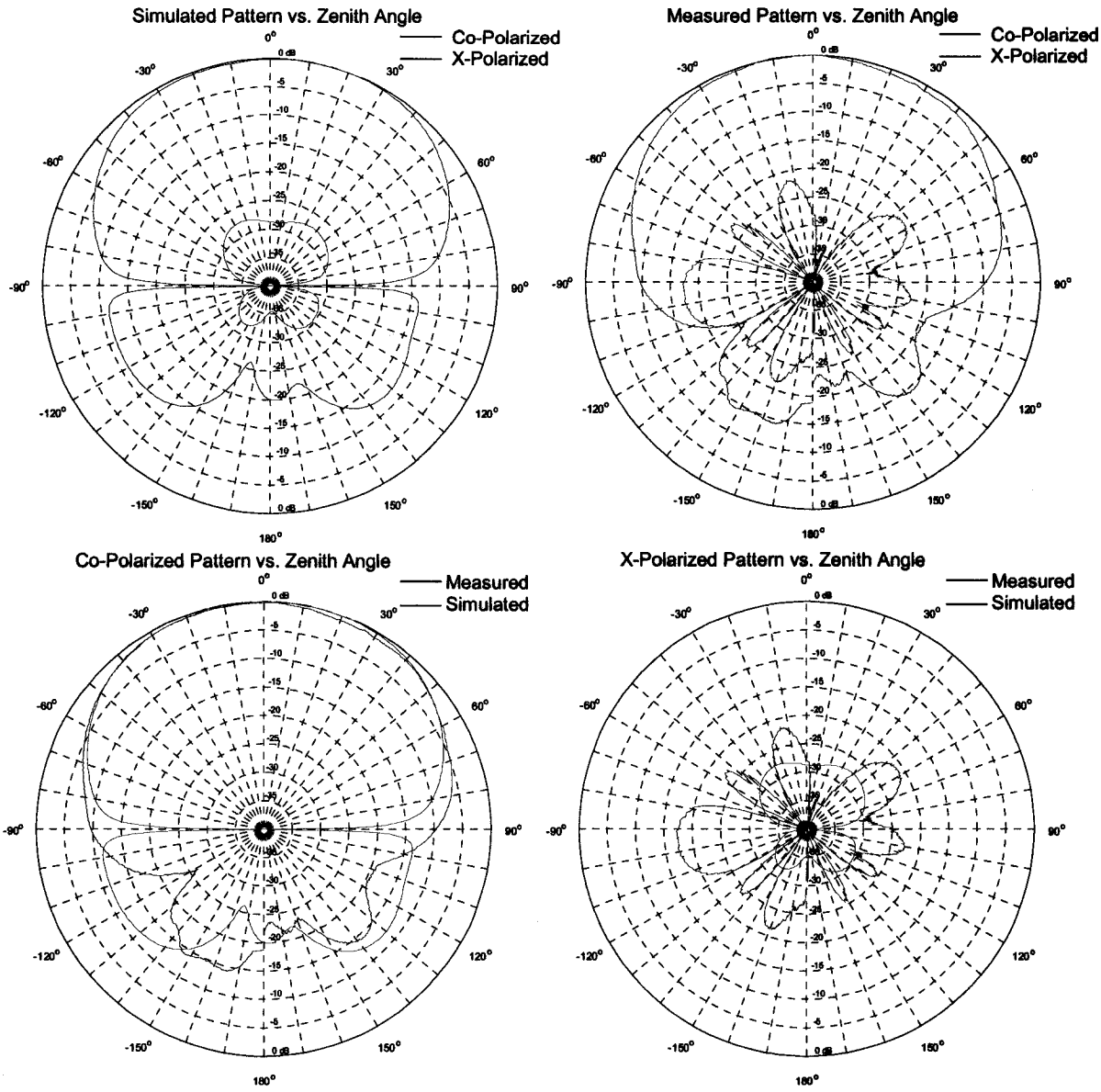

Figure 31 Normalized aperture-coupled polarization E-plane radiation patterns of the microstrip patch with a straight edge-coupled feed

The results for radiation patterns in Figure 31 are summarized in Table 1.

Table 1 Summary of aperture-coupled polarization E-plane radiation pattern parameters of the microstrip patch with a straight edge-coupled feed

	3dB Beamwidth	Max X-Pol Level ($\|\theta\| \leq 60°$)	Front to Back Ratio	Back Lobe ($\|\theta\| \geq 120°$)
Simulated	106°	-27.6dB @ -30°	20.1dB	-11.3dB @-115°
Measured	107°	-21.7dB @ -13°	20.0dB	-14.1dB @ -148°

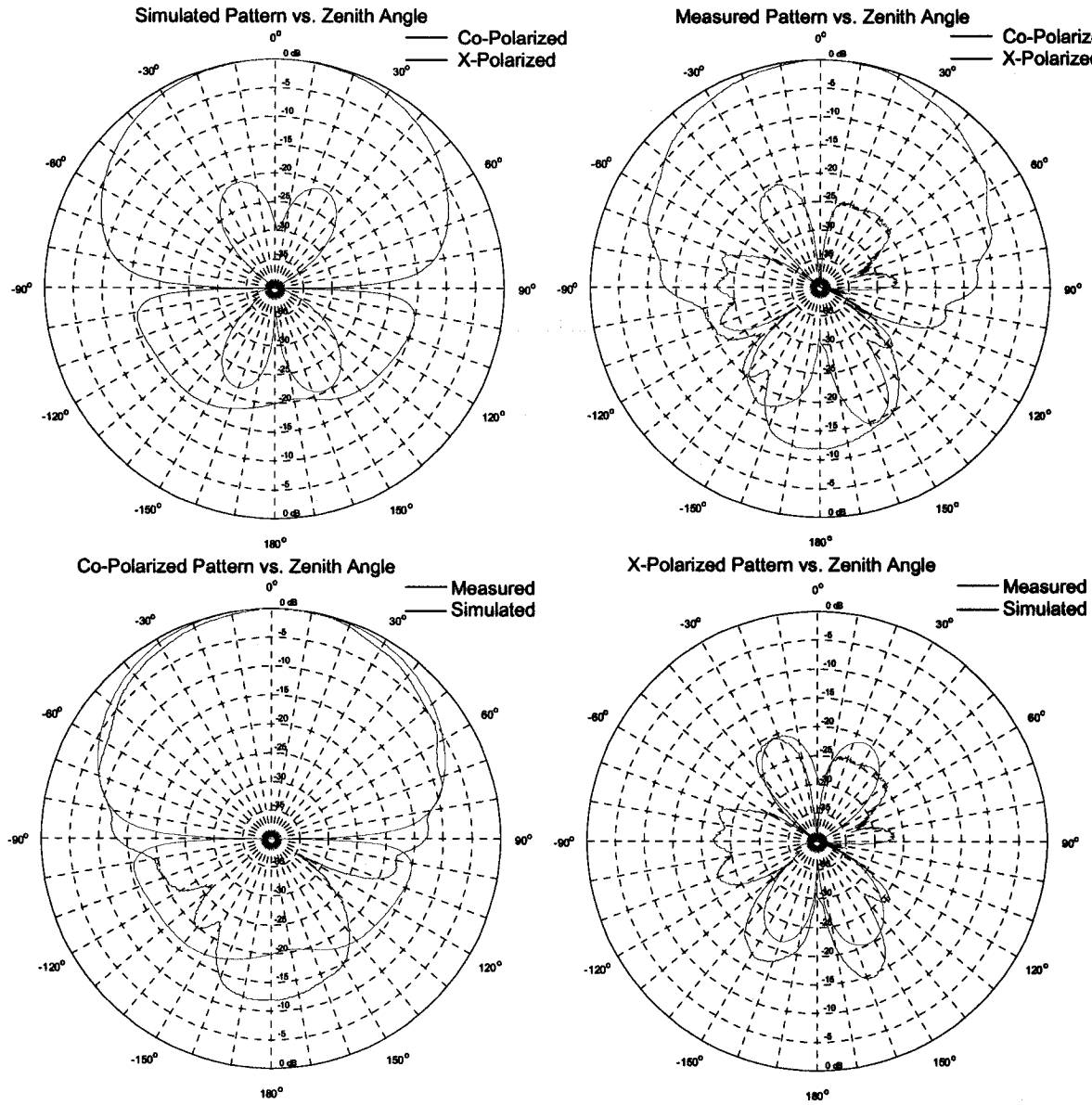

Figure 32 Normalized aperture-coupled polarization H-plane radiation patterns of the microstrip patch with a straight edge-coupled feed

The results for radiation patterns in Figure 32 are summarized in Table 2.

Table 2 Summary of aperture-coupled polarization H-plane radiation pattern parameters of the microstrip patch with a straight edge-coupled feed

	3dB Beamwidth	Max X-Pol Level ($\|\theta\| \leq 60°$)	Front to Back Ratio	Back Lobe ($\|\theta\| \geq 120°$)
Simulated	95°	-20.5dB @ -20°	20.0dB	-16.4dB @-135°
Measured	80°	-20.5dB @ -23°	12.0dB	-12.0dB @ 180°

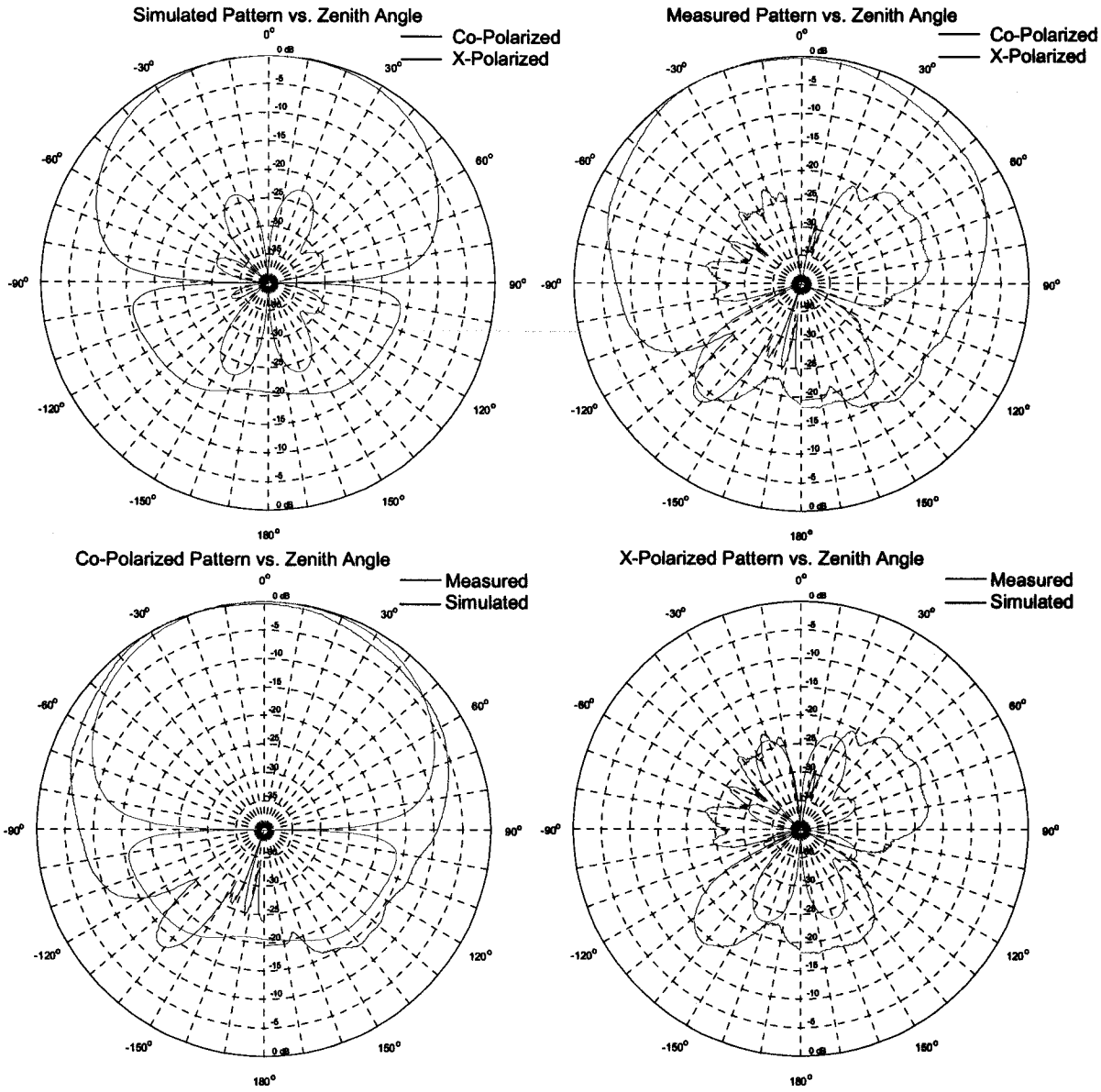

Figure 33 Normalized edge-coupled polarization E-plane radiation patterns of the microstrip patch with a straight edge-coupled feed

The results for radiation patterns in Figure 33 are summarized in Table 3.

Table 3 Summary of edge-coupled polarization E-plane radiation pattern parameters of the microstrip patch with a straight edge-coupled feed

	3dB Beamwidth	Max X-Pol Level ($\|\theta\| \leq 60°$)	Front to Back Ratio	Back Lobe ($\|\theta\| \geq 120°$)
Simulated	96°	-22.6dB @ 21°	20.7dB	-17.2dB @ -140°
Measured	100°	-16.8dB @ 60°	21.0dB	-12.7dB @ -139°

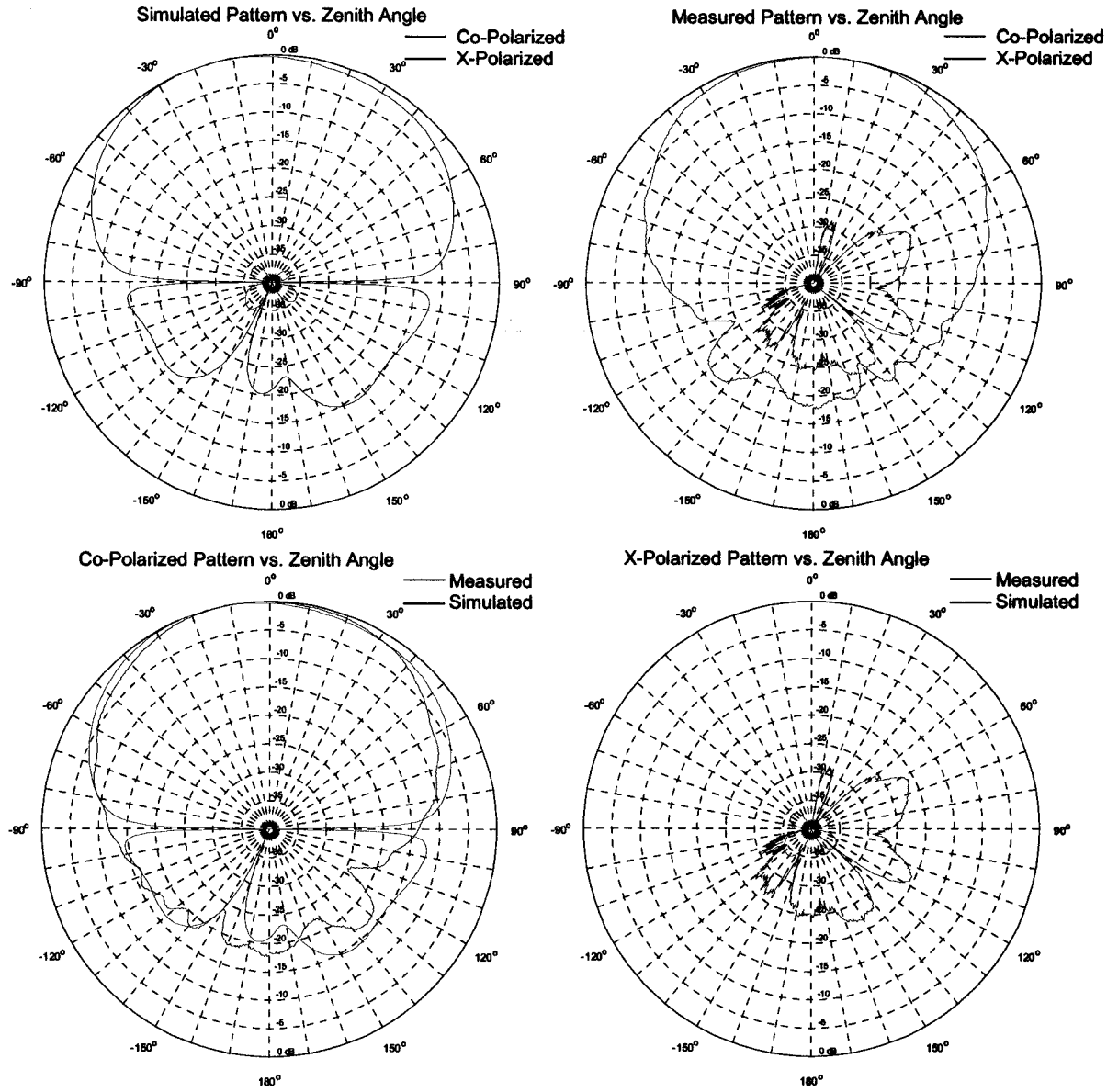

Figure 34 Normalized edge-coupled polarization H-plane radiation patterns of the microstrip patch with a straight edge-coupled feed

The results for radiation patterns in Figure 34 are summarized in Table 4.

Table 4 Summary of edge-coupled polarization H-plane radiation pattern parameters of the microstrip patch with a straight edge-coupled feed

	3dB Beamwidth	Max X-Pol Level ($\|\theta\| \leq 60°$)	Front to Back Ratio	Back Lobe ($\|\theta\| \geq 120°$)
Simulated	109°	-35.8dB @ -55°	21.0dB	-14.4dB @ 143°
Measured	89°	-21.5dB @ -60°	18.0dB	-16.2dB @ -133°

3.3 Dual-Polarized Microstrip Patch Element with an Aperture-Coupled Port and an Edge-Coupled Port with a Single-Bend Feed Line

Since our ultimate goal is to use this dual-polarized microstrip patch element in an array environment we will not be able to maintain the degree of symmetry exhibited by the straight feed layout presented previously. The bends in the feed network transmission lines will need to be introduced and we will investigate the effects these routing bends will have on the port isolation performance of our dual-polarized microstrip patch element. Dual-polarized microstrip patch element with a single bend in the horizontal feed line was obtained by bending the quarter-wave matching section of the horizontal feed line into a quarter-circle to produce the layout shown in figure below.

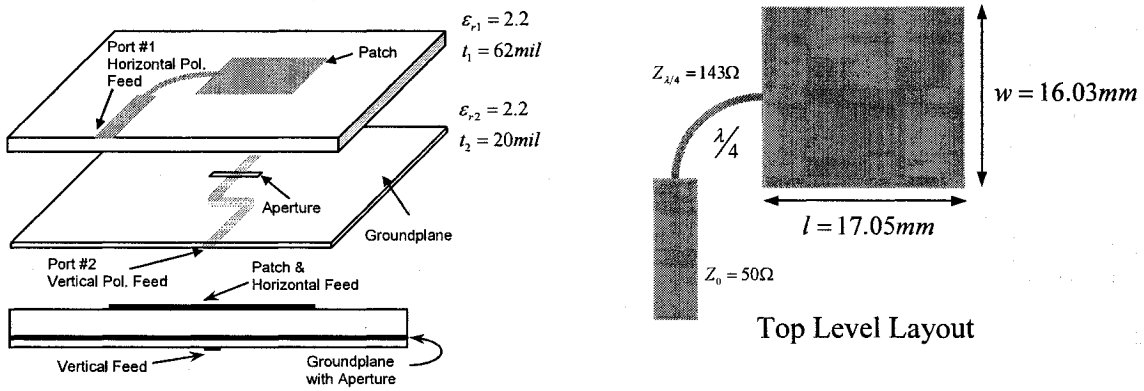

Figure 35 Dual-polarized microstrip patch with a single bend in the edge-coupled feed

The layout of the top layer (horizontal feed and the radiating patch) is no longer symmetrical with respect to the horizontal axis. The lack of the symmetry causes degradation in the isolation performance compared to the radiating element with straight feeds, which was confirmed by both measured and simulated results shown in Figure 37. The 50Ω portion of the feed line is vertical and so is the excitation current it carries. The coupling between the transmission line and the radiating patch due to proximity in routing will induce vertically oriented current on the radiating element, thus degrading the port isolation performance. Also, the radiation from the feed will be vertically polarized and will cause an increase in cross-polarization levels. The aperture-coupled feed is separated from

the rest of the circuit by a ground plane and has very little influence on port isolation or cross-polarization performance of the element.

Simulated and measured S-parameters of the radiating element in Figure 35 are shown in Figure 37. The patch resonates at $5.47GHz$ and has impedance bandwidth of 2.5% calculated using $B_{\%} = \frac{B_{VSWR\leq 2}}{f_{res}} 100\%$. The measured port isolation performance is better than $16dB$ over the $1GHz$ frequency span centered at $5.5GHz$. The element with the single bend in the edge-coupled feed has $28dB$ lower port isolation performance than the element with the straight edge-coupled feed. If we were to rely solely on the port isolation performance of the element with this feed network routing to provide us with good isolation in the array environment we would fail to achieve good results.

To explain the poor port isolation performance for this layout we will consider a pair of current elements on the vertical portion of the edge-coupled feed in Figure 36.

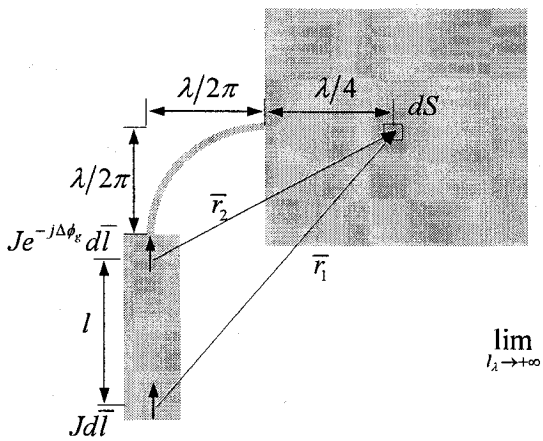

$$\varepsilon_g = \varepsilon_0 = \varepsilon_{eff}$$

$$path1 = \sqrt{\left(\frac{\lambda}{4}+\frac{\lambda}{2\pi}\right)^2 + \left(\frac{\lambda}{2\pi}+l_\lambda\right)^2}$$

$$path2 = \sqrt{\left(\frac{\lambda}{4}+\frac{\lambda}{2\pi}\right)^2 + \left(\frac{\lambda}{2\pi}\right)^2} + l_\lambda$$

$$\lim_{l_\lambda \to +\infty} \Delta\phi = \lim_{l_\lambda \to +\infty} \left[(path2 - path1)\frac{360^\circ}{\lambda} \right] \approx 100^\circ < 120^\circ$$

Figure 36 The cross-coupling contributions from the vertical portion of the feed network with a single bend in the edge-coupled feed

The magnitude of the current elements is the same and the phase difference $\Delta\phi_g$ between the elements is due to their separation l on the transmission line. Each current element will induce vertically oriented current at differential area dS on the microstrip patch. The phase of the induced current due to each element will depend on the phase of the current element and the phase delay due to distances $|\bar{r}_1|$ and $|\bar{r}_2|$ of the current element from the observation point at the center of dS. The coupling contributions from these current elements will

combine constructively if their phase difference is close to zero or they will combine destructively if the phase difference is close to 180°. If we have equal magnitude contributions the combination of the two will be smaller than the individual contribution if the phase difference between the two is larger than 120°. The phase difference between the two contributions in Figure 36 is given by $\Delta\phi = \Delta\phi_g + \Delta\phi_0$, where $\Delta\phi_g$ is the phase difference between the current elements, and $\Delta\phi_0$ is the phase difference due to the different path lengths between the current elements and the observation point. Assuming that guided and coupled effective relative dielectric constants (ε_g and ε_0 respectively) are equal we find that the phase difference $\Delta\phi$ due to difference in electrical lengths of paths 1 and 2 from Figure 36 is less than 120°. Although path r_1 is longer than r_2, this is compensated for by $\Delta\phi_g$, namely $\Delta\phi = \phi_{r1} - (\phi_{r2} + \Delta\phi_g)$. Thus even the two most widely separated current elements in the geometry shown in Figure 36 will combine to yield increase in the overall cross-coupling. This argument is only valid for relatively short vertical portion of the transmission line. If a longer line is considered, then the magnitude of the coupling will decrease with increasing distance between the current element and the radiating patch. The cross-coupling contributions from the current elements in the immediate vicinity of the patch will dominate. To obtain overall cross-coupling the contributions due to all current element pairs along the vertical portion of the feed network transmission line will need to be added. The above argument explains why simulated and measured performances of the radiating element in Figure 35 are significantly degraded compared to the radiating element in Figure 29. Also we get the insight into the impact that vertical sections of the horizontal polarization feed network have on the port isolation performance of the dual-polarized microstrip patch.

The radiation patterns of the antenna shown in Figure 35 were simulated and measured. The normalized simulated and measured E-plane radiation patterns for the polarization with aperture-coupling are shown in Figure 38. The normalized simulated and measured H-plane radiation patterns of the radiator in Figure 35 for the polarization with aperture-coupling are shown in Figure 39. The normalized simulated and measured E-plane radiation patterns of the radiator in Figure 35 for the polarization with edge-coupling are shown in Figure 40. The normalized simulated and measured H-plane radiation patterns of the radiator in Figure 35 for the polarization with edge-coupling are shown in Figure 41.

Simulated and measured S-parameters of the radiating element in Figure 35 are shown in Figure 37.

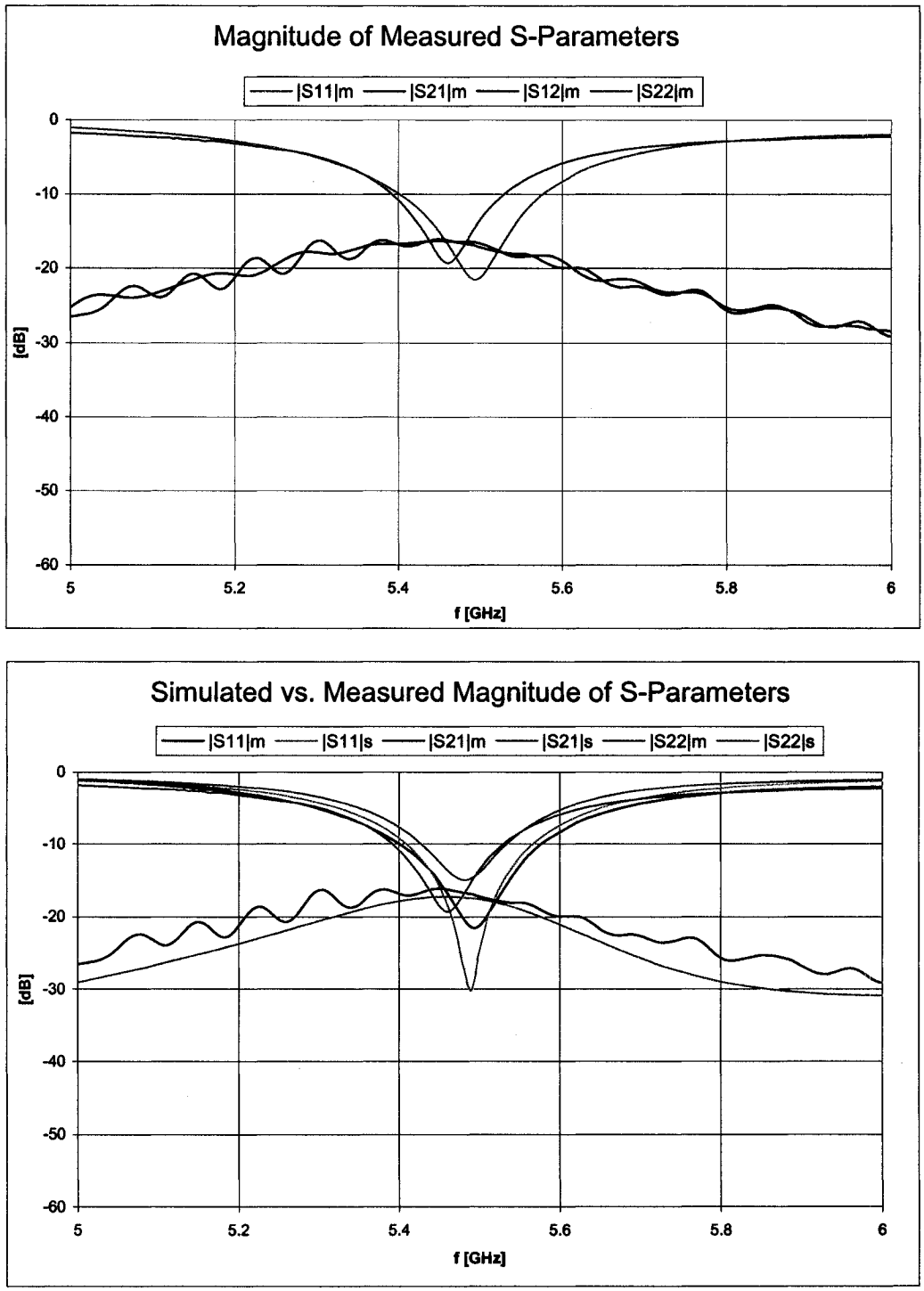

Figure 37 S-Parameters for dual-polarized microstrip patch with a single bend in the edge-coupled feed

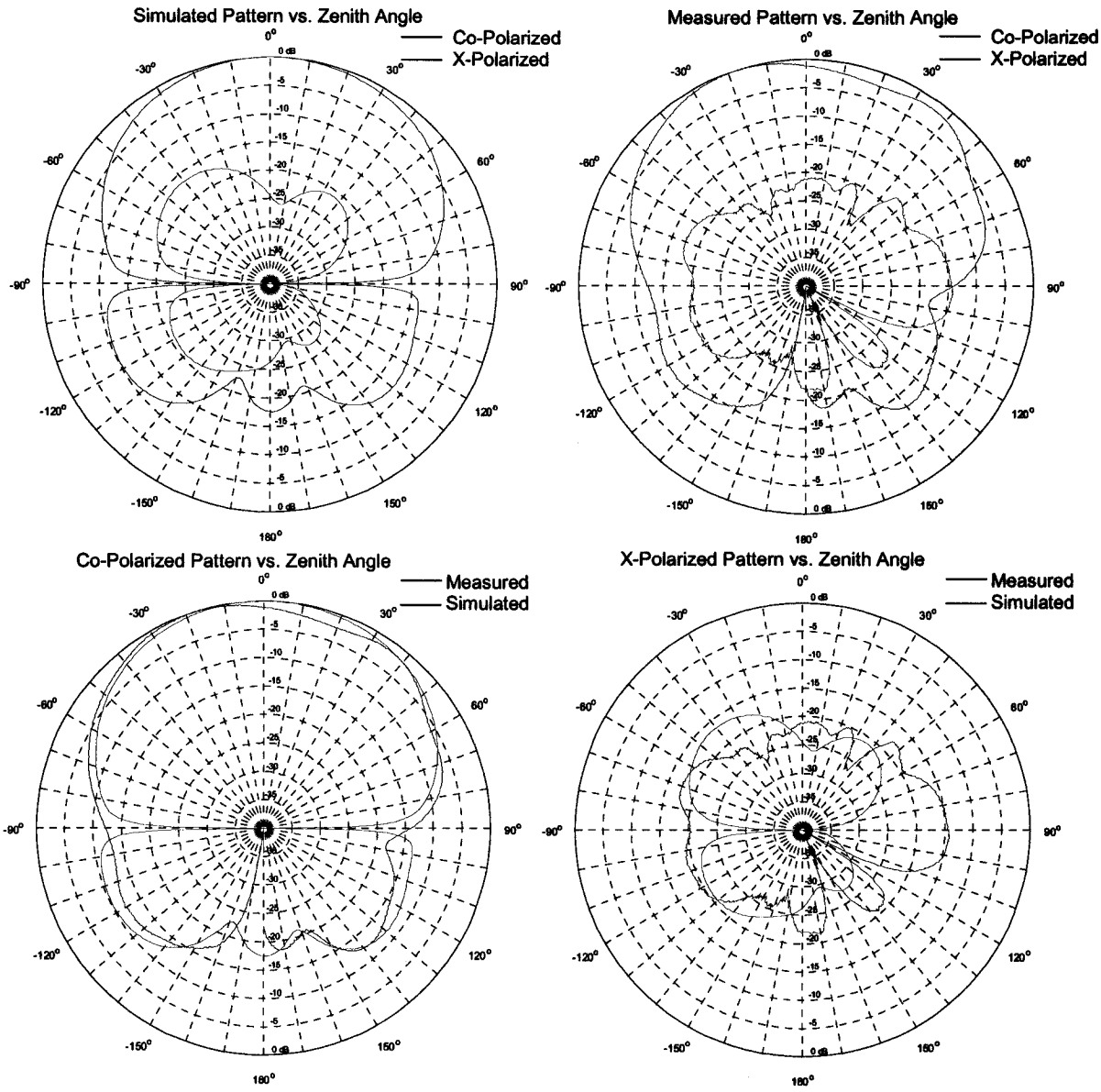

Figure 38 Normalized aperture-coupled polarization E-plane radiation patterns of the microstrip patch with a single bend in the edge-coupled feed

The results for radiation patterns in Figure 38 are summarized in Table 5.

Table 5 Summary of aperture-coupled polarization E-plane radiation pattern parameters of the microstrip patch with a single bend in the edge-coupled feed

	3dB Beamwidth	Max X-Pol Level ($\|\theta\| \leq 60°$)	Front to Back Ratio	Back Lobe ($\|\theta\| \geq 120°$)
Simulated	92°	-16.4dB @ -40°	17.6dB	-10.3dB @ -120°
Measured	95°	-17.7dB @ 48°	22.0dB	-12.3dB @ 136°

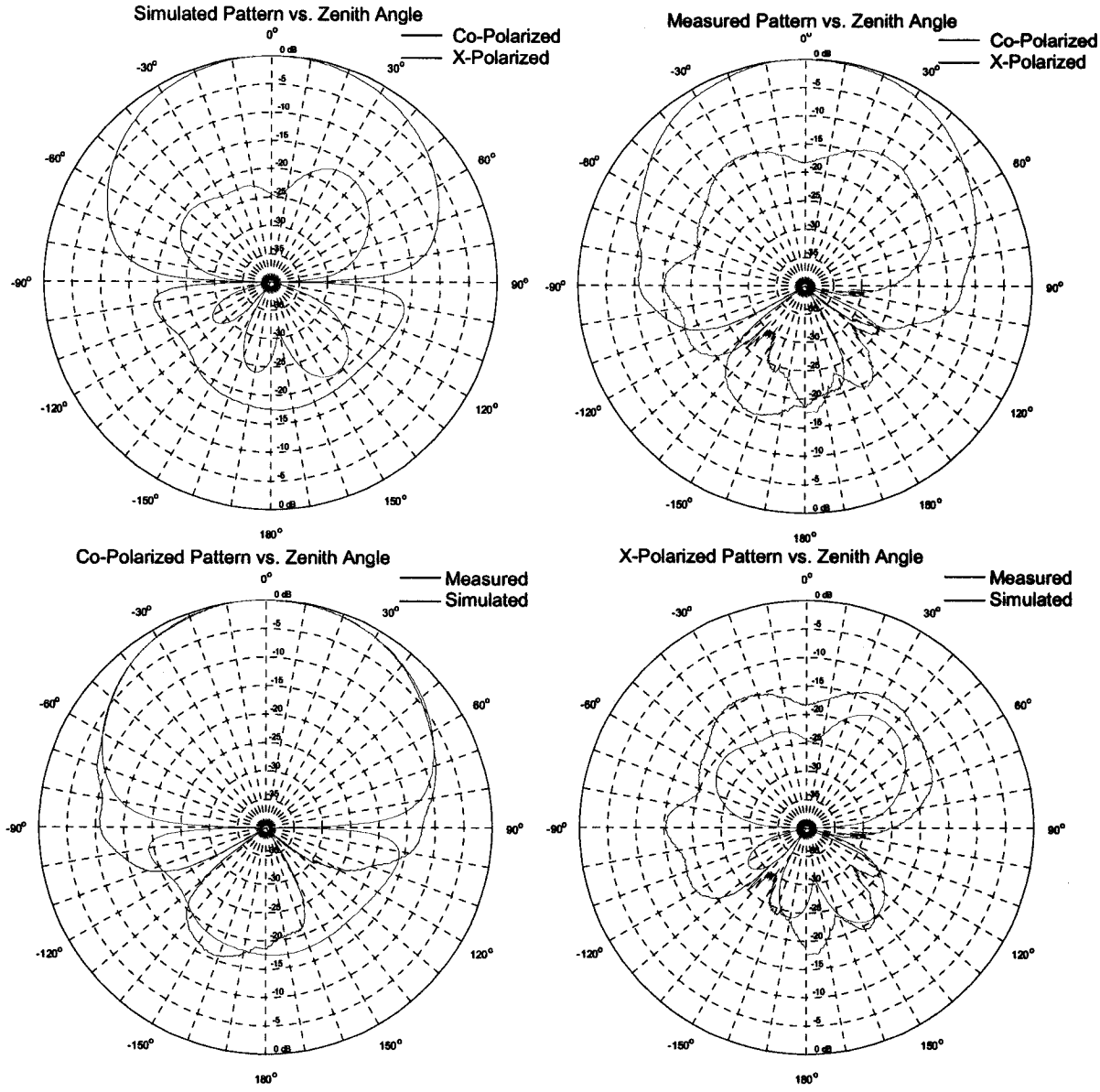

Figure 39 Normalized aperture-coupled polarization H-plane radiation patterns of the microstrip patch with a single bend in the edge-coupled feed

The results for radiation patterns in Figure 39 are summarized in Table 6.

Table 6 Summary of aperture-coupled polarization H-plane radiation pattern parameters of the microstrip patch with a single bend in the edge-coupled feed

	3dB Beamwidth	Max X-Pol Level ($\|\theta\| \leq 60°$)	Front to Back Ratio	Back Lobe ($\|\theta\| \geq 120°$)
Simulated	86°	-16.8dB @ 37°	17.6dB	-17.6dB @ 180°
Measured	84°	-13.0dB @ 30°	18.6dB	-15.9dB @ -160°

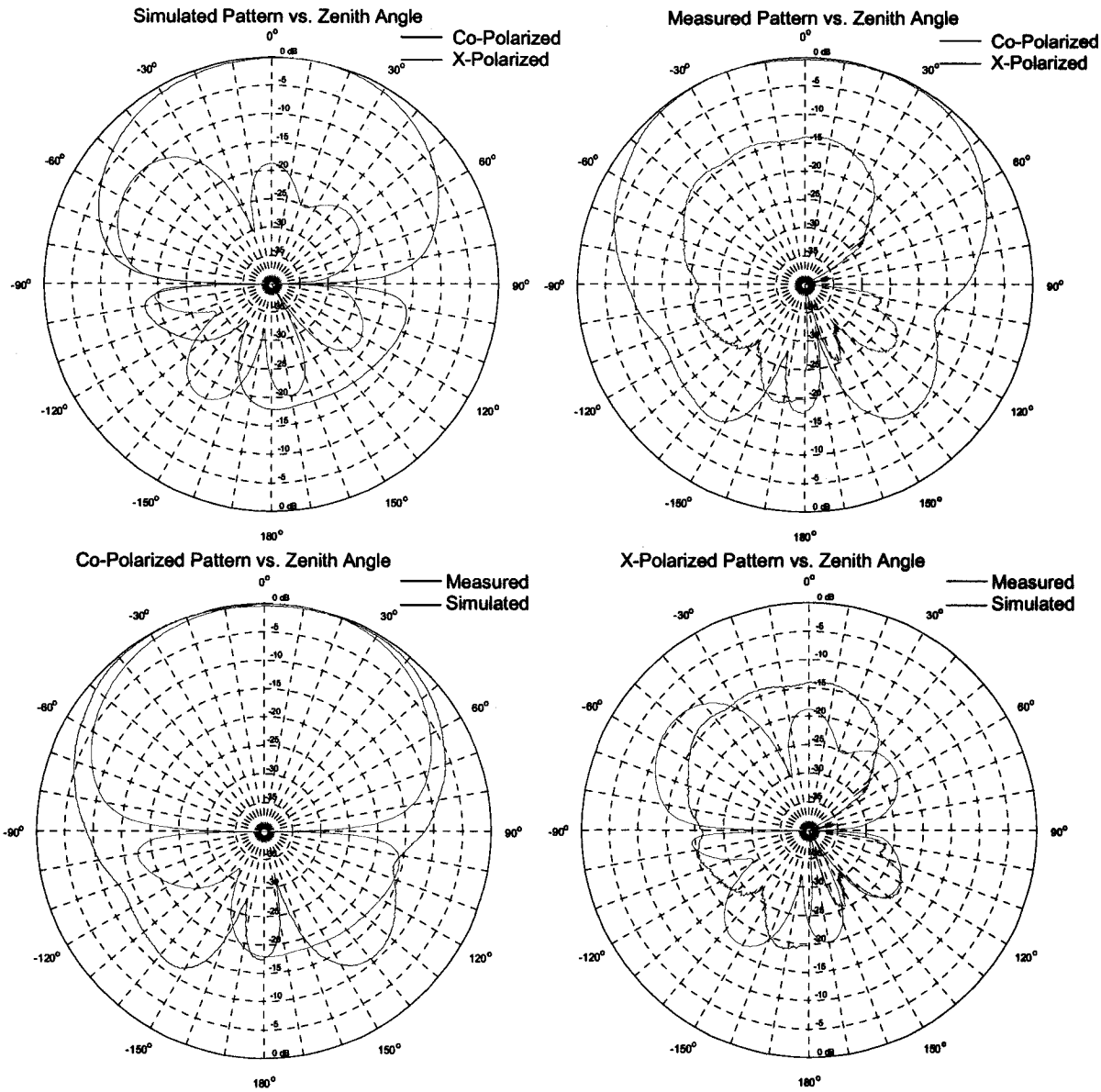

Figure 40 Normalized edge-coupled polarization E-plane radiation pattern parameters of the microstrip patch with a single bend in the edge-coupled feed

The results for radiation patterns in Figure 40 are summarized in Table 7.

Table 7 Summary of edge-coupled polarization E-plane radiation pattern parameters of the microstrip patch with a single bend in the edge-coupled feed

	3dB Beamwidth	Max X-Pol Level ($\|\theta\| \leq 60°$)	Front to Back Ratio	Back Lobe ($\|\theta\| \geq 120°$)
Simulated	93°	-9.5dB @ -53°	18.0dB	-18.0 @ 180°
Measured	115°	-14.0dB @ 0°	17.5dB	-10.7 @ 139°

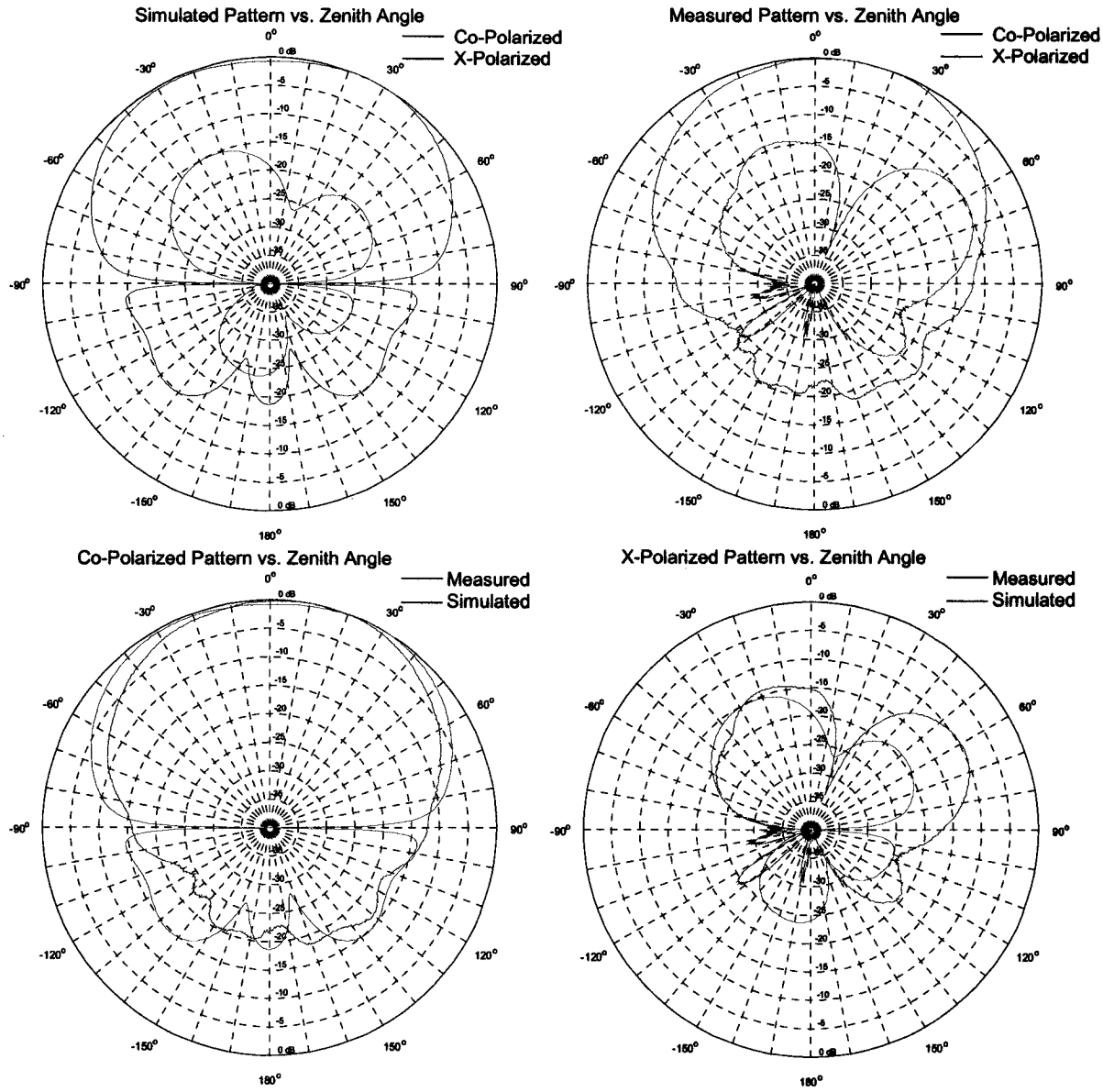

Figure 41 Normalized edge-coupled polarization H-plane radiation patterns of the microstrip patch with a single bend in the edge-coupled feed

The results for radiation patterns in Figure 41 are summarized in Table 8.

Table 8 Summary of edge-coupled polarization H-plane radiation pattern parameters of the microstrip patch with a single bend in the edge-coupled feed

	3dB Beamwidth	Max X-Pol Level ($\|\theta\| \leq 60°$)	Front to Back Ratio	Back Lobe ($\|\theta\| \geq 120°$)
Simulated	112°	-15.1dB @ -30°	18.7dB	-14.8dB @ 135°
Measured	83°	-9.6dB @ -60°	22.1dB	-16.1dB @ 131°

3.4 Dual-Polarized Microstrip Patch Element with an Aperture-Coupled Port and an Edge-Coupled Port with a Three-Bend Feed Line

In an attempt to improve the poor port isolation performance caused by the presence of a single bend in the horizontal feed network we are going to introduce a feed network that consists of three cascaded quarter-wave transformers folded into a "U" shape with a total of three bends in the edge-coupled feed network. The dimensions of the sections of the matching network are optimized in such a way that the port isolation performance is maximized. The layout is shown in Figure 42.

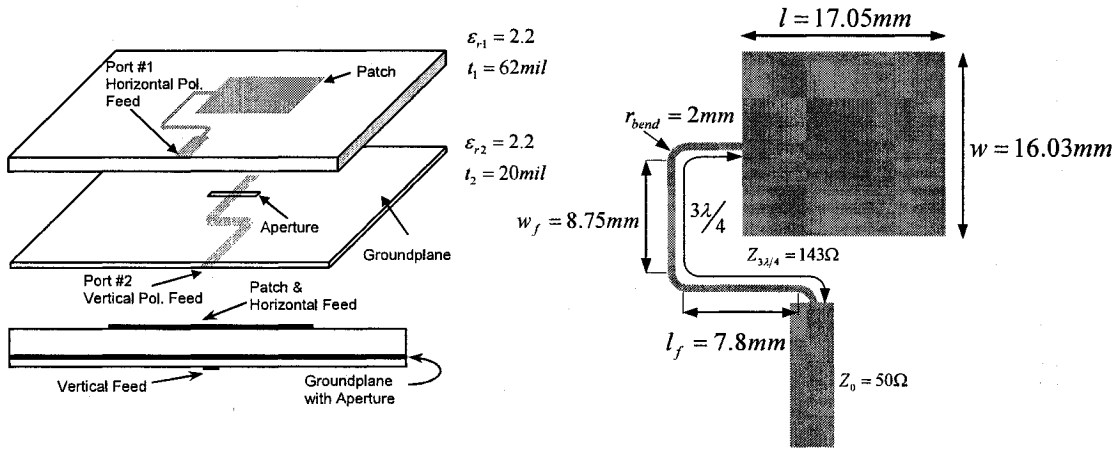

Figure 42 Dual-polarized microstrip patch with three bends in the edge-coupled feed

The cross coupling between the radiating element and vertical portions of the feed network was minimized by cascading three quarterwave transformers and bending them into a "U"-shape as shown in Figure 42. The dimensions w_f and l_f of the "U"-shaped matching network are optimized in order to maximize the port isolation. Simulated and measured S-parameters of the radiating element in Figure 42 are shown in Figure 45. The patch resonates at $5.48GHz$ and has impedance bandwidth of 2.4% calculated using $B_{\%} = \frac{B_{VSWR\leq 2}}{f_{res}} 100\%$. The measured port isolation performance is better than $36dB$ over the impedance bandwidth.

The element with the folded edge-coupled feed has $20dB$ higher port isolation performance than the element with a single bend in the edge-coupled feed. To explain the improvement in port isolation performance for this layout we will consider a pair of current elements on the vertical portions of the edge-coupled feed shown in Figure 43.

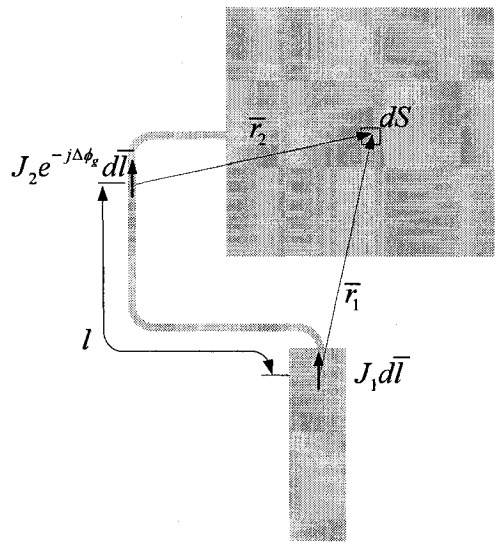

Figure 43 The cross-coupling contributions from the vertical portions of the feed network with three bends in the edge-coupled feed

The currents on the vertical portions of the folded edge-coupled feed will induce vertically oriented currents on the radiating element thus causing the unwanted cross-coupling between the feed and the radiating element and, in the process, lowering the port isolation. The amount of cross-coupling depends on whether the cross-coupling contributions from the individual current elements like $J_1d\bar{l}$ and $J_2e^{-j\Delta\phi_g}d\bar{l}$ in Figure 43 will combine constructively or destructively. The current magnitudes J_1 and J_2 depend on the incident power and standing waves formed by the impedance mismatches. The phase difference between the current elements $J_1d\bar{l}$ and $J_2e^{-j\Delta\phi_g}d\bar{l}$ due to their separation l on the transmission line is $\Delta\phi_g$. The difference in path lengths between individual current elements and the observation point $\left(|\bar{r}_1|-|\bar{r}_2|\right)$ will produce the difference in the path phase delay $\Delta\phi_0$. If the geometry of the "U" fold changes so will the parameters affecting the

amount of the unwanted cross-coupling: J_2, $\Delta\phi_g$, $\Delta\phi_0$, $|\overline{r}_1|$, and $|\overline{r}_2|$. By altering the dimensions w_f and l_f of the "U"-shaped matching network in Figure 42 the positioning of vertical portions of the feed network relative to the radiating element can be adjusted so that the unwanted cross-coupling contributions from these sections of the feed network combine destructively yielding maximized port isolation performance.

To substantiate our conjecture we performed a numerical experiment shown in Figure 44. The S-parameters of the original geometry were simulated and at 5.5GHz and we obtained port isolation of 45dB in Figure 44a. Then the upper horizontal portion of the feed network is removed and the feed is terminated in the impedance corresponding to the input impedance of the original geometry at the location of port 3. For the geometry in Figure 44b the port isolation is found to be 44dB. Next we remove the first bend as shown in Figure 44c and find that the port isolation has decreased to 41dB. By removing the vertical portion of the folded matching network as shown in Figure 44d we find that port isolation falls to 24dB which means that vertical portion of the matching network has significant influence on the port isolation performance. As the next step we reduced the length of the 50Ω feed line as shown in Figure 44e and we find the port isolation to be 37dB. Keeping the 50Ω feed line short we restore the vertical portion of the matching network to its original length as shown in Figure 44f the port isolation falls to 27dB. Effects of the 50Ω feed line length on the port isolation are shown in Figure 44g and Figure 44h. When we have both vertical sections present the port isolation is high, the same is true if both vertical sections are removed. The port isolation gets low when only one of the vertical sections is present and the other one is removed. This confirms that cross-coupling contributions from two vertical sections combine destructively. Previous analysis has been used as a guideline in optimization of the feed network dimensions w_f and l_f in Figure 42.

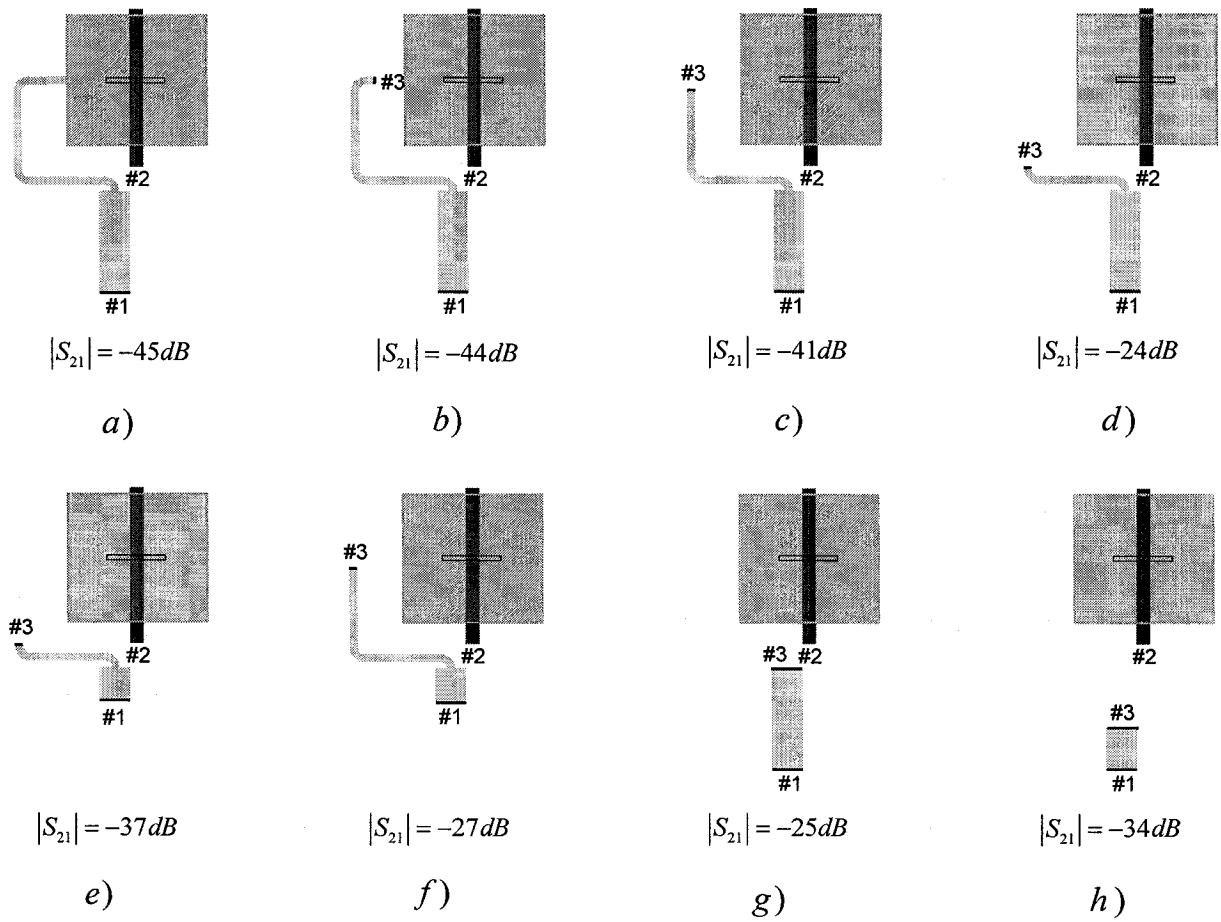

Figure 44 Effects of various portions of the feed network on the port isolation at f=5.5GHz

The radiation patterns of the antenna shown in Figure 42 were simulated and measured. The normalized simulated and measured E-plane radiation patterns for the polarization with aperture-coupling are shown in Figure 46. The normalized simulated and measured H-plane radiation patterns of the radiator in Figure 42 for the polarization with aperture-coupling are shown in Figure 47. The normalized simulated and measured E-plane radiation patterns of the radiator in Figure 42 for the polarization with edge-coupling are shown in Figure 48. The normalized simulated and measured H-plane radiation patterns of the radiator in Figure 42 for the polarization with edge-coupling are shown in Figure 49.

Simulated and measured S-parameters of the radiating element in Figure 42 are shown in Figure 45.

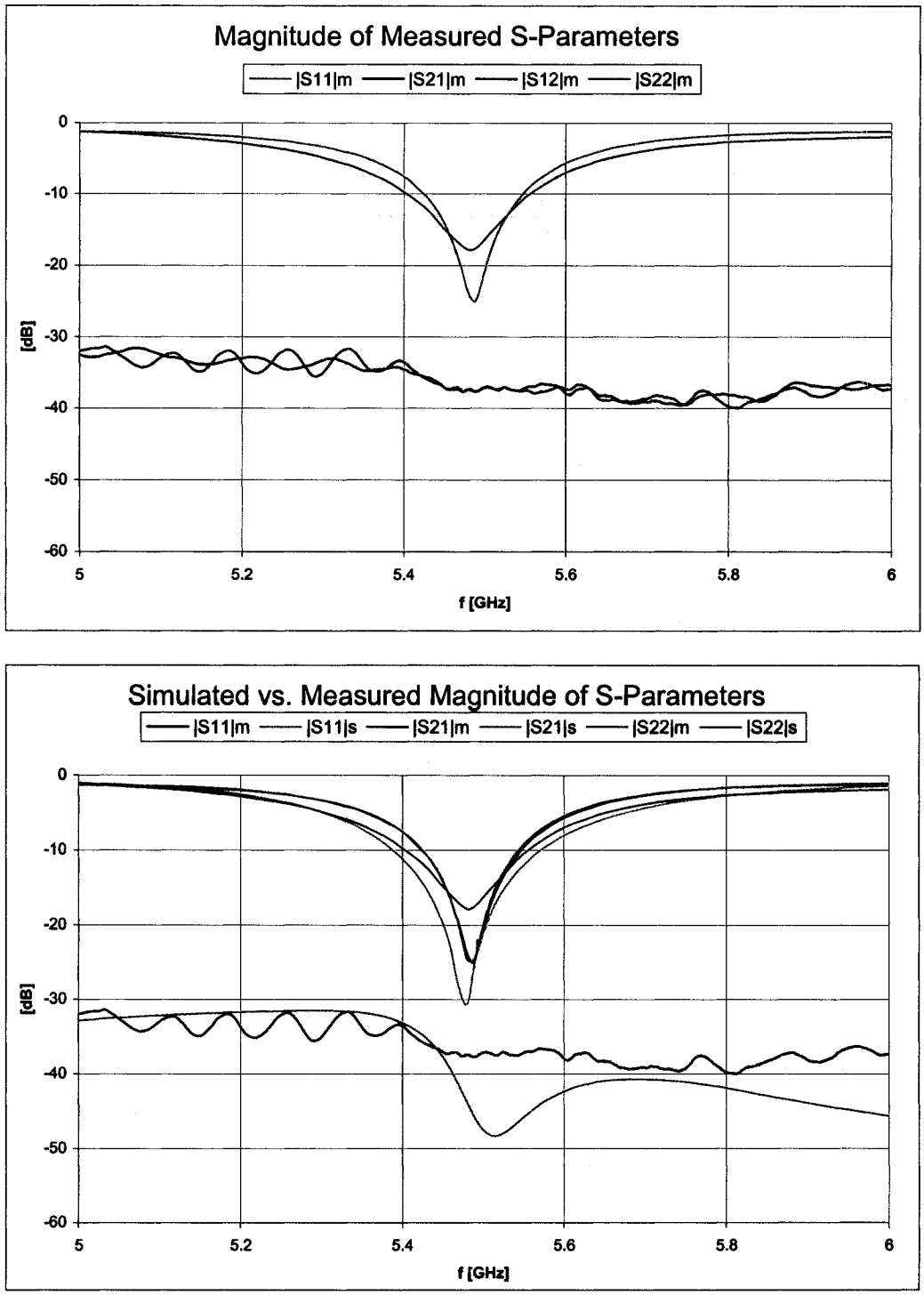

Figure 45 S-Parameters for dual-polarized microstrip patch with three bends in the edge-coupled feed

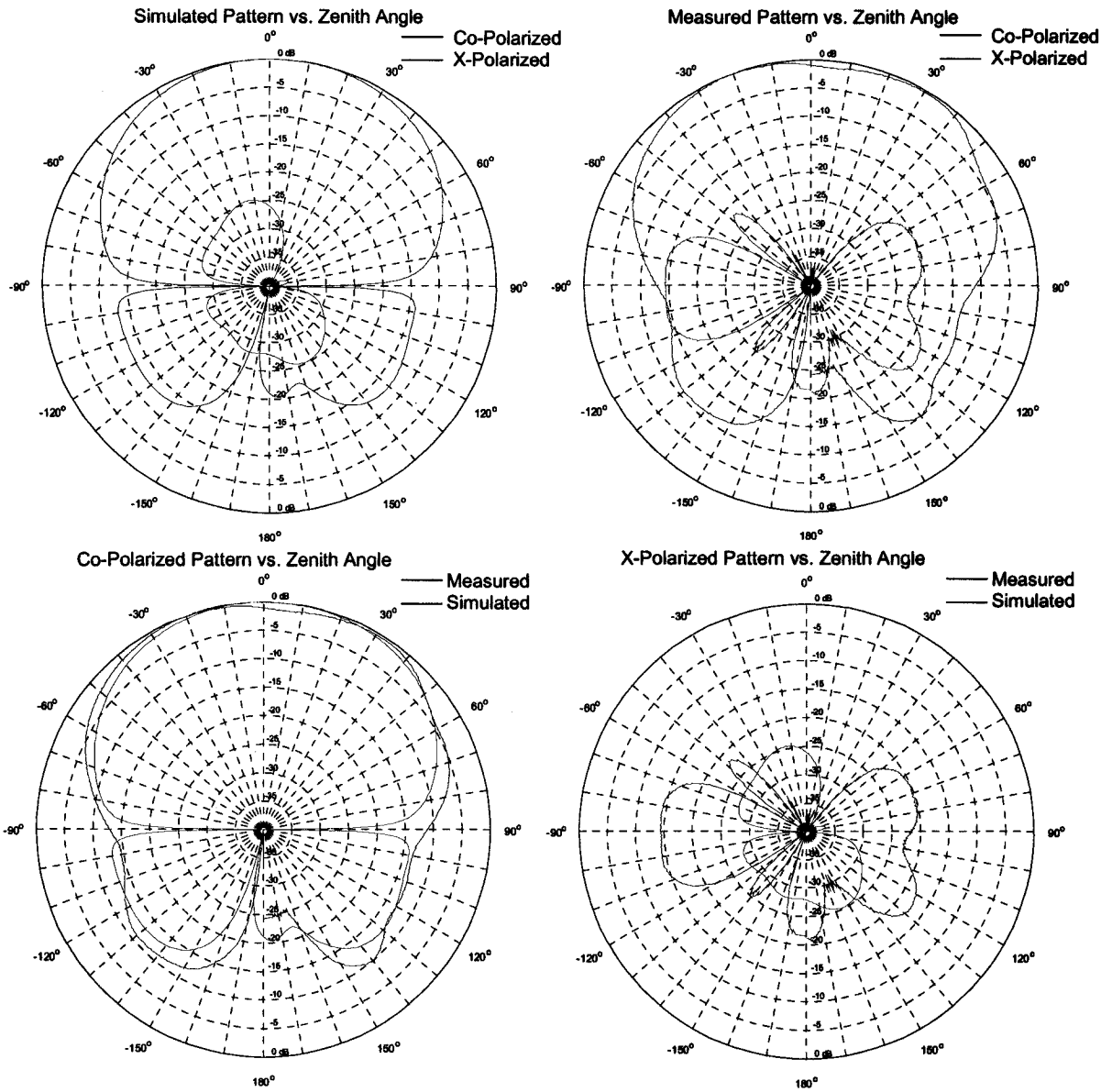

Figure 46 Normalized aperture-coupled polarization E-plane radiation patterns of the microstrip patch with three bends in the edge-coupled feed

The results for radiation patterns in Figure 46 are summarized in Table 9.

Table 9 Summary of aperture-coupled polarization E-plane radiation pattern parameters of the microstrip patch with three bends in the edge-coupled feed

	3dB Beamwidth	Max X-Pol Level ($\|\theta\| \leq 60°$)	Front to Back Ratio	Back Lobe ($\|\theta\| \geq 120°$)
Simulated	94°	-24.5dB @ -15°	21.2dB	-12.9dB @ -130°
Measured	103°	-20.6dB @ -60°	24.4dB	-10.1dB @ 140°

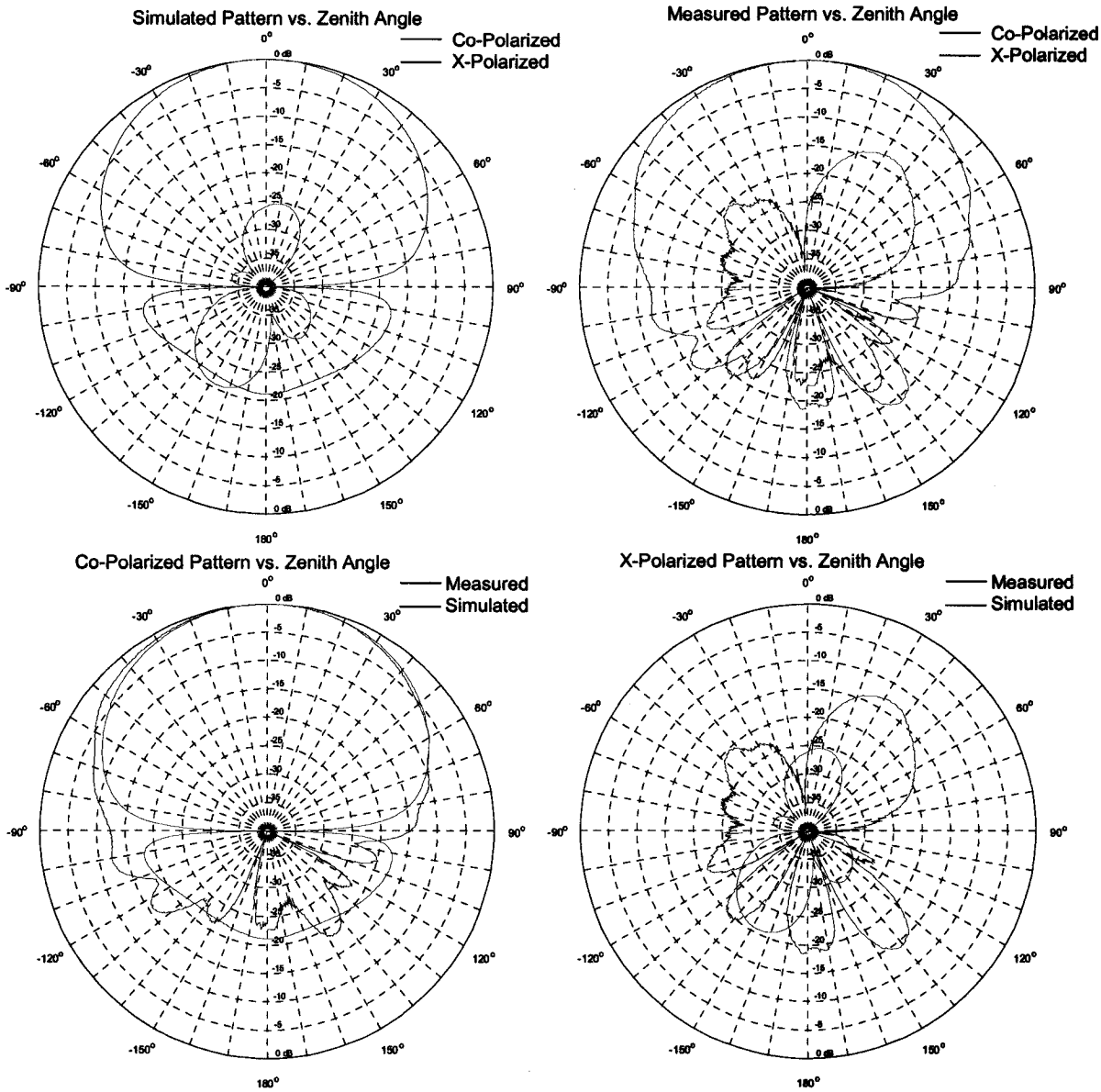

Figure 47 Normalized aperture-coupled polarization H-plane radiation patterns of the microstrip patch with three bends in the edge-coupled feed

The results for radiation patterns in Figure 47 are summarized in Table 10.

Table 10 Summary of aperture-coupled polarization H-plane radiation pattern parameters of the microstrip patch with three bends in the edge-coupled feed

	3dB Beamwidth	Max X-Pol Level ($\|\theta\| \leq 60°$)	Front to Back Ratio	Back Lobe ($\|\theta\| \geq 120°$)
Simulated	83°	-25.3dB @ 11°	21.2dB	-21.2dB @ 180°
Measured	89°	-13.0dB @ 34°	24.0dB	-15.8dB @ -123°

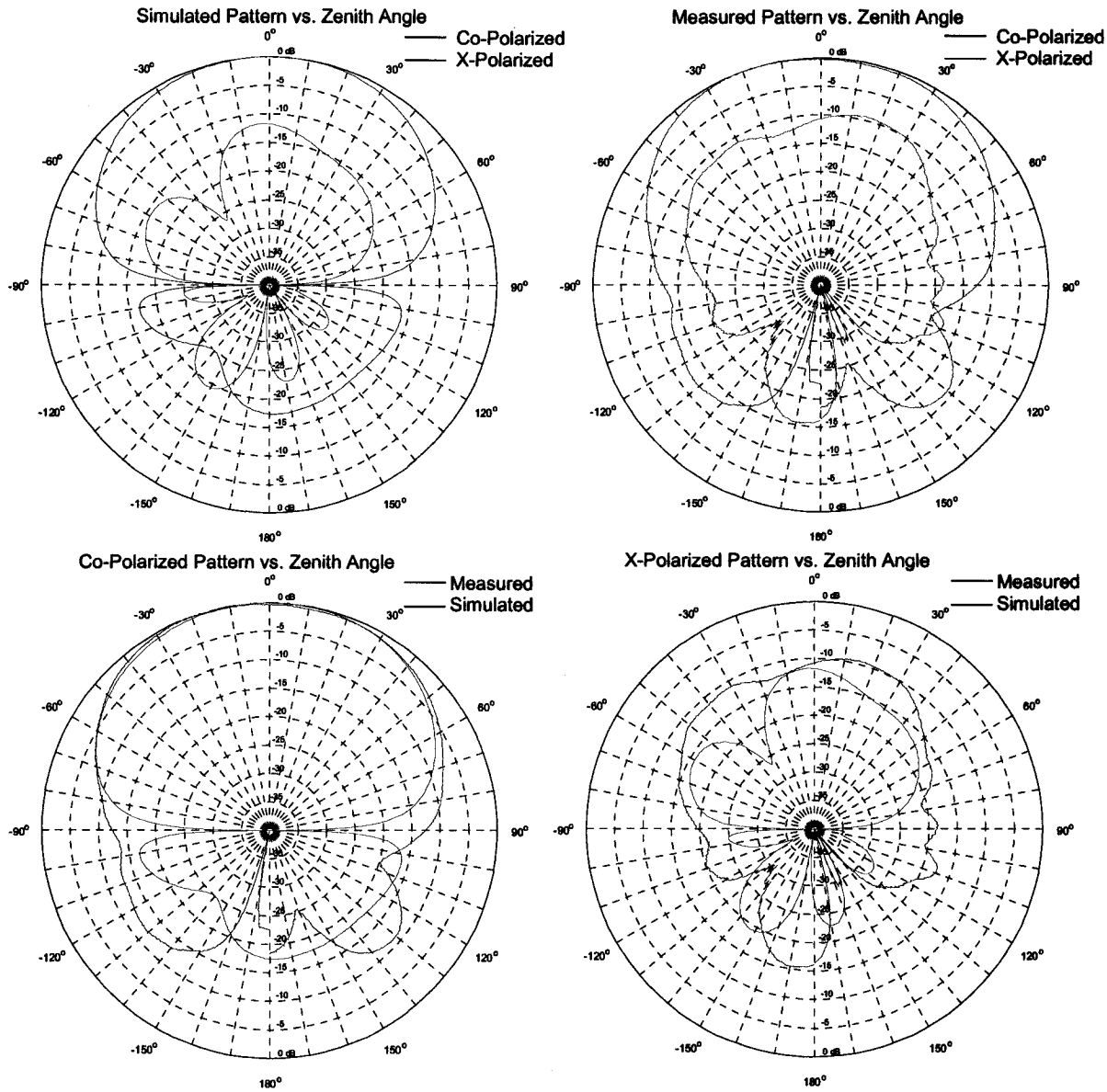

Figure 48 Normalized edge-coupled polarization E-plane radiation patterns of the microstrip patch with three bends in the edge-coupled

The results for radiation patterns in Figure 48 are summarized in Table 11.

Table 11 Summary of edge-coupled polarization E-plane radiation pattern parameters of the microstrip patch with three bends in the edge-coupled feed

	3dB Beamwidth	Max X-Pol Level ($\|\theta\| \leq 60°$)	Front to Back Ratio	Back Lobe ($\|\theta\| \geq 120°$)
Simulated	92°	-11.7dB @ 2°	17.4dB	-17.4 @ 180°
Measured	98°	-9.4dB @ -15°	20.0dB	-11.0 @ 131°

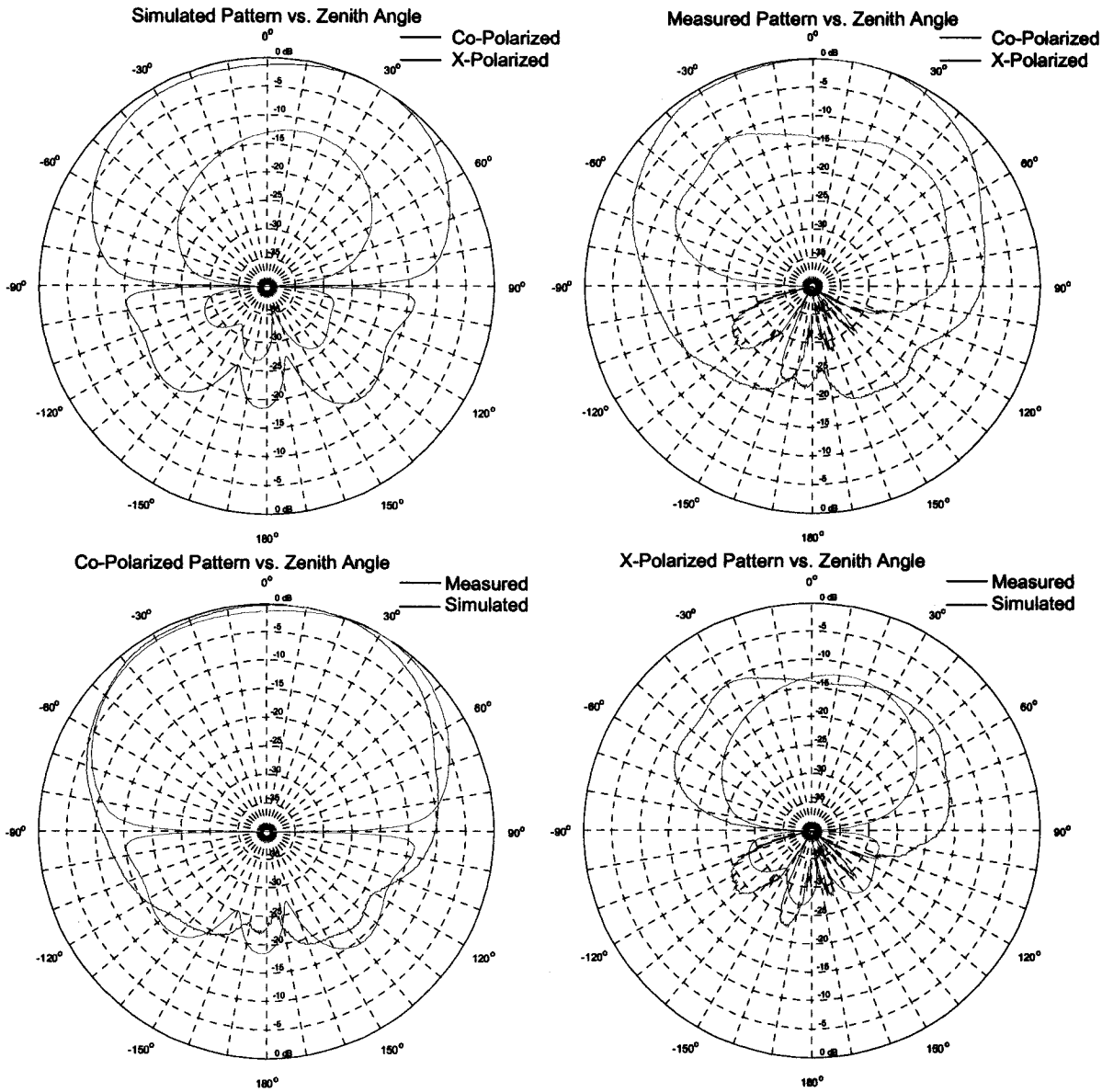

Figure 49 Normalized edge-coupled polarization H-plane radiation patterns of the microstrip patch with three bends in the edge-coupled feed

The results for radiation patterns in Figure 49 are summarized in Table 12.

Table 12 Summary of edge-coupled polarization H-plane radiation pattern parameters of the microstrip patch with three bends in the edge-coupled feed

	3dB Beamwidth	Max X-Pol Level ($\|\theta\| \leq 60°$)	Front to Back Ratio	Back Lobe ($\|\theta\| \geq 120°$)
Simulated	107°	-12.2dB @ 17°	18.7dB	-14.3dB @ 138°
Measured	97°	-10.4dB @ 30°	22.8dB	-17.2dB @ 135°

3.5 Feed Network Contribution to Increase in Cross-Polarization Levels

In order to assess the impact of the feed network on the cross-polarization levels, the performance of the radiating elements with probe-fed and edge-fed matching network shown in Figure 50a and Figure 50b will be examined.

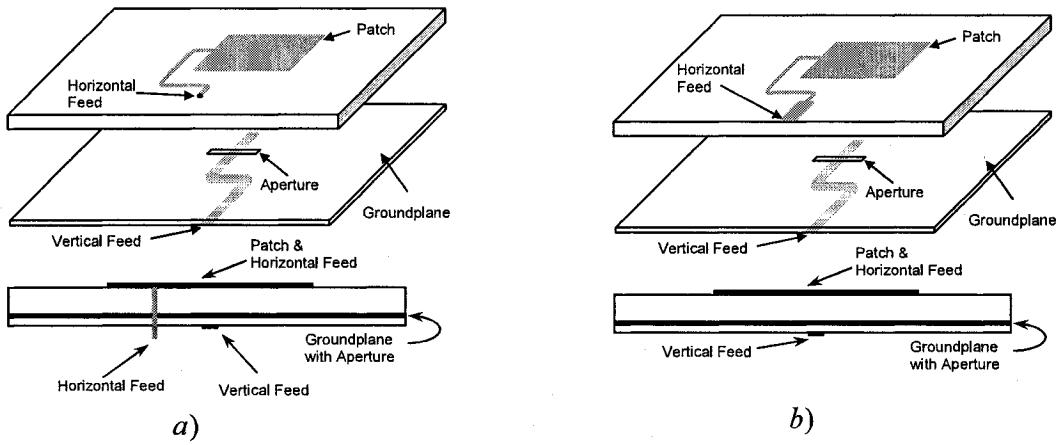

Figure 50 Dual-polarized microstrip patch with three bends in the edge-coupled feed, excited by a probe or a microstrip line

The geometry with the probe feed is expected to produce better cross-polarization levels due to the absence of the vertical 50Ω section of the feed network whose vertically polarized radiation directly affects the cross-polarization levels. The measured radiation patterns of the geometries in Figure 50 will be compared in order to assess the effects of the feed network on the cross-polarization levels. Only the cross-polarization of the edge-coupled portion of the dual-polarized patch is expected to improve because the only modification introduced is the one in the edge-coupled portion of the geometry.

The normalized measured E-plane radiation patterns of the radiators in Figure 50 for the polarization with aperture-coupling are shown in Figure 51. The normalized measured H-plane radiation patterns of the radiators in Figure 50 for the polarization with aperture-coupling are shown in Figure 52. The normalized measured E-plane radiation patterns of the radiators in Figure 50 for the polarization with edge-coupling are shown in Figure 53. The normalized measured H-plane radiation patterns of the radiators in Figure 50 for the polarization with edge-coupling are shown in Figure 54.

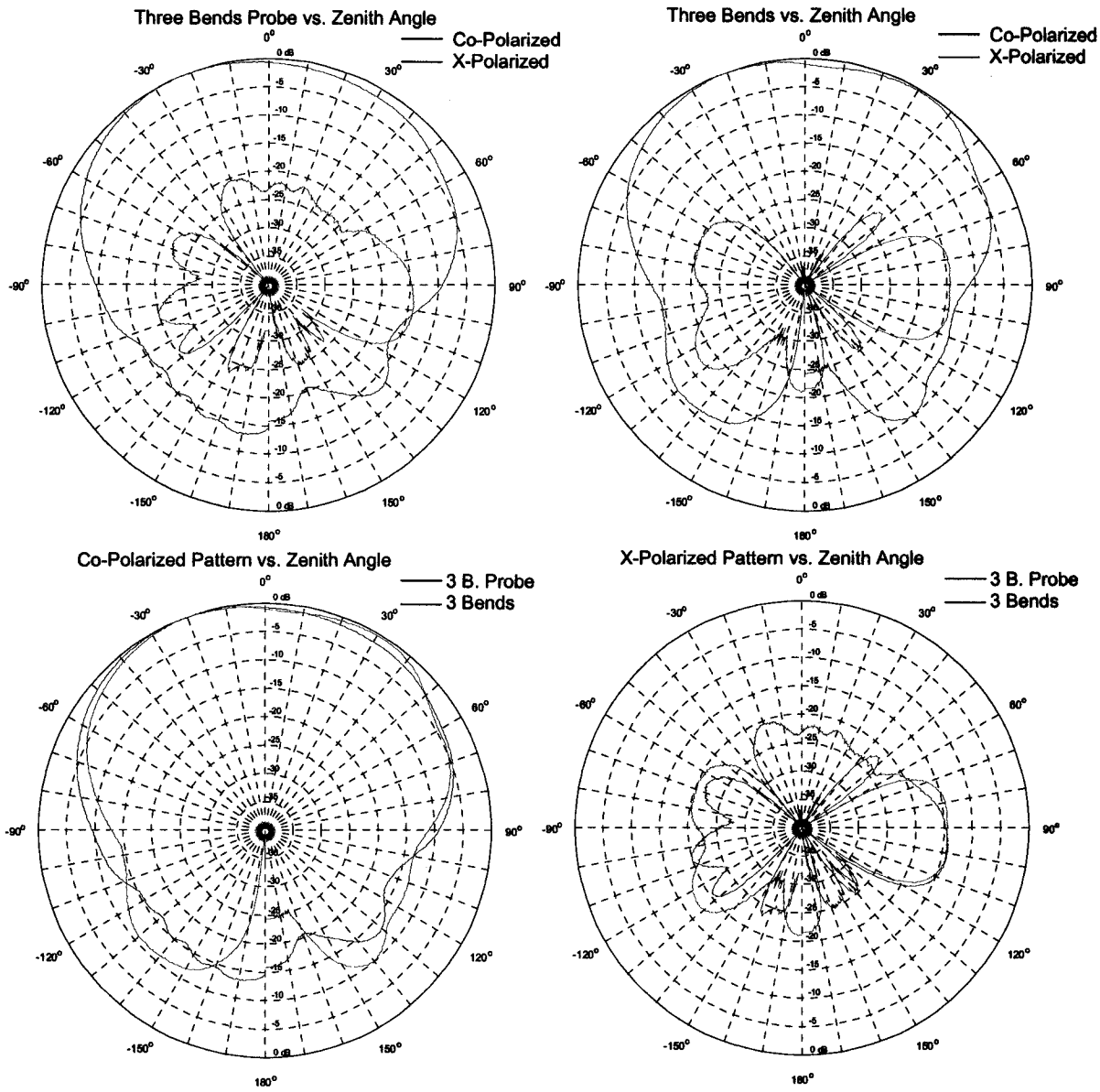

Figure 51 Normalized aperture-coupled polarization E-plane radiation pattern comparison for microstrip patch with three bends in the edge-coupled feed excited by a probe and a microstrip line

The results for radiation patterns in Figure 51 are summarized in Table 13.

Table 13 Summary of aperture-coupled polarization E-plane radiation pattern parameters of the microstrip patch with three bends in the edge-coupled feed excited by a probe and a microstrip line

	3dB Beamwidth	Max X-Pol Level ($\|\theta\| \leq 60°$)	Front to Back Ratio	Back Lobe ($\|\theta\| \geq 120°$)
3 bend	103°	-21.6dB @ 47°	24.4dB	-10.1dB @ 140°
3 bend probe	111°	-20.4dB @ -20°	15.0dB	-15.0dB @ 180°

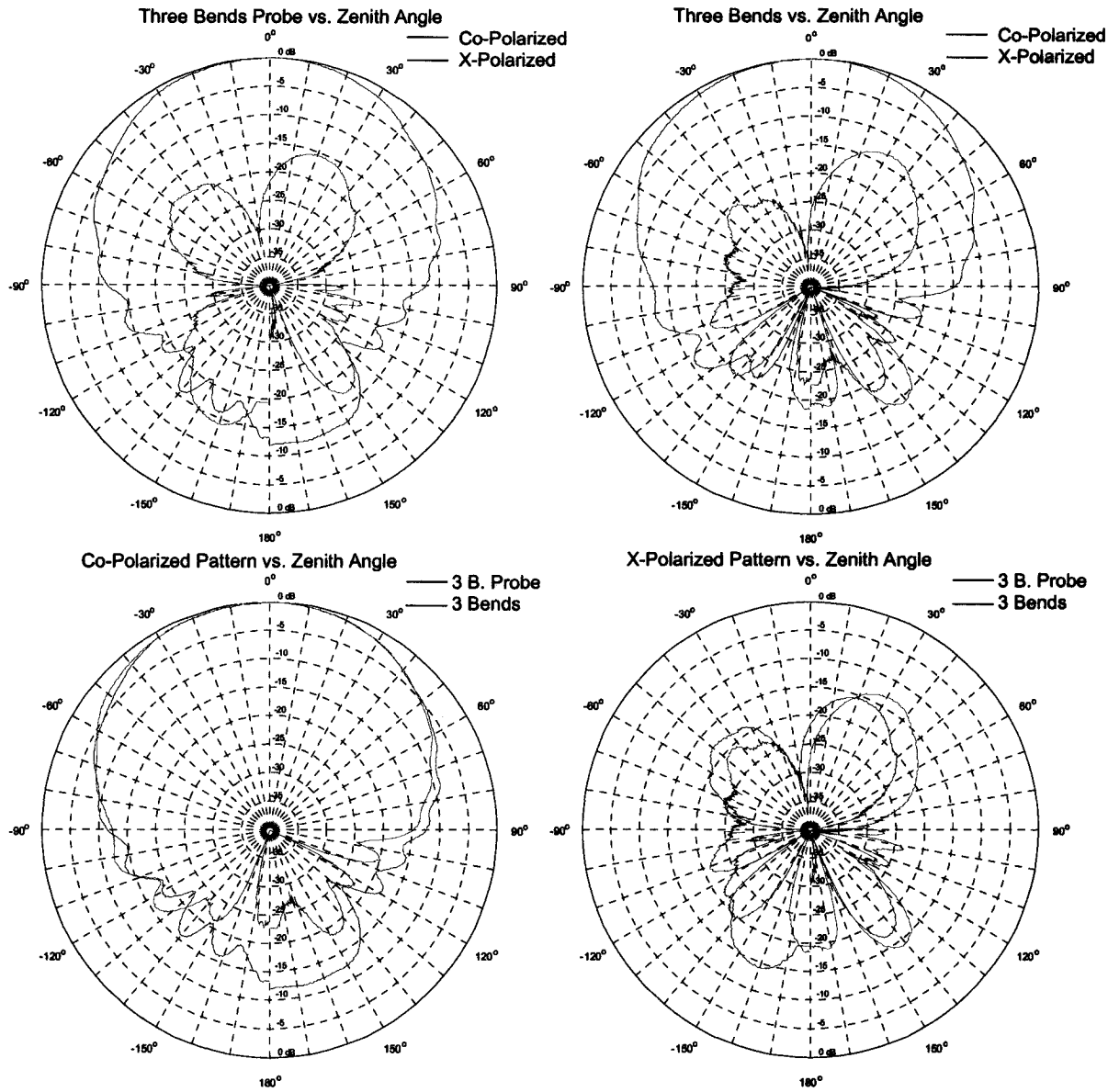

Figure 52 Normalized aperture-coupled polarization H-plane radiation pattern comparison for microstrip patch with three bends in the edge-coupled feed excited by a probe and a microstrip line

The results for radiation patterns in Figure 52 are summarized in Table 14.

Table 14 Summary of aperture-coupled polarization H-plane radiation pattern parameters of the microstrip patch with three bends in the edge-coupled feed excited by a probe and a microstrip line

	3dB Beamwidth	Max X-Pol Level ($\|\theta\| \leq 60°$)	Front to Back Ratio	Back Lobe ($\|\theta\| \geq 120°$)
3 bend	89°	-13.0dB @ 34°	-24dB	-15.8dB @ -123°
3 bend probe	81°	-15.4dB @ 22°	-13dB	-13.0dB @ 180°

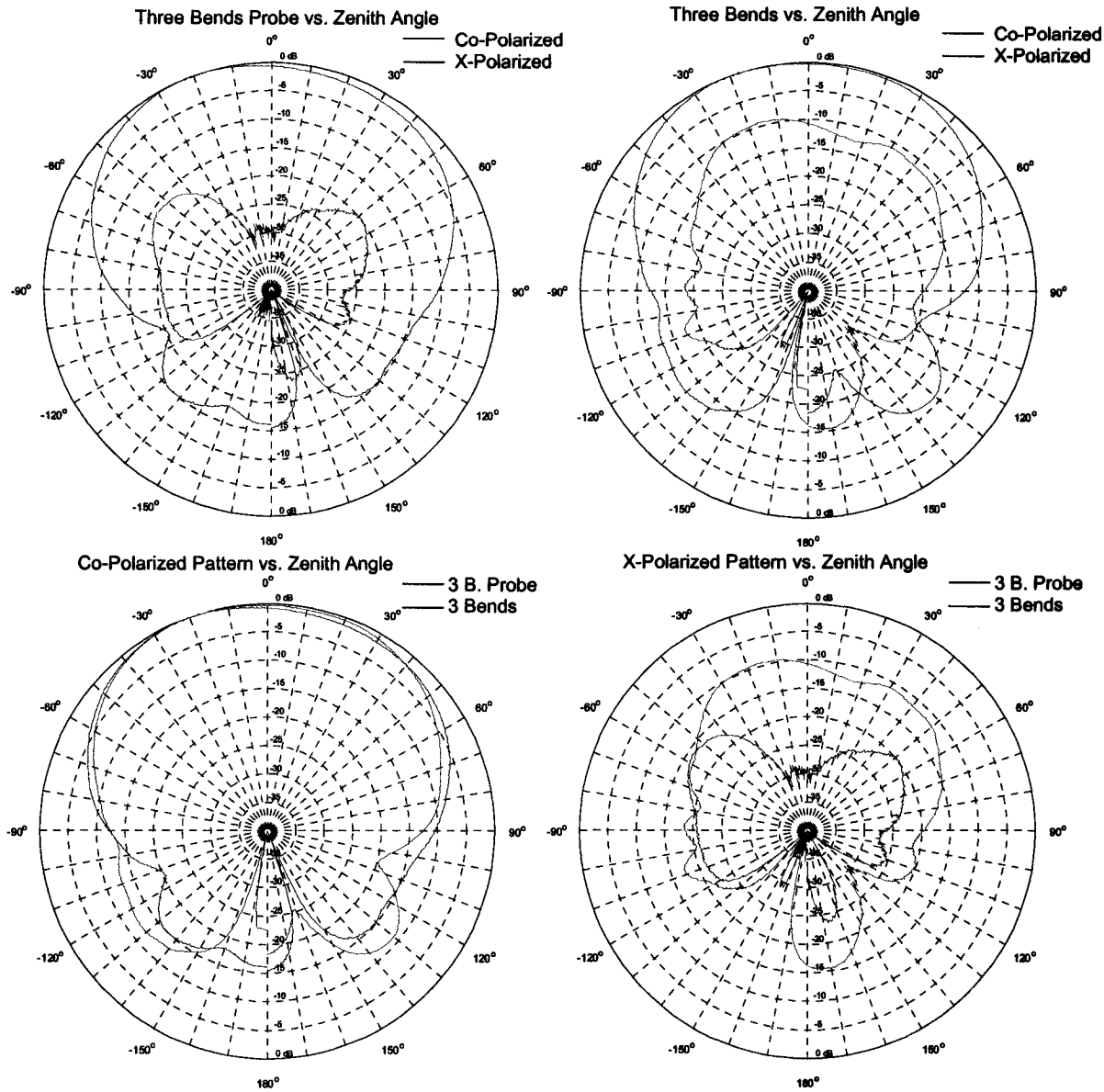

Figure 53 Normalized edge-coupled polarization E-plane radiation pattern comparison for microstrip patch with three bends in the edge-coupled feed excited by a probe and a microstrip line

The results for radiation patterns in Figure 53 are summarized in Table 15.

Table 15 Summary of edge-coupled polarization E-plane radiation pattern parameters of the microstrip patch with three bends in the edge-coupled feed excited by a probe and a microstrip line

	3dB Beamwidth	Max X-Pol Level ($\|\theta\| \leq 60°$)	Front to Back Ratio	Back Lobe ($\|\theta\| \geq 120°$)
3 bend	98°	-9.4dB @ -15°	20dB	-11.0dB @ 131°
3 bend probe	108°	-16.0dB @ 55°	16dB	-14.9dB @ -134

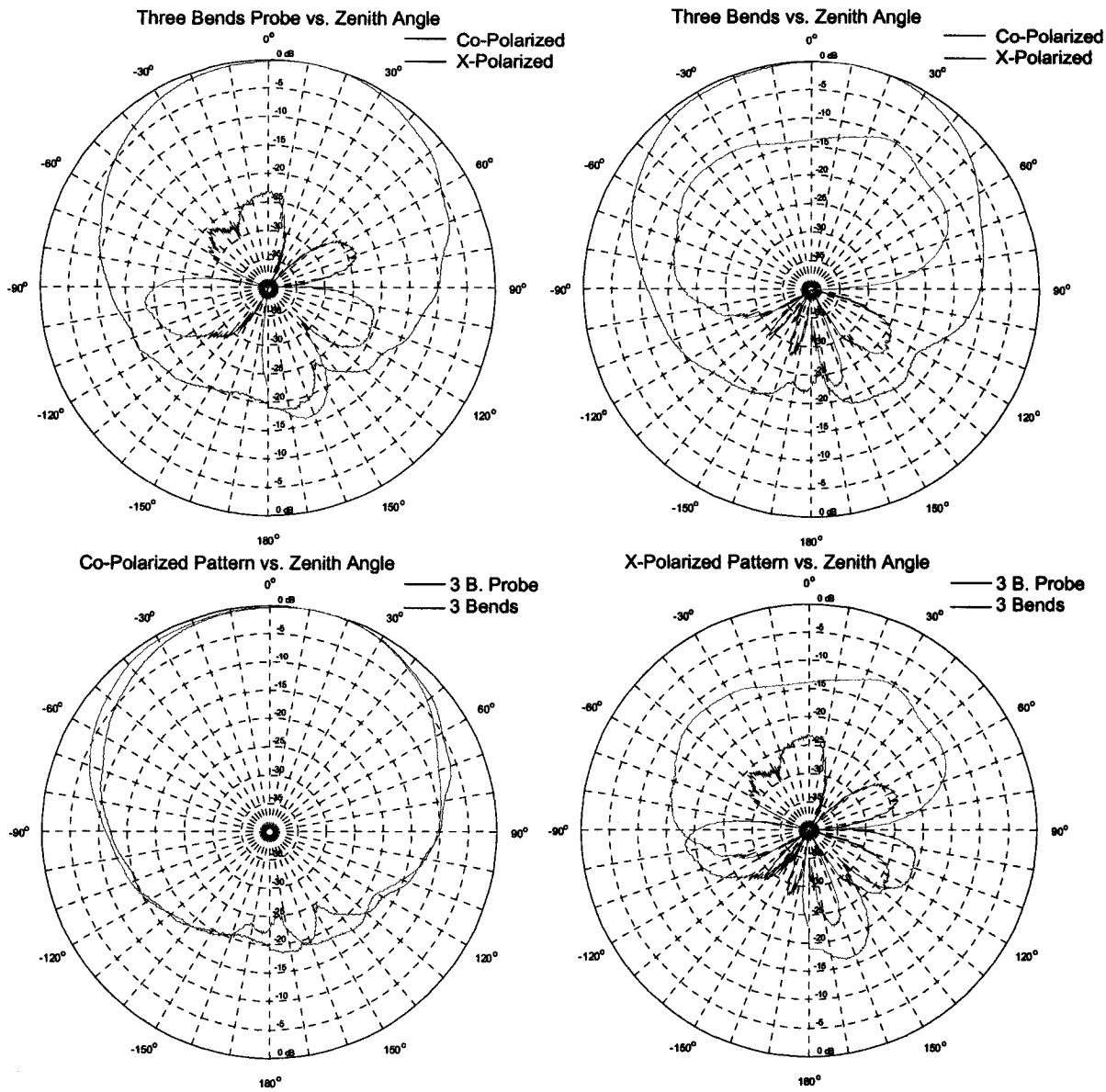

Figure 54 Normalized edge-coupled polarization H-plane radiation pattern comparison for microstrip patch with three bends in the edge-coupled feed excited by a probe and a microstrip line

The results for radiation patterns in Figure 54 are summarized in Table 16.

Table 16 Summary of edge-coupled polarization H-plane radiation pattern parameters of the microstrip patch with three bends in the edge-coupled feed excited by a probe and a microstrip line

	3dB Beamwidth	Max X-Pol Level ($\|\theta\| \leq 60°$)	Front to Back Ratio	Back Lobe ($\|\theta\| \geq 120°$)
3 bend	97°	-10.4dB @ 30°	22.8dB	-17.2dB @ 135°
3 bend probe	90°	-23.0dB @ 0°	19.5dB	-19.5dB @ 180°

3.6 Comparison of Isolation Performance of the Three Layouts

The port isolation performances of the layouts in Figure 29, Figure 35, and Figure 42 are shown in Figure 55.

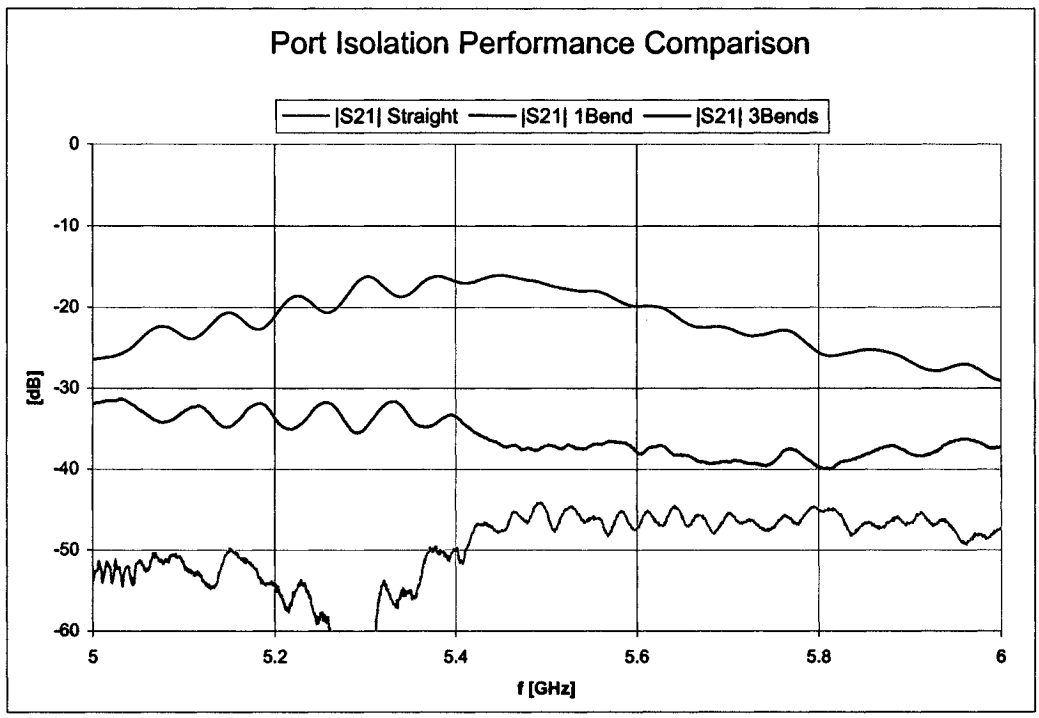

Figure 55 Port Isolation levels for three dual-polarized microstrip patch layouts

The best performance is exhibited by the element with straight feeds with the measured port isolation performance better than $44dB$ over the $1GHz$ span centered at $5.5GHz$. The worst performance was measured for the element with a single bend in the edge-coupled feed with port isolation performance better than $16dB$ over the $1GHz$ span centered at $5.5GHz$. The measured port isolation performance for the element with folded edge-coupled feed was found to be better than $36dB$ over the impedance bandwidth. The element with three bends in the edge-coupled feed has around $7dB$ lower port isolation performance than the element with the straight feed but it can be readily integrated into an array thus combining the good port isolation observed in the case of the element with the straight feed with a geometry that lends itself to integration into arrays.

3.7 Feed Network Physical Implementation and Modeling

The feed networks and matching networks were implemented using microstrip transmission lines. The parameters of the microstrip lines used in the feed network and matching network design are given in Table 17.

Table 17 Transmission line parameters

Top Layer Substrate RT/duroid 5880: ε_r=2.2, t=62mil, tanδ=0.0009			
Characteristic Impedance [Ω]	Line width [mm]	Guided Wavelength @ 5.5GHz [mm]	Effective Permittivity
50	5.08	39.7859	1.87696
70.7	2.912	40.3901	1.82123
100	1.48	41.0151	1.76615
141.42	0.612	41.6049	1.72059
143.66	0.582	41.5744	1.71895
200	0.186	41.9558	1.68784

Bottom Layer Substrate RT/duroid 5880: ε_r=2.2, t=20mil, tanδ=0.0009			
Characteristic Impedance [Ω]	Line width [mm]	Guided Wavelength @ 5.5GHz [mm]	Effective Permittivity
50	1.587	39.6938	1.88569
70.7	0.914	40.3226	1.82733
100	0.468	40.9505	1.77173

The transmission line with the characteristic impedance of 143.66Ω is used to implement quarter-wave transformers for radiating element matching purposes. In Chapter 4 the edge-coupled feed network is constructed using 100Ω transmission lines because of the prohibitive width of the 50Ω line (5.08mm) for given thickness and material properties of the dielectric substrate used. The aperture-coupled feed network is constructed using 50Ω transmission lines. The transmission lines with characteristic impedance of 141.42Ω, and 200Ω are used to implement the power splitters and 70.7Ω line is used to match the 100Ω feed network line to 50Ω port.

The IE3D models for geometries in this chapter have the following parameters:

- Groundplane: Finite groundplane
- Metallization material: Copper $\sigma = 5.8 \cdot 10^7\ S/m$
- Metallization thickness: $t = 36\mu m$
- Dielectric: RT Duroid 5880 $\varepsilon_r = 2.2$
- Dielectric Losses: $\tan\delta = 0.0009$
- Substrate thickness: Top layer $1.575mm$, Bottom layer $0.508mm$
- Substrate size: infinite

3.8 Concluding Remarks

Microstrip patches continue to be widely used as the radiating elements in planar array antennas, with the associated array feed networks comprised of microstrip transmission lines, power dividers and matching networks implemented in microstrip line as well. In order to obtain dual-polarization performance from such antenna arrays the individual microstrip patch radiators themselves have to be inherently dual-polarized and posses two distinct ports, one for each of the two polarizations. Most importantly, it must be possible to integrate such microstrip radiating elements into a corporate-fed planar array layout, where by "microstrip radiating element" we mean the patch plus its feed lines. In this chapter we have devised a dual-polarized microstrip radiating element with a feed line geometry that does not significantly degrade port isolation by its presence, and yet is compatible for use in the array environment. The element performance was studied through the comparison to that of an idealized element (which does not permit incorporation into an array) and a "simplistic" element which simply bends the feed lines of the idealized element in order to force it to fit into the planar array layout. Proper routing of the element feed lines in the vicinity of the patch was shown to be essential. This enabled us to establish that the new element provides excellent performance under the constraints of array compatibility. Comparison between the measured and simulated results was shown to be excellent. This allowed us to conclude that the effects of altering the feed line geometries observed during simulations were not due to the peculiarities of the computational electromagnetics method used but are indeed physically real. We were able to conjecture why the new array-compatible element provides a port isolation performance that is better than that of the poorly-performing simplistic element and only slightly worse than the idealized (but impractical) element, and then utilized the electromagnetic simulator in a rather novel way to verify this conjecture. In Chapter 4 we will examine the performance of the new dual-polarized microstrip radiating element in a planar array environment.

Chapter 4

The Array

4.1 Introductory Remarks

A single microstrip radiating element has a low gain and a broad beam. If a higher gain and narrower beam are required a number of elements can be arranged into an array. Depending on the spacing, and the number of elements it is possible to achieve higher gain, narrower beamwidth, beam-shaping, multi-beam patterns, and so on. Also, depending on the excitation amplitude and the phase of individual elements it is possible to suppress sidelobe levels and realize beam-squinting without physically moving the antenna. In planar array antennas comprised of microstrip patch elements, the feed network delivering power to the individual radiating elements within the array is usually implemented using microstrip lines. All power splitting, phase shifting, and impedance matching circuits necessary for beam-shaping, beam-squinting, and efficient operation of the antenna array are realized in microstrip and seamlessly integrated into the feed network. Integrating the dual-polarized microstrip elements into an array is challenging because we have to cope with two feed networks instead of one. There is a need to address additional issues like cross-coupling between the radiating elements and the feed network lines, and a need to route certain sections of the feed network transmission lines so to minimize the detrimental cross-coupling effects on the port isolation levels. The beam-shaping techniques such as: excitation amplitude taper and phase progression need to be examined in detail regarding their effects on port isolation levels and a special attention given to the implementation of these features.

In section 4.2 we will discuss the effects that the element spacing, element grouping and certain sections of the feed network have on the port isolation. The simulated and measured results are presented in section 4.3. The benefits of using two different feed mechanisms are discussed in section 4.4. Section 4.5 deals with the implementation of the excitation amplitude taper and phase progression, their effects on the port isolation and how suitable application of the excitation amplitude taper can improve the port isolation

performance of the array. In section 4.6 an attempt is made to utilize simulated values of the magnetic field to obtain the feed network geometry design clues. Section 4.7 concludes the chapter.

In Chapter 3 we devised a dual-polarized microstrip radiating element that has good port isolation performance and lends itself to easy integration into an array environment. We can now embark on the task of integrating this element into the array environment in order to produce an array antenna that will preserve the isolation performance inherent to the individual element yet provide higher directivity, and lower cross-polarization levels than those of a single radiating element. We will consider the effects of the spatial arrangement of the radiating elements within the array structure and a specific approach to the grouping of the elements in order to keep the isolation performance at a satisfactory level. Then we will discuss how to deal with the portions of the feed network which have no mirrored counterparts with respect to the axis of symmetry of the feed network residing on the same substrate level with radiating elements. The simulated and measured results for 2x4, and 4x4 element arrays will be presented, and we will see that measured results corroborate the simulated results, which will enable us to use simulated results with increased confidence in future research efforts.

4.2 Integration of Individual Elements into an Array

4.2.1 The Effects of Element Positioning on Port Isolation

The simulated port isolation for two microstrip patch radiators is shown in Figure 56. The plot is obtained by horizontally sliding one of the elements past the other one at vertical separations of: 30mm, 35mm, 40mm, 45mm, and 50mm. Port isolation is better than 40dB when the top element is slightly to the left of the vertical alignment of the elements. As the top element is moved from this optimum position the port isolation quickly deteriorates and reaches the lowest value, which varies depending on the vertical separation of the elements, and then slowly gets better with increase in horizontal separation. The horizontal separation at which the port isolation gets better than 40dB is much larger than freespace wavelength thus relying on horizontal spacing as means of

maintaining high port isolation is out of the question for antenna arrays due to appearance of grating lobes in radiation patterns with elements being spaced that far.

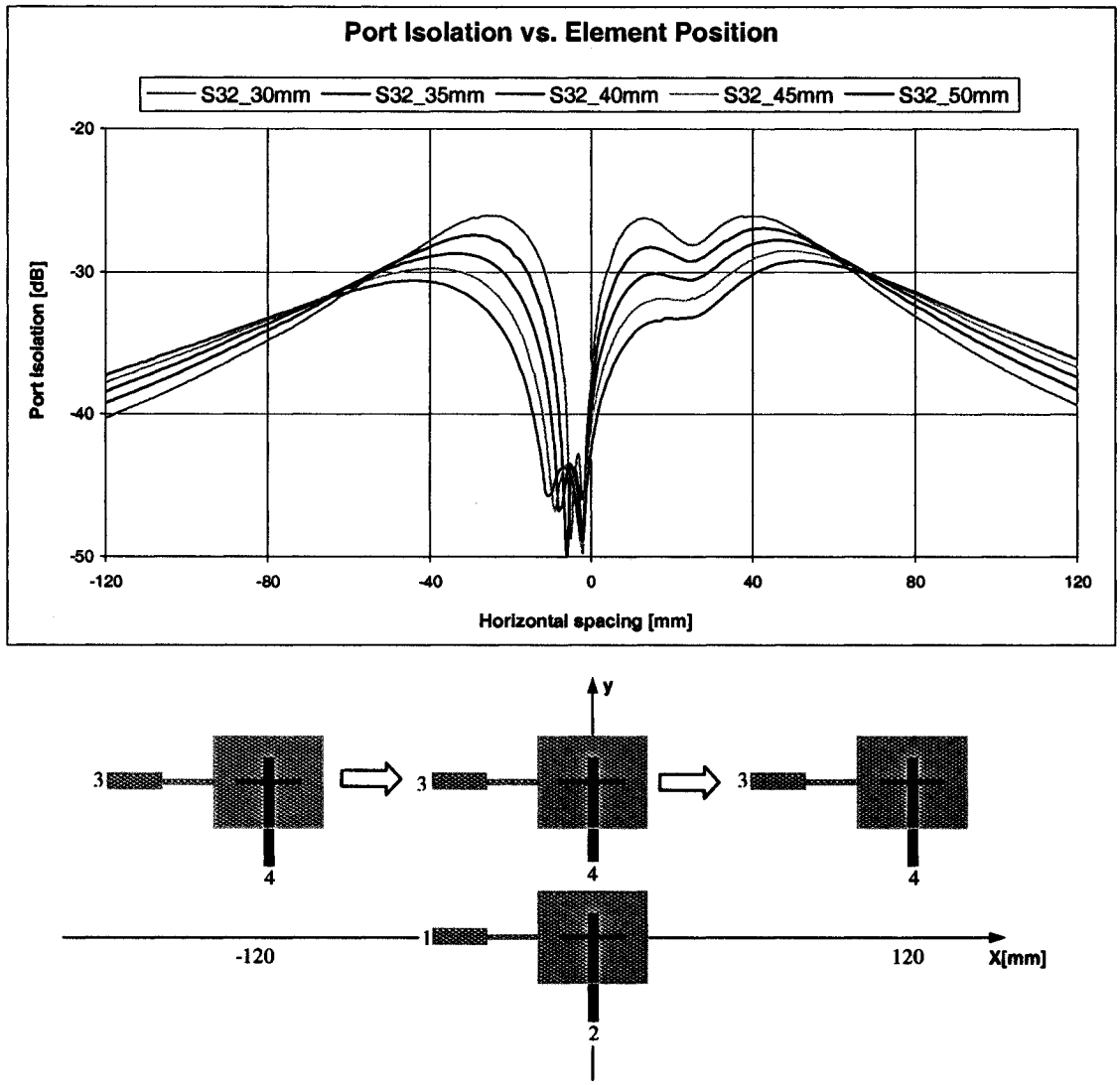

Figure 56 Effects of element positioning on the port isolation

4.2.2 Element Grouping

The port isolation of a single radiating element discussed in Chapter 3 is not sufficiently high (36dB measured) to ensure targeted port isolation of 40dB for the array. However, by grouping radiating elements vertically into columns we can achieve an additional cancellation of the cross-coupling contributions from the individual radiating elements and improve overall port isolation to meet the 40dB port isolation requirement. To observe how this cancellation occurs the elements are arranged as shown in Figure 57, ports 3 through 10 are excited by voltage sources with equal phase and magnitude and ports 1

and 2 are terminated in matched impedances. The scattering parameters corresponding to the ports whose positions are mirrored with respect to the horizontal axis of the geometry shown in Figure 57 are equal in magnitude and are 180° out of phase and therefore the cross-coupling contributions originating from these ports cancel out. The absolute values of sums of the scattering parameters corresponding to mirrored ports are shown in Figure 57. As long as the symmetry of the geometry is maintained and as long as the port excitation is uniform in phase, the cancellation of the cross-coupling contributions from the individual elements is ensured. Only vertical transmission lines of the feed network are susceptible to the cross-coupling and as long as each vertical section is paired with its version mirrored with respect to the horizontal axis of symmetry the cancellation of the cross-coupling will be very good as we can see from Figure 57.

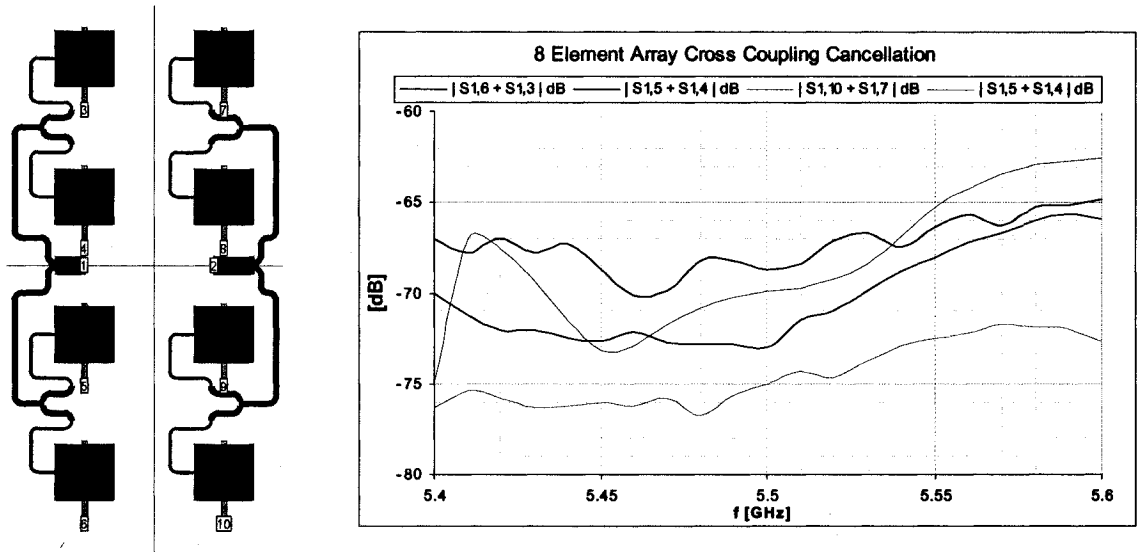

Figure 57 Cross coupling cancellation within the 2x4 element array

However, when we want to use the 2x4 array as a building block for larger arrays we will have to introduce vertical sections of the feed network that will have no mirrored counterparts and, therefore, their contributions to cross-coupling will not be cancelled.

4.2.3 Treatment of Non-Mirrored Vertical Feed Lines

When the edge-coupled feed network excites the radiating elements to produce horizontally (vertically) polarized radiation, then vertical (horizontal) non-mirrored feed network lines have detrimental effects on the port isolation. In our case the edge-coupled feed network excites the radiating elements to produce horizontally polarized radiation. The meandering is introduced into sections of the feed network without mirrored counterparts with respect to the horizontal axis of the layout in order to minimize their impact on the port isolation. The meandering of the non-mirrored feed network sections will improve port isolation performance by up to 20dB compared to the case of non-meandered non-mirrored feed network sections. The meandering consists of three "U"-bends symmetrically arranged around the center of the non-mirrored portion of the feed network. The depth and width of the "U"-bends are optimized to maximize the port isolation performance of the array.

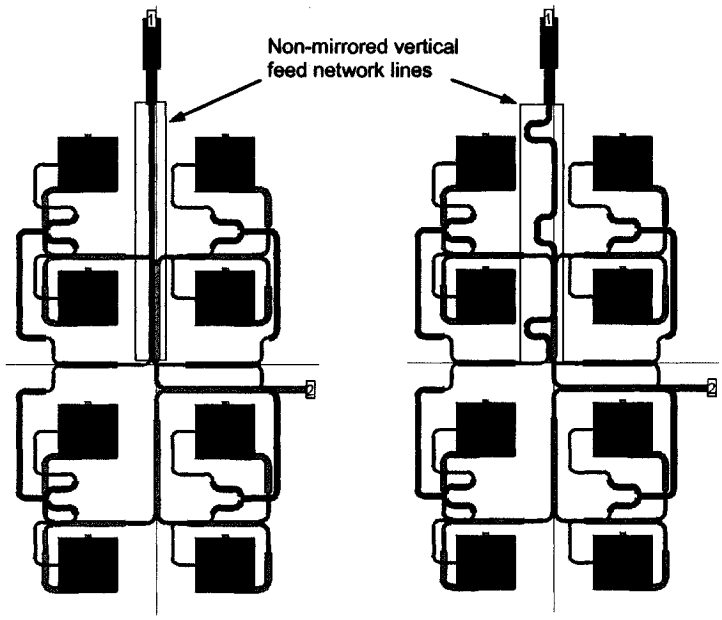

Figure 58 Layout of the 2x4 array with a straight non-mirrored feed network section and with a meandered non-mirrored feed network section

The horizontal sections of the "U"-bends provide the phase delay necessary for the cancellation of the cross-coupling contributions from other parts of the antenna geometry picked up along the line in a manner similar to that described in section 3.4.

The comparison of simulated S-parameters of two array geometries in Figure 58 is shown in Figure 59.

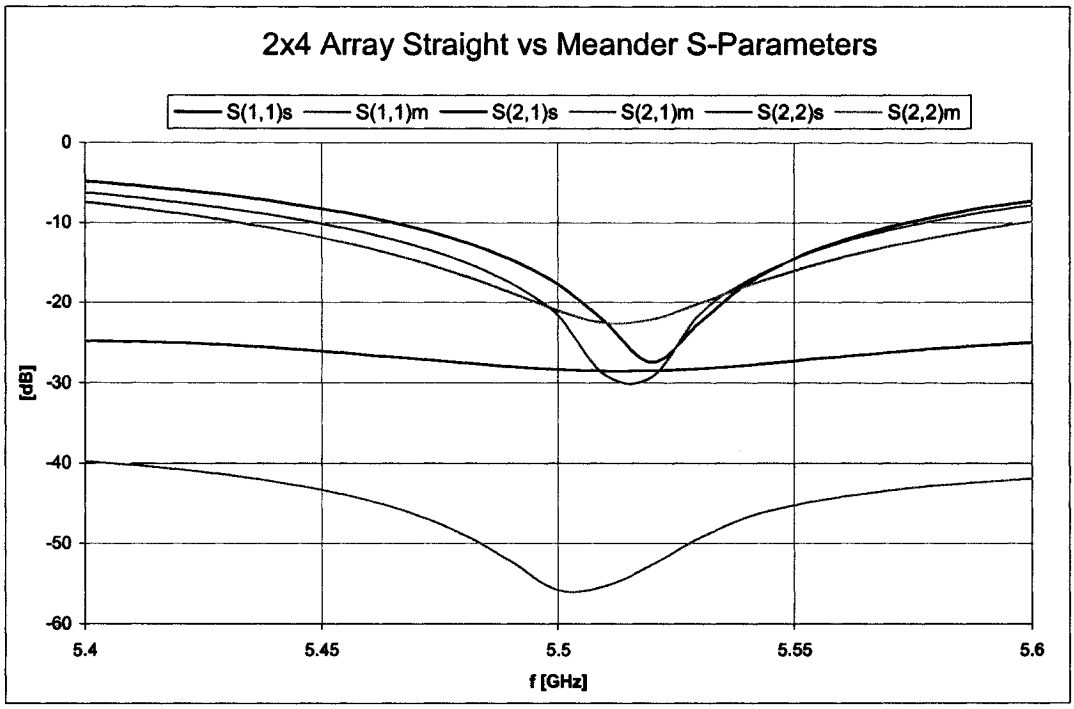

Figure 59 Straight vs. meandered non-mirrored line layout results

The array geometry with meandered non-mirrored section of the feed network exhibits port isolation level better than 40dB over the 200MHz span centered at 5.5GHz. The return loss for the aperture-coupled polarization is identical for both geometries as expected since these particular feed networks are identical. The return loss for the edge-coupled polarization has slightly improved after the meandering was implemented resulting, along with significant improvement in port isolation performance, in an increase in impedance bandwidth of the array for the edge-coupled polarization.

4.3 Simulated and Measured Results

The 2x4 array design was fine-tuned and optimized in IE3D electromagnetic simulator in order to attain better than 40dB port isolation performance over the impedance bandwidth with satisfactory return loss for both polarizations. Once the desired results were achieved we used the 2x4 array as a building block to construct a 4x4 array. The layouts obtained from the IE3D electromagnetic simulator were used in the fabrication of the arrays

and in the following sections the simulated and measured results obtained in the process are presented.

4.3.1 Gain Measurement and Calculation

To measure gain of the two arrays we had two methods at our disposal: Gain Transfer Method, and Absolute Gain Method [24].

The gain transfer method requires an antenna gain standard. The procedure for obtaining the gain of the antenna under test (AUT) consists of comparing the received power from the gain standard antenna and the received power from the antenna under test while everything else in the link is unchanged. The gain of the antenna under test in *dBi* is then given by $G_{AUT} = G_{ST} + P_{AUT} - P_{ST}$.

The absolute gain method requires three antennas and no prior knowledge of the gain of the antennas used. This method requires three measurements of the received power with antennas placed at fixed known distance from each other. To calculate the gain of all three antennas the Friis' link equation is used to form the system of three equations with three unknowns from which all three gains can be calculated. The procedure will need to be performed for both aperture-coupled polarization and edge-coupled polarization.

We decided to use the absolute gain method to measure the gain of the 2x4 and 4x4 arrays. As the third antenna in the measurement we used American Electronic Laboratories horn antenna model H1498 with frequency range of 2-18GHz and maximum on-axis gain of 11dBi [25, [26]. The measurement setup block diagram is shown in Figure 60.

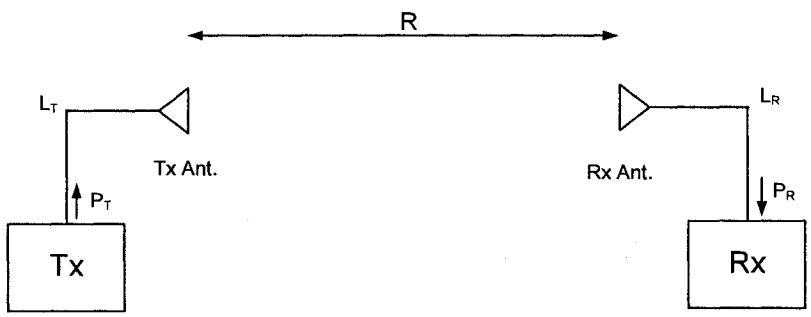

Figure 60 Antenna gain measurement setup

From the block diagram in Figure 60 we can write the Friis' link equation 4.3.1-1.

$$P_R = P_T - L_T + G_T + 20\log\left(\frac{\lambda}{4\pi R}\right) + G_R - L_R$$
$$P_R - P_T + L_T - 20\log\left(\frac{\lambda}{4\pi R}\right) + L_R = G_T + G_R \qquad 4.3.1\text{-}1$$

The terms in 4.3.1-1 are designated as follows:

P_T – Transmitted Power

P_R – Received Power

L_T – Insertion loss of the coaxial cable connecting the Transmitter and the Tx Antenna

L_R – Insertion loss of the coaxial cable connecting the Rx Antenna and the Receiver

R – Separation between Tx and Rx Antenna

G_T – Gain of the transmit Antenna

G_R – Gain of the receive Antenna

In order to determine the gain of the pyramidal horn antenna, 2x4 and 4x4 microstrip antenna arrays we will use the measured results in Table 18 in Friis' equation and calculate the gain of all three antennas.

The system of the three equations 4.3.1-1 can be represented in a matrix form 4.3.1-2.

$$\begin{bmatrix} P_{R1} - P_{T1} + L_T - 20\log\left(\frac{\lambda}{4\pi R}\right) + L_R \\ P_{R2} - P_{T2} + L_T - 20\log\left(\frac{\lambda}{4\pi R}\right) + L_R \\ P_{R3} - P_{T3} + L_T - 20\log\left(\frac{\lambda}{4\pi R}\right) + L_R \end{bmatrix} = \begin{bmatrix} 1 & 1 & 0 \\ 1 & 0 & 1 \\ 0 & 1 & 1 \end{bmatrix} \cdot \begin{bmatrix} G_1 \\ G_2 \\ G_3 \end{bmatrix} \qquad 4.3.1\text{-}2$$

The gains of individual antennas are designated as follows:

G_1 – Gain of the Horn Antenna

G_{2A} – Aperture-coupled polarization gain of the 4x4 Array

G_{3A} – Aperture-coupled polarization gain of the 2x4 Array

G_{2E} – Edge-coupled polarization gain of the 4x4 Array

G_{3E} – Edge-coupled polarization gain of the 2x4 Array

The measurement results obtained are summarized in Table 18.

Table 18 Summary of the gain measurements for both polarizations

Tx Antenna		Rx Antenna		Tx Power [dBm]	Rx Power [dBm]	Tx Coax Loss [dB]	Rx Coax Loss [dB]	Free Space Loss [dB]	Polarization efficiency	G_T+G_R [dB_i]
Antenna type	Coupling Type	Antenna type	Coupling Type							
Pyramidal Horn	-	2x4 microstrip Array	Edge	21.73	-28.22	6.69	8.42	60.059	1	25.219
Pyramidal Horn	-	2x4 Microstrip Array	Aperture	21.74	-26.5	6.69	8.42	60.059	1	26.929
Pyramidal Horn	-	4x4 Microstrip Array	Edge	21.72	-24.48	6.69	8.42	60.059	1	28.969
Pyramidal Horn	-	4x4 Microstrip Array	Aperture	21.77	-23.92	6.69	8.42	60.059	1	29.479
4x4 Microstrip Array	Edge	2x4 Microstrip Array	Edge	21.79	-20.73	6.69	8.42	60.059	1	32.649
4x4 Microstrip Array	Aperture	2x4 Microstrip Array	Aperture	21.8	-17.6	6.69	8.42	60.059	1	35.769

Since we are dealing with dual-polarized antennas we will have to obtain gain for each of the polarizations. Measured results for the polarization with aperture coupling are shown in Table 19

Table 19 Summary of the gain measurements for the polarization with aperture coupling

Tx Antenna		Rx Antenna		Tx Power [dBm]	Rx Power [dBm]	Tx Coax Loss [dB]	Rx Coax Loss [dB]	Free Space Loss [dB]	Polarization efficiency	G_T+G_R [dB]
Antenna type	Coupling Type	Antenna type	Coupling Type							
Pyramidal Horn	-	2x4 Microstrip Array	Aperture	21.74	-26.5	6.69	8.42	60.059	1	26.929
Pyramidal Horn	-	4x4 Microstrip Array	Aperture	21.77	-23.92	6.69	8.42	60.059	1	29.479
4x4 Microstrip Array	Aperture	2x4 Microstrip Array	Aperture	21.8	-17.6	6.69	8.42	60.059	1	35.769

The matrix form of the system of three Friis' equations with three unknown gains is given in 4.3.1-3.

$$\begin{bmatrix} 1 & 1 & 0 \\ 1 & 0 & 1 \\ 0 & 1 & 1 \end{bmatrix} \cdot \begin{bmatrix} G_1 \\ G_{2A} \\ G_{3A} \end{bmatrix} = \begin{bmatrix} P_{R1} - P_{T1} + L_T - 20\log\left(\frac{\lambda}{4\pi R}\right) + L_R \\ P_{R2} - P_{T2} + L_T - 20\log\left(\frac{\lambda}{4\pi R}\right) + L_R \\ P_{R3} - P_{T3} + L_T - 20\log\left(\frac{\lambda}{4\pi R}\right) + L_R \end{bmatrix} = \begin{bmatrix} 29.479dB_i \\ 26.929dB_i \\ 35.769dB_i \end{bmatrix} \quad 4.3.1\text{-}3$$

The gains of individual antennas are calculated in 4.3.1-4.

$$\begin{bmatrix} G_1 \\ G_{2A} \\ G_{3A} \end{bmatrix} = \begin{bmatrix} 1 & 1 & 0 \\ 1 & 0 & 1 \\ 0 & 1 & 1 \end{bmatrix}^{-1} \cdot \begin{bmatrix} 29.479dB_i \\ 26.929dB_i \\ 35.769dB_i \end{bmatrix} = \frac{1}{2}\begin{bmatrix} 1 & 1 & -1 \\ 1 & -1 & 1 \\ -1 & 1 & 1 \end{bmatrix} \cdot \begin{bmatrix} 29.479dB_i \\ 26.929dB_i \\ 35.769dB_i \end{bmatrix} = \begin{bmatrix} 10.3195dB_i \\ 19.1595dB_i \\ 16.6095dB_i \end{bmatrix} \quad 4.3.1\text{-}4$$

Measured results for the polarization with edge coupling are shown in Table 20

Table 20 Summary of the gain measurements for the polarization with edge coupling

Tx Antenna		Rx Antenna		Tx Power [dBm]	Rx Power [dBm]	Tx Coax Loss [dB]	Rx Coax Loss [dB]	Free Space Loss [dB]	Polarization efficiency	G_T+G_R [dB]
Antenna type	Coupling Type	Antenna type	Coupling Type							
Pyramidal Horn	-	2x4 Microstrip Array	Edge	21.73	-28.22	6.69	8.42	60.059	1	25.219
Pyramidal Horn	-	4x4 Microstrip Array	Edge	21.72	-24.48	6.69	8.42	60.059	1	28.969
4x4 Microstrip Array	Edge	2x4 Microstrip Array	Edge	21.79	-20.73	6.69	8.42	60.059	1	32.649

The matrix form of the system of three Friis' equations with three unknown gains is given in 4.3.1-5.

$$\begin{bmatrix} 1 & 1 & 0 \\ 1 & 0 & 1 \\ 0 & 1 & 1 \end{bmatrix} \cdot \begin{bmatrix} G_1 \\ G_{2E} \\ G_{3E} \end{bmatrix} = \begin{bmatrix} P_{R1} - P_{T1} + L_T - 20\log\left(\frac{\lambda}{4\pi R}\right) + L_R \\ P_{R2} - P_{T2} + L_T - 20\log\left(\frac{\lambda}{4\pi R}\right) + L_R \\ P_{R3} - P_{T3} + L_T - 20\log\left(\frac{\lambda}{4\pi R}\right) + L_R \end{bmatrix} = \begin{bmatrix} 28.969dB_i \\ 25.219dB_i \\ 32.649dB_i \end{bmatrix} \quad \text{4.3.1-5}$$

The gains of individual antennas are calculated in 4.3.1-6.

$$\begin{bmatrix} G_1 \\ G_{2E} \\ G_{3E} \end{bmatrix} = \begin{bmatrix} 1 & 1 & 0 \\ 1 & 0 & 1 \\ 0 & 1 & 1 \end{bmatrix}^{-1} \cdot \begin{bmatrix} 28.969dB_i \\ 25.219dB_i \\ 32.649dB_i \end{bmatrix} = \frac{1}{2}\begin{bmatrix} 1 & 1 & -1 \\ 1 & -1 & 1 \\ -1 & 1 & 1 \end{bmatrix} \cdot \begin{bmatrix} 28.969dB_i \\ 25.219dB_i \\ 32.649dB_i \end{bmatrix} = \begin{bmatrix} 10.7695dB_i \\ 18.1995dB_i \\ 14.4495dB_i \end{bmatrix} \quad \text{4.3.1-6}$$

The gain performance of the three antennas for polarizations with both edge and aperture coupling is summarized in Table 21.

Table 21 Summary of the measured and simulated gain performance of the three antennas used

Antenna type	Gain [dBi]			
	Edge-Coupling		Aperture-Coupling	
	Measured	Predicted	Measured	Predicted
Pyramidal Horn	10.8	11.0*	10.3	11.0*
2x4 Microstrip Array	14.4	13.8888**	16.6	15.6856**
4x4 Microstrip Array	18.2	17.3808**	19.2	18.7788**

*Manufacturer specification

**IE3D simulation

4.3.2 Simulated and Measured Results for the 2x4 Array

The physical layout of the 2x4 microstrip array is shown in Figure 61.

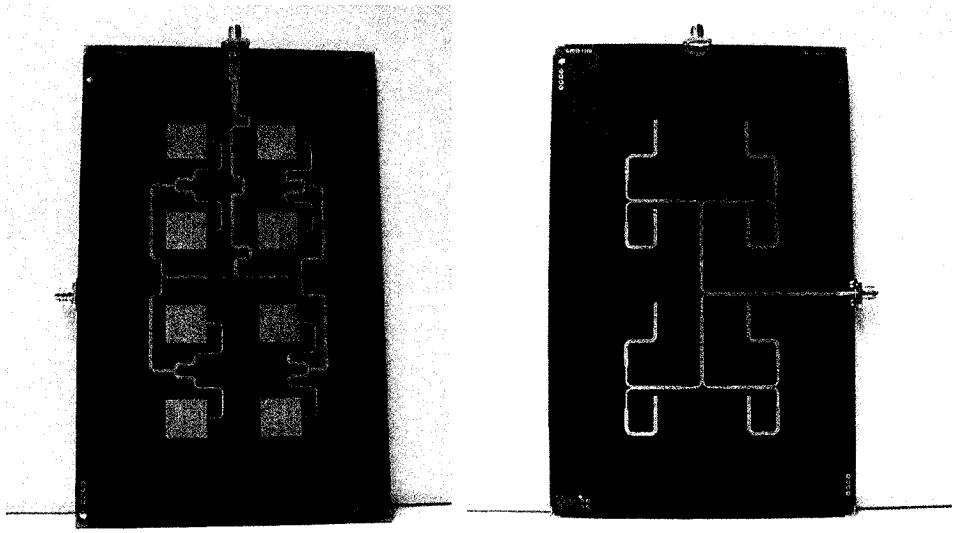

Figure 61 Physical implementation of the 2x4 dual-polarized microstrip patch array

The simulated and measured S-parameters of the 2x4 microstrip array in Figure 61 are shown in Figure 62. The array resonates at $5.495GHz$ and has an impedance bandwidth of 2.7% calculated using $B_{\%} = \frac{B_{VSWR\leq 2}}{f_{res}} 100\%$. The measured port isolation performance is better than $50dB$ at resonance. Once the proper precautions in the design of the feed network are taken the port isolation performance of the array is better than that of the single microstrip radiating element (Figure 42) used to construct the array. Both edge-coupled and aperture-coupled feed network of the array are designed to provide uniform amplitude excitation and zero phase progression, the arrangement that yields broadside beam, and maximum aperture efficiency.

The simulated and measured E-plane radiation patterns of the array in Figure 61 for the polarization with aperture-coupling are shown in Figure 63. The simulated and measured H-plane radiation patterns of the array in Figure 61 for the polarization with aperture-coupling are shown in Figure 64. The simulated and measured E-plane radiation patterns of the array in Figure 61 for the polarization with edge-coupling are shown in Figure 65. The simulated and measured H-plane radiation patterns of the array in Figure 61 for the polarization with edge-coupling are shown in Figure 66.

The simulated and measured S-parameters of the 2x4 microstrip array in Figure 61 are shown in Figure 62.

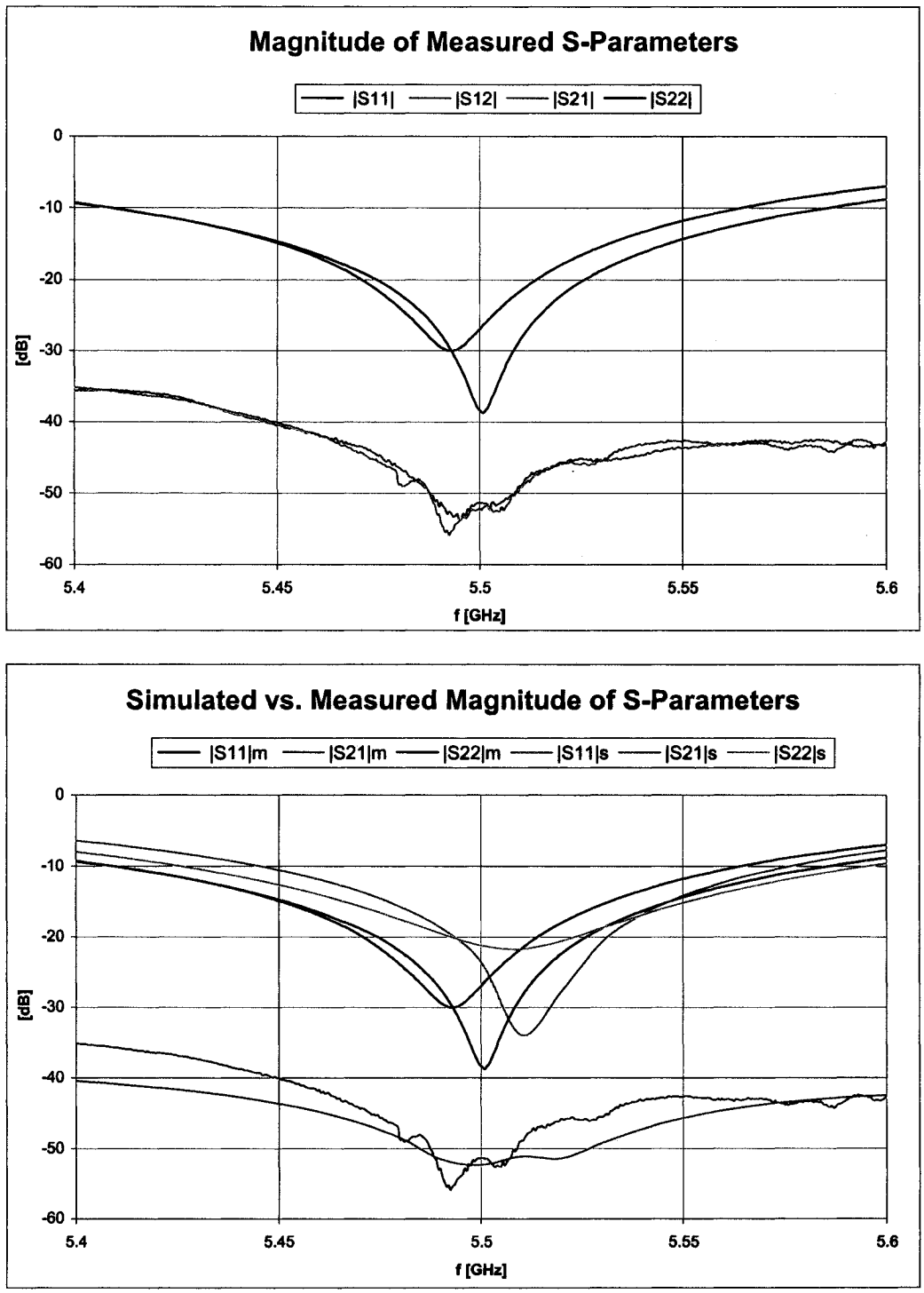

Figure 62 S-parameters for 2x4 dual-polarized microstrip array

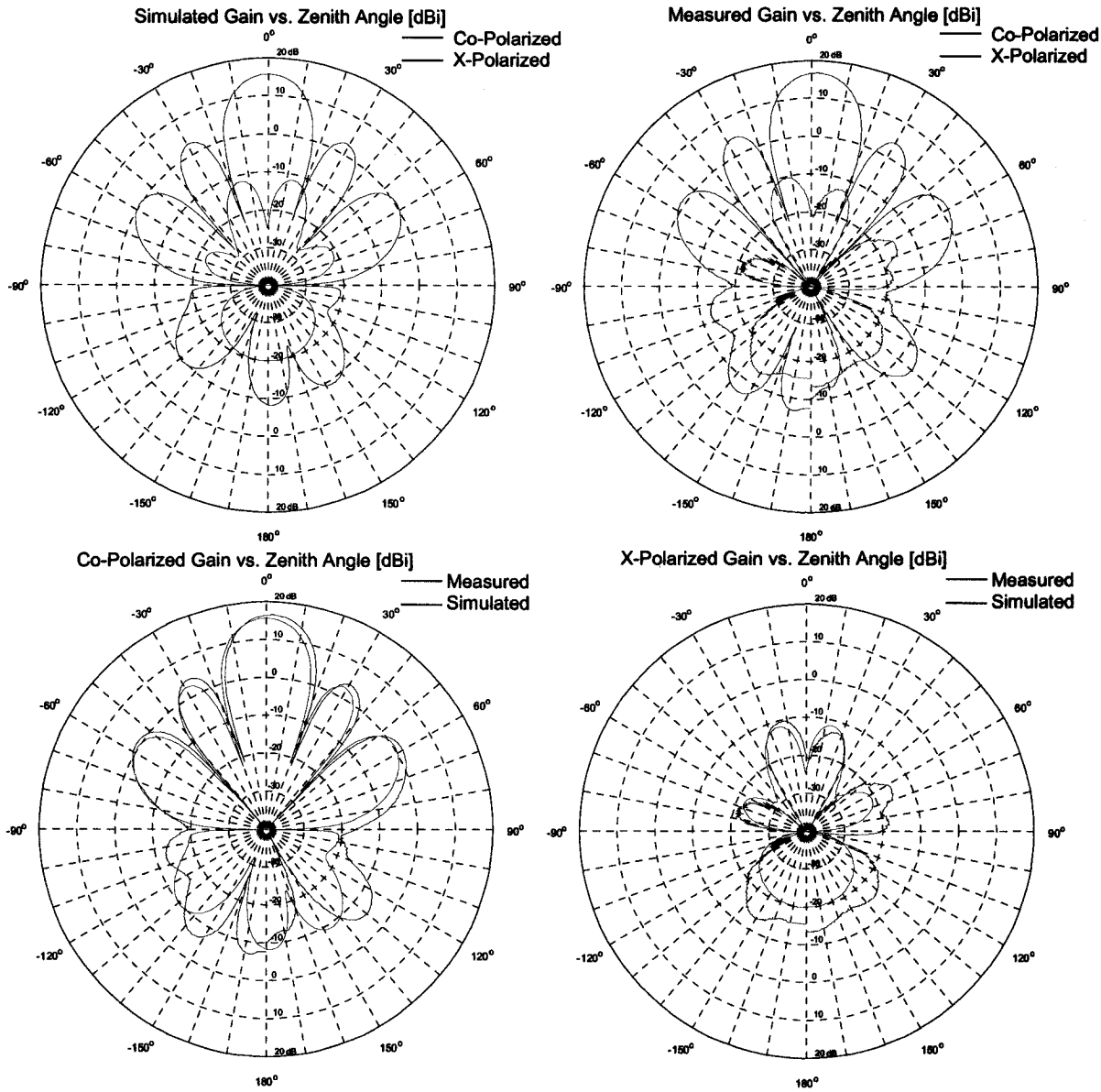

Figure 63 Measured and simulated aperture-coupled polarization E-plane radiation patterns of the 2x4 dual-polarized microstrip patch array

The results for radiation patterns in Figure 63 are summarized in Table 22.

Table 22 Summary of aperture-coupled polarization E-plane radiation pattern parameters of the 2x4 dual-polarized microstrip patch array

	3dB Beamwidth	Max X-Pol Level ($\|\theta\| \leq 60°$)	Front to Back Ratio	Back Lobe ($\|\theta\| \geq 120°$)
Simulated	18°	-28.1dB @ 14°	24.1dB	-24.1dB @ 180°
Measured	18°	-26.9dB @ 12°	25.0dB	-23.4dB @ -173°

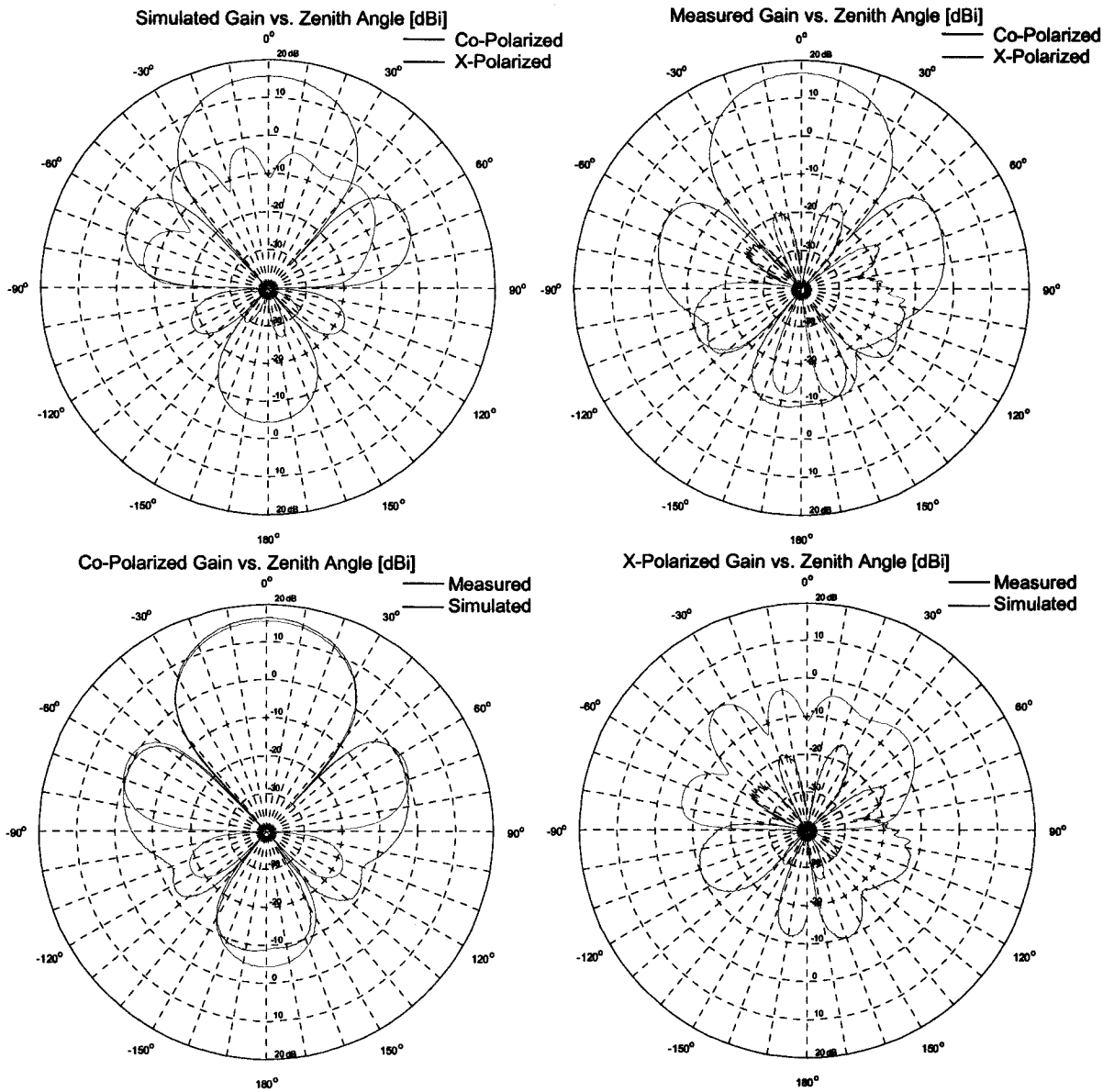

Figure 64 Measured and simulated aperture-coupled polarization H-plane radiation patterns of the 2x4 dual-polarized microstrip patch array

The results for radiation patterns in Figure 64 are summarized in Table 23.

Table 23 Summary of aperture-coupled polarization H-plane radiation pattern parameters of the 2x4 dual-polarized microstrip patch array

	3dB Beamwidth	Max X-Pol Level ($\|\theta\| \leq 60°$)	Front to Back Ratio	Back Lobe ($\|\theta\| \geq 120°$)
Simulated	36°	-15.8dB @ -35°	21.1dB	-21.1dB @ 180°
Measured	35°	-32.4dB @ 25°	25.5dB	-25.5dB @ 180°

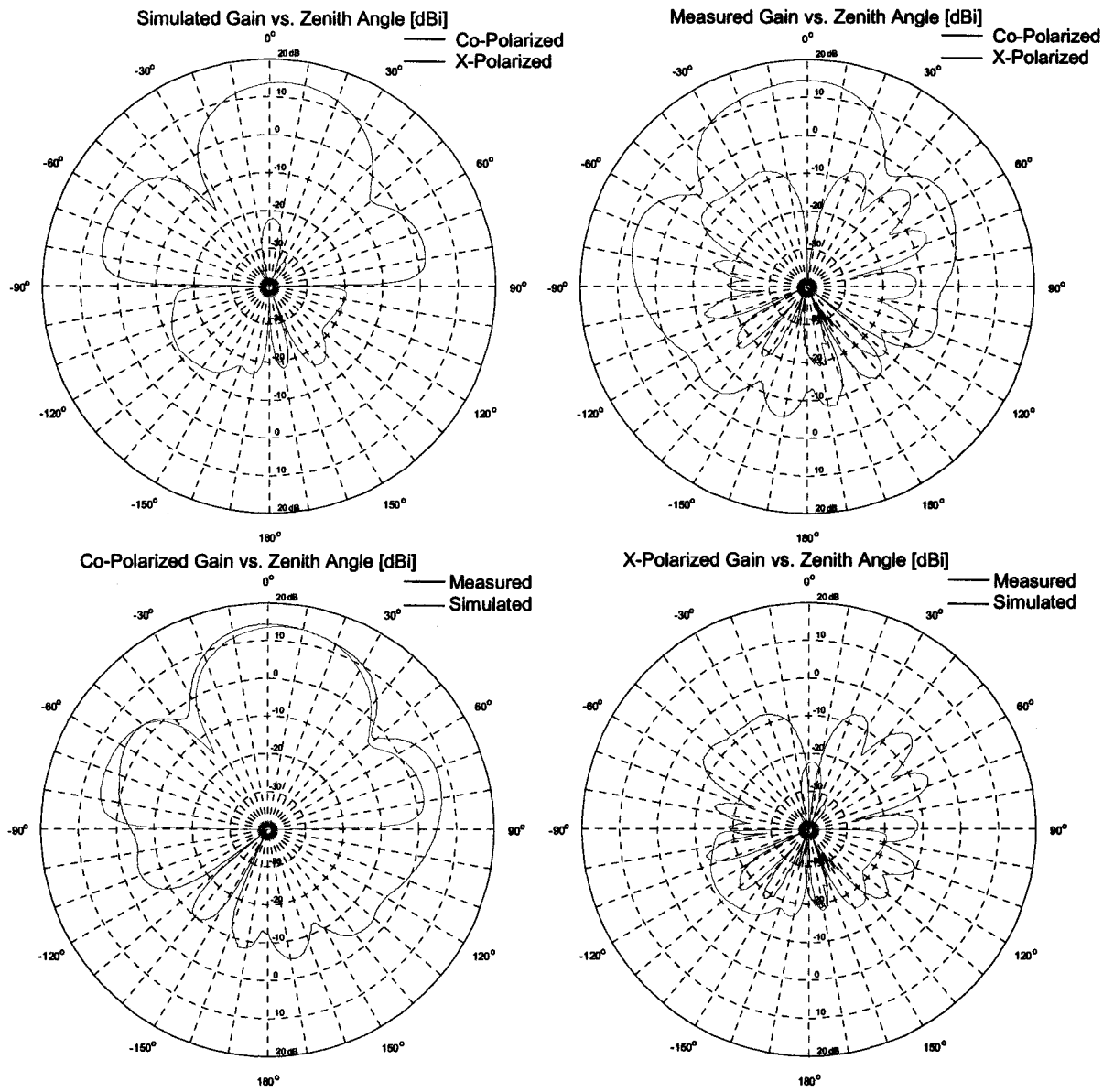

Figure 65 Measured and simulated edge-coupled polarization E-plane radiation patterns of the 2x4 dual-polarized microstrip patch array

The results for radiation patterns in Figure 65 are summarized in Table 24.

Table 24 Summary of edge-coupled polarization E-plane radiation pattern parameters of the 2x4 dual-polarized microstrip patch array

	3dB Beamwidth	Max X-Pol Level ($\|\theta\| \leq 60°$)	Front to Back Ratio	Back Lobe ($\|\theta\| \geq 120°$)
Simulated	38°	-36.1dB @ 4°	53.8dB	-53.8dB @ 180°
Measured	41°	-18.0dB @ 46°	26.5dB	-19.6dB @ -168°

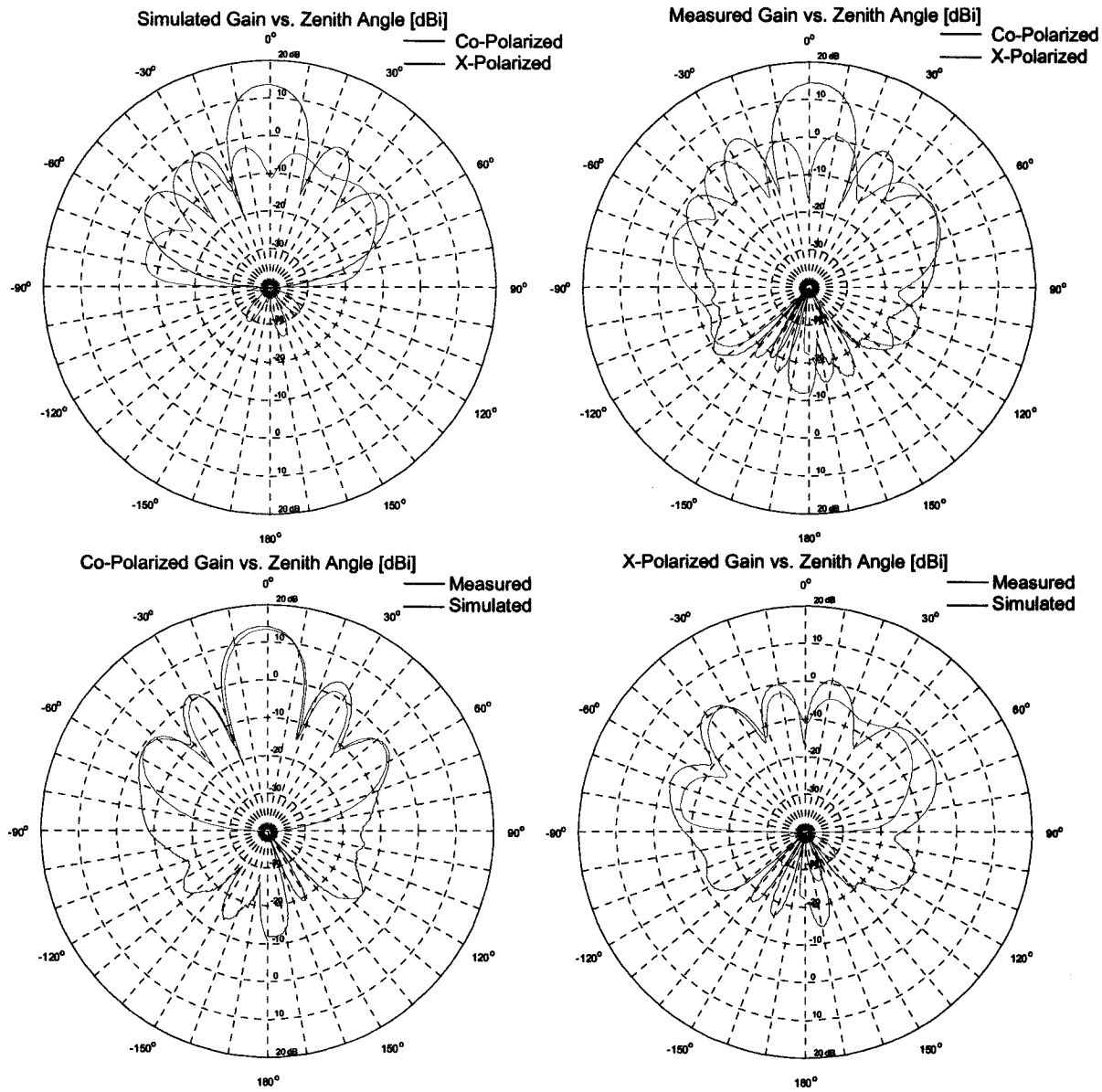

Figure 66 Measured and simulated edge-coupled polarization H-plane radiation patterns of the 2x4 dual-polarized microstrip patch array

The results for radiation patterns in Figure 66 are summarized in Table 25.

Table 25 Summary of edge-coupled polarization H-plane radiation pattern parameters of the 2x4 dual-polarized microstrip patch array

	3dB Beamwidth	Max X-Pol Level ($\|\theta\| \leq 60°$)	Front to Back Ratio	Back Lobe ($\|\theta\| \geq 120°$)
Simulated	17°	-14.0dB @ -35°	63.5dB	-53.0dB @ 138°
Measured	17°	-13.5dB @ -10°	26dB	-24.3dB @ -125°

4.3.3 Simulated and Measured Results for 4x4 Array

The physical layout of the 4x4 microstrip array is shown in Figure 67.

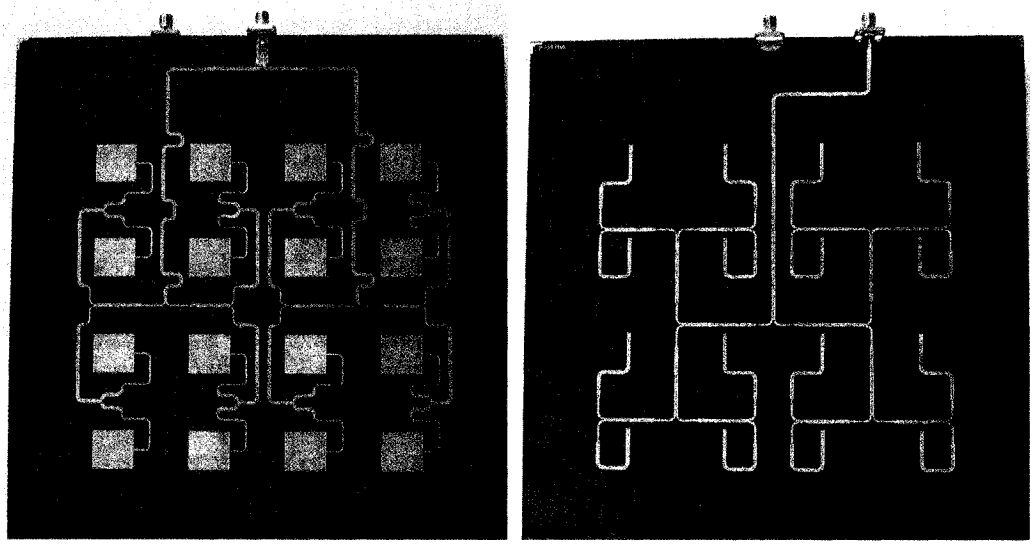

Figure 67 Physical implementation of the 4x4 dual-polarized microstrip patch array

The simulated and measured S-parameters of the 4x4 microstrip array in Figure 67 are shown in Figure 68. The array resonates at $5.505GHz$ and has an impedance bandwidth of 2.3% calculated using $B_{\%} = \frac{B_{VSWR\leq 2}}{f_{res}} 100\%$. The measured port isolation is $50dB$ at resonance. From the measured scattering parameters shown in Figure 68 we can see that the port isolation performance is retained after we constructed a 4x4 array using two 2x4 sub-arrays, therefore it is possible to build larger arrays with high port isolation from smaller sub-arrays as long as the sub-array suppresses the cross coupling between its radiating elements and exhibits good port isolation. In this particular implementation of the 4x4 array the excitation amplitude is uniform there is no phase progression.

The simulated and measured E-plane radiation patterns of the array in Figure 67 for the polarization with aperture-coupling are shown in Figure 69. The simulated and measured H-plane radiation patterns of the array in Figure 67 for the polarization with aperture-coupling are shown in Figure 70. The simulated and measured E-plane radiation patterns of the array in Figure 67 for the polarization with edge-coupling are shown in Figure 71. The simulated and measured H-plane radiation patterns of the array in Figure 67 for the polarization with edge-coupling are shown in Figure 72.

The simulated and measured S-parameters of the 4x4 microstrip array in Figure 67 are shown in Figure 68.

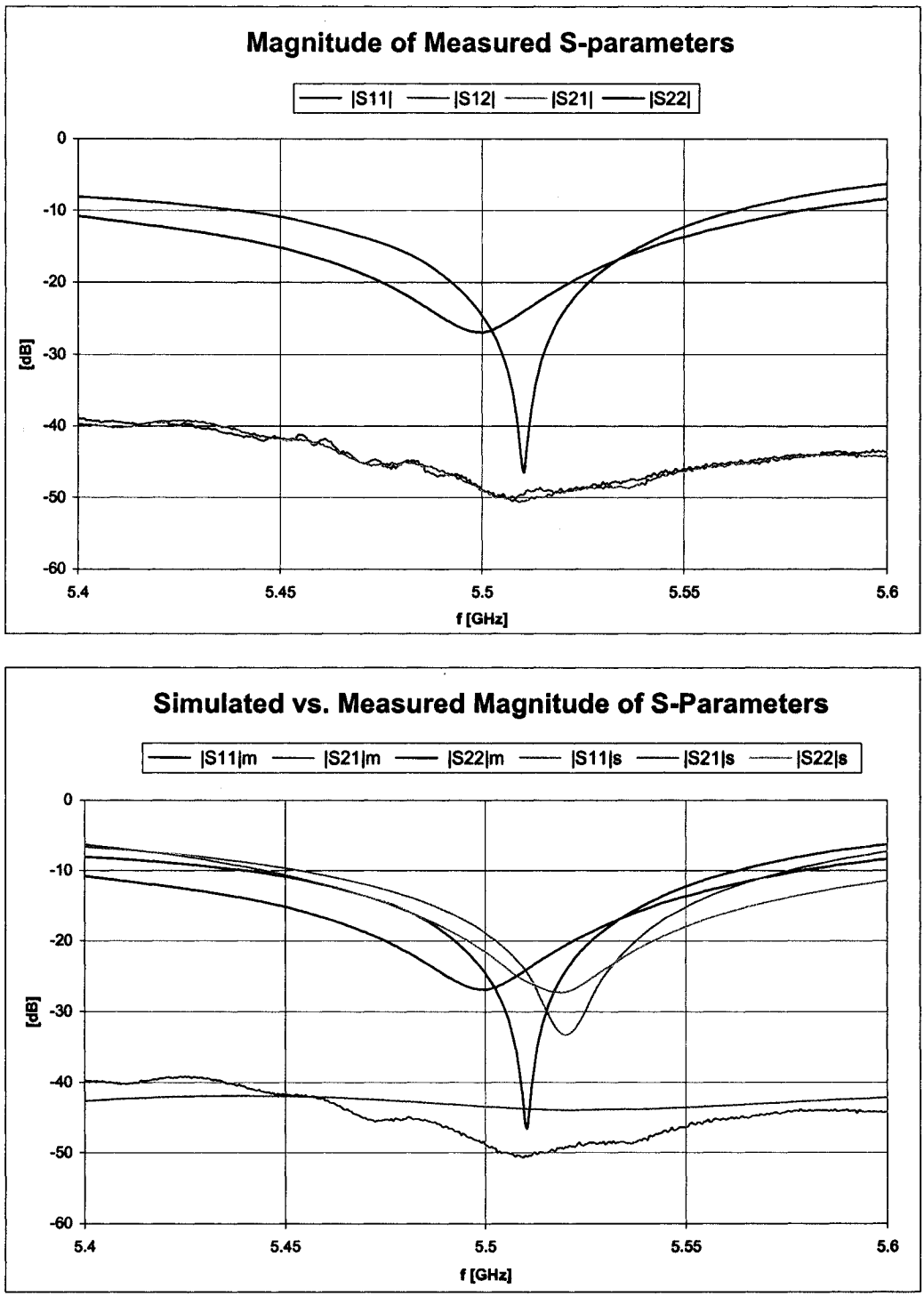

Figure 68 S-parameters for 4x4 dual-polarized microstrip array

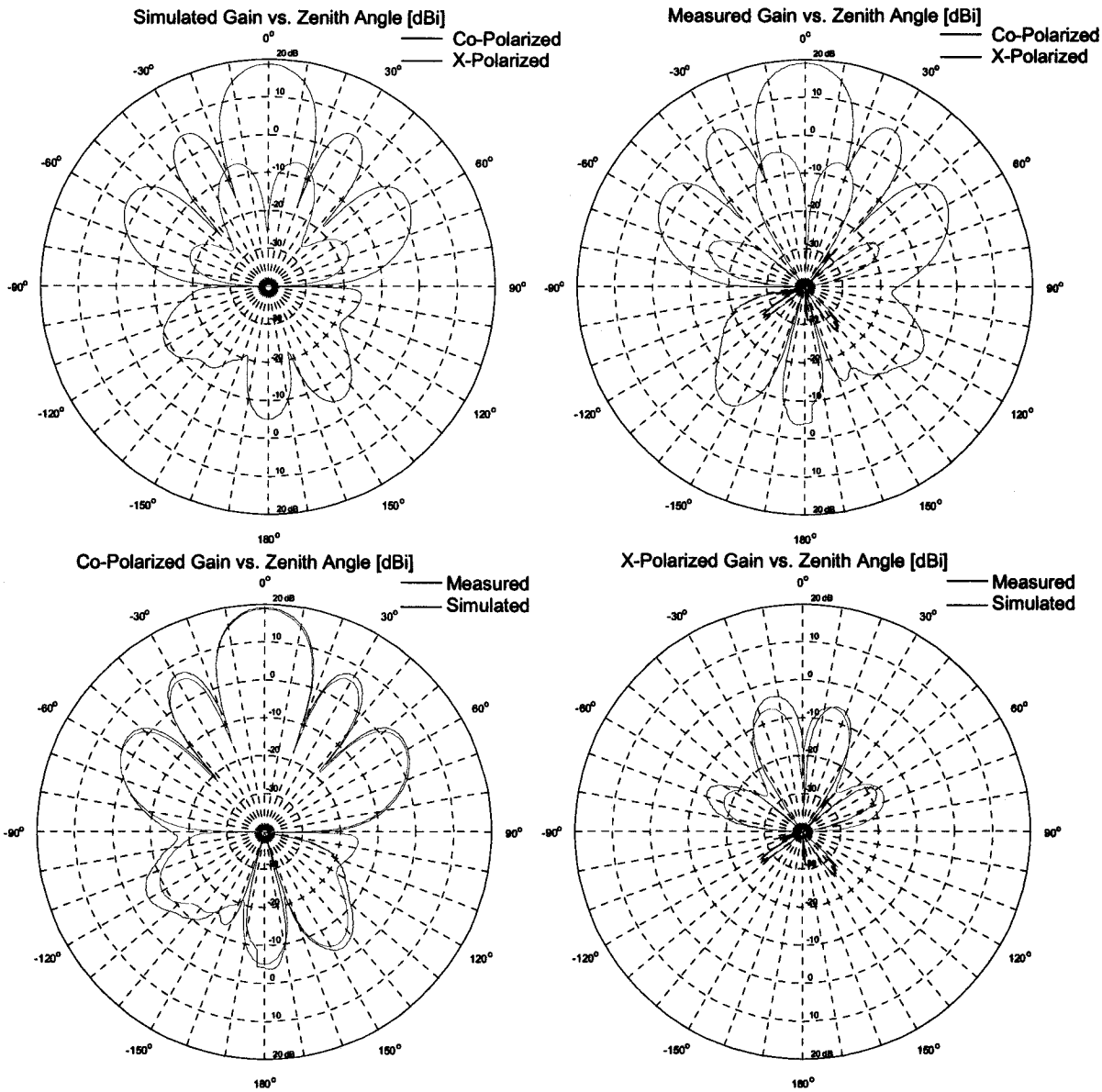

Figure 69 Measured and simulated aperture-coupled polarization E-plane radiation patterns of the 4x4 dual-polarized microstrip patch array

The results for radiation patterns in Figure 69 are summarized in Table 26.

Table 26 Summary of aperture-coupled polarization E-plane radiation pattern parameters of the 4x4 dual-polarized microstrip patch array

	3dB Beamwidth	Max X-Pol Level ($\|\theta\| \leq 60°$)	Front to Back Ratio	Back Lobe ($\|\theta\| \geq 120°$)
Simulated	18°	-25.4dB @ 16°	23.9dB	-23.9dB @ 180°
Measured	18°	-22.7dB @ 13°	23.3dB	-22.3dB @ -145°

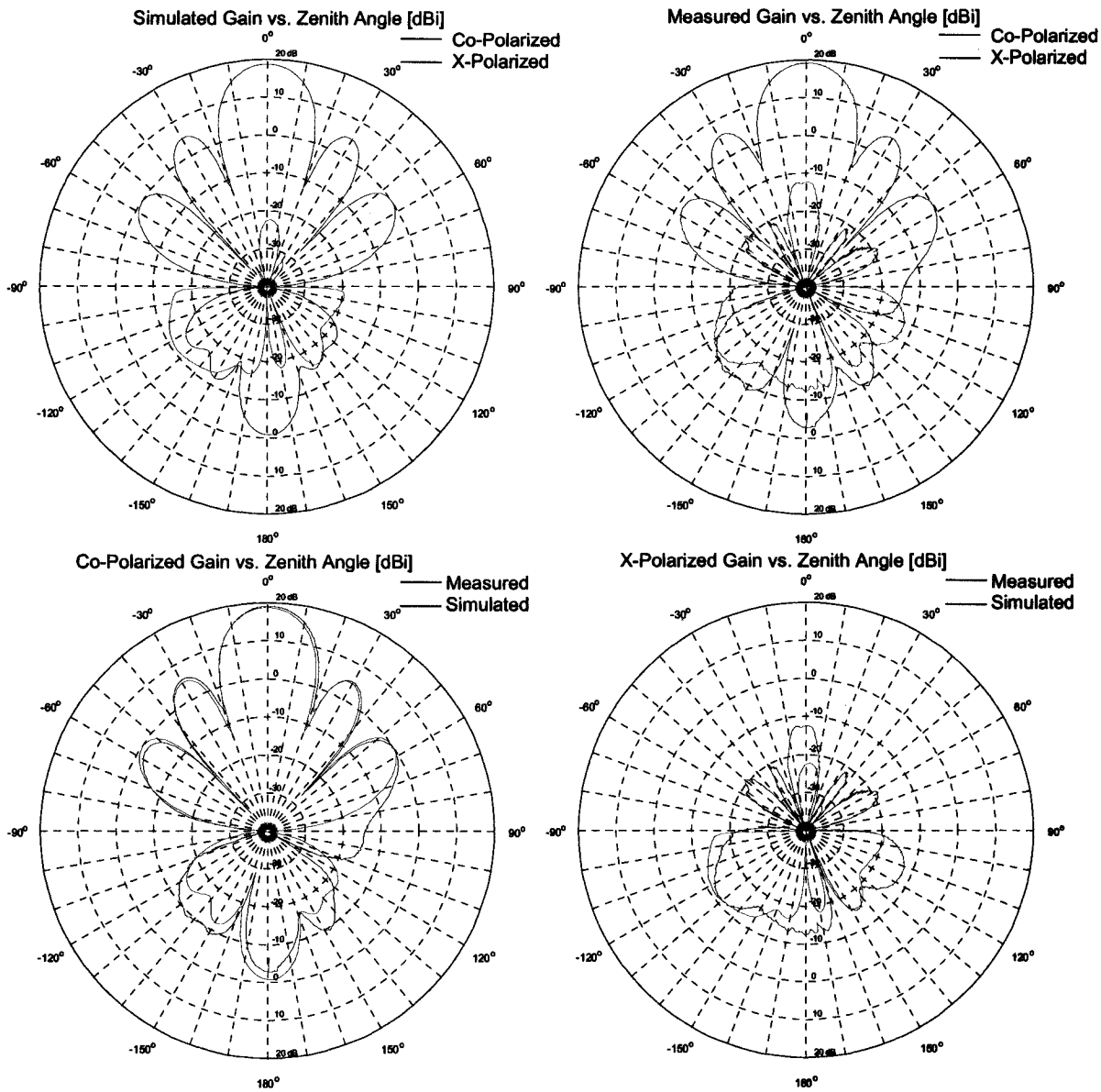

Figure 70 Measured and simulated aperture-coupled polarization H-plane radiation patterns of the 4x4 dual-polarized microstrip patch array

The results for radiation patterns in Figure 70 are summarized in Table 27.

Table 27 Summary of aperture-coupled polarization H-plane radiation pattern parameters of the 4x4 dual-polarized microstrip patch array

	3dB Beamwidth	Max X-Pol Level ($\|\theta\| \leq 60°$)	Front to Back Ratio	Back Lobe ($\|\theta\| \geq 120°$)
Simulated	18°	-40.9dB @ 3°	19.7dB	-19.7dB @ 180°
Measured	18°	-31.3dB @ 3°	22.2dB	-22.2dB @ 180°

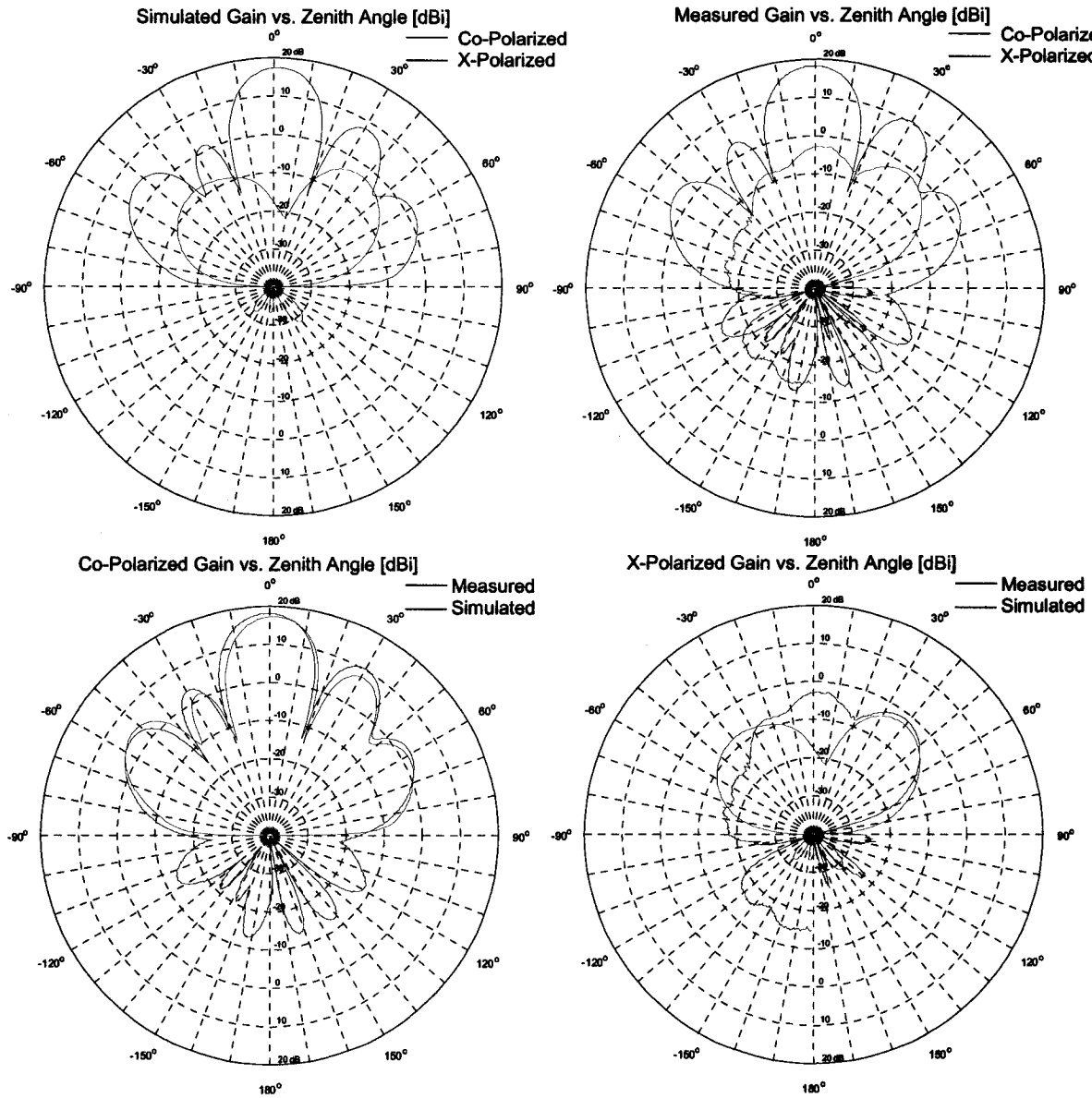

Figure 71 Measured and simulated edge-coupled polarization E-plane radiation patterns of the 4x4 dual-polarized microstrip patch array

The results for radiation patterns in Figure 71 are summarized in Table 28.

Table 28 Summary of edge-coupled polarization E-plane radiation pattern parameters of the 4x4 dual-polarized microstrip patch array

	3dB Beamwidth	Max X-Pol Level ($\|\theta\| \leq 60°$)	Front to Back Ratio	Back Lobe ($\|\theta\| \geq 120°$)
Simulated	18°	-20.2dB @ 39°	54.1dB	-54.1dB @ 180°
Measured	18°	-19.6dB @ 39°	40.0dB	-29.9dB @ 120°

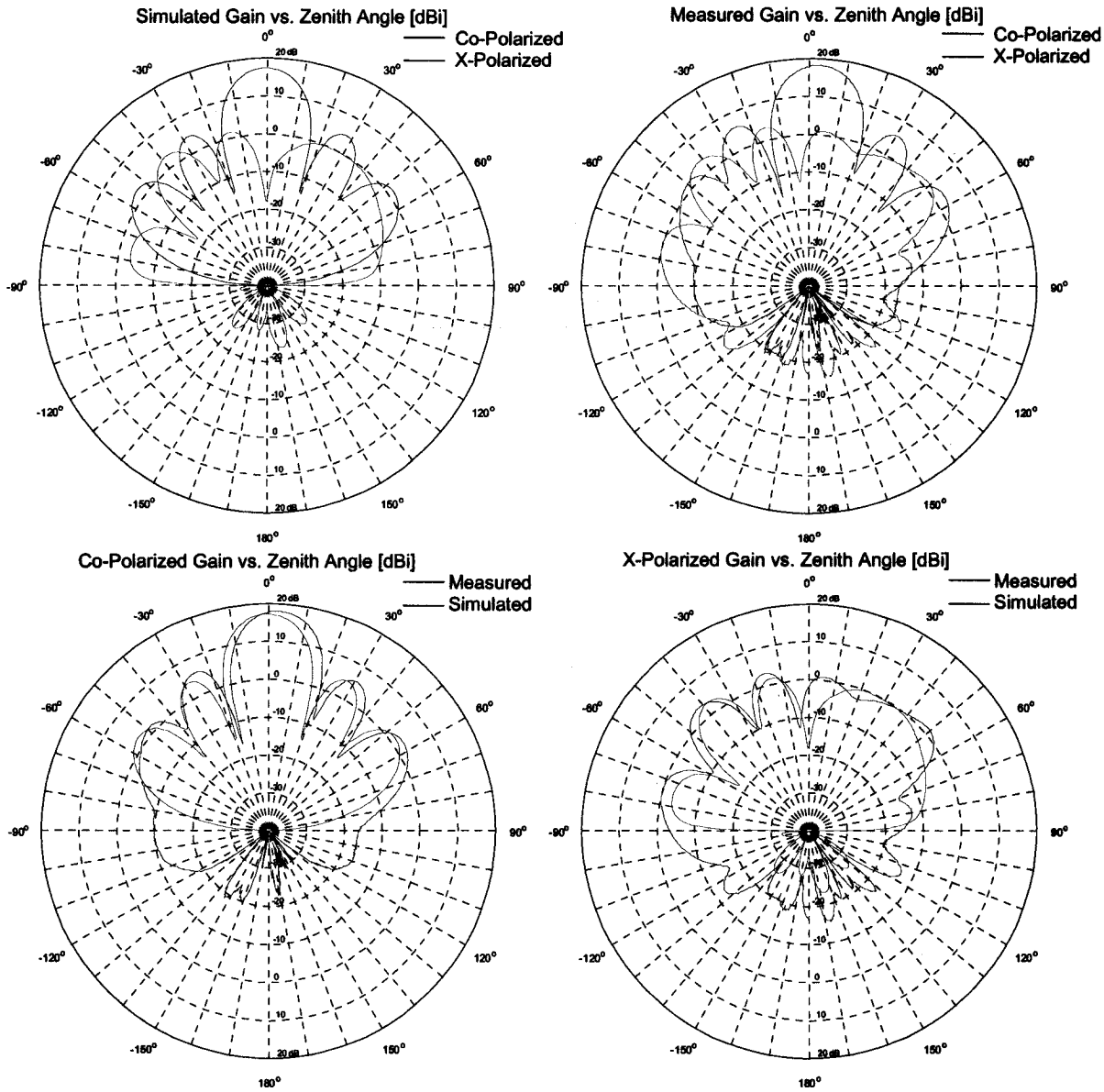

Figure 72 Measured and simulated edge-coupled polarization H-plane radiation patterns of the 4x4 dual-polarized microstrip patch array

The results for radiation patterns in Figure 72 are summarized in Table 29.

Table 29 Summary of edge-coupled polarization H-plane radiation pattern parameters of the 4x4 dual-polarized microstrip patch array

	3dB Beamwidth	Max X-Pol Level ($\|\theta\| \leq 60°$)	Front to Back Ratio	Back Lobe ($\|\theta\| \geq 120°$)
Simulated	18°	-14.7dB @ -38°	63.0dB	-53.5dB @ -140°
Measured	18°	-14.5dB @ -48	60.3dB	-37.5dB @ -145°

4.4 Benefits of Two Different Feed Mechanisms Implementation

The dual aperture-coupled patch will produce a good cross-polarization performance; however the coupling between the feed lines, which are on the same level, will affect the port isolation and present difficulties in the integration into an array. To avoid having feed networks for both polarization on the same level, the additional layer of substrate can be added and fork-shaped feed lines in the coupling region can be implemented in order to further minimize the interaction between the feed networks at the expense of the increased design complexity (in our case increase in design complexity was not justifiable, and therefore the dual-aperture approach was abandoned).

The dual edge-coupled patch will produce good port isolation levels but the cross-polarization levels will increase because of the radiation of the feed lines and coupling between the radiating element and the feed lines. The advantage of this feed mechanism lies in its simplicity; however the fact the feed lines are on the same level introduces difficulties in the integration of these dual-polarized elements into antenna array configuration.

The dual probe-coupled patch will produce excellent isolation levels and good cross-polarization performance due to the physical isolation between the coaxial feeds. There will be no feed radiation to interfere with either port isolation or cross-polarization levels. The problem with this configuration is the complexity of the fabrication process that is complicated by the presence of vias necessary for this type of feed coupling, and the impossibility of integration into arrays using planar feed network methods.

So far we have discussed the dual-polarized elements excited with like methods of feed coupling. We have seen that the problem of low port isolation performance arose when the transmission lines of both feed networks were placed on the same physical level. The solution to this problem is to combine two different feed mechanisms, which will have feed networks on different levels like edge-coupled feed and aperture-coupled feed mechanisms.

The transmission lines in the aperture-coupled feed network are separated from the radiating element and the edge feed network by the groundplane eliminating the coupling between the two feed networks. The transmission lines used in the edge-coupled feed network are on the same level as the radiating elements allowing the radiation from the feed

network to contribute to an increase in the cross-polarization levels. The coupling between the feed network and the radiating elements will affect the port isolation levels. The feed networks are located on the separate levels making it possible to easily integrate this dual-polarized element into an antenna array. Using the edge and aperture feed coupling mechanisms we have reduced the number of elements susceptible to unwanted cross-coupling between the orthogonal polarizations to radiating element alone, and achieved port isolation of 50dB with the 4x4 element array which is a 15dB improvement over the single type coupling mechanism arrays presented in Chapter 2.

Having the feed networks on separate layers allows us to implement corporate feed network for each of the orthogonal polarizations. This in turn enables us to design, with a greater degree of freedom, features such as excitation amplitude taper and phase progression to achieve sidelobe suppression and beam squinting. Also, it is possible to achieve an increase in the port isolation levels by applying certain combinations of horizontal and vertical excitation amplitude taper and phase progression.

4.5 The Effects of the Excitation Amplitude Taper and Phase Progression

The excitation amplitude taper is the most commonly used method in sidelobe suppression. Depending on the kind of the taper employed an antenna designer can alter the sidelobe levels in order to meet the design specification. Since we are dealing with dual-polarized microstrip arrays we want to examine the effects the excitation amplitude taper has on the port isolation performance of the array. Planar arrays are two-dimensional structures and can have excitation amplitude taper in both horizontal and vertical direction. It is possible to implement horizontal and vertical excitation amplitude taper for either of the orthogonal polarizations. In our case we will concentrate on the horizontal and vertical excitation amplitude taper implemented in the vertically polarized aperture-coupled feed network of the 4x4 element microstrip array. We will observe the effect on the port isolation level due to the amplitude taper given in Figure 74.

To obtain the plot in Figure 74 the 4x4 array is converted into a 17-port network shown in Figure 73 and S-parameters for this network were obtained.

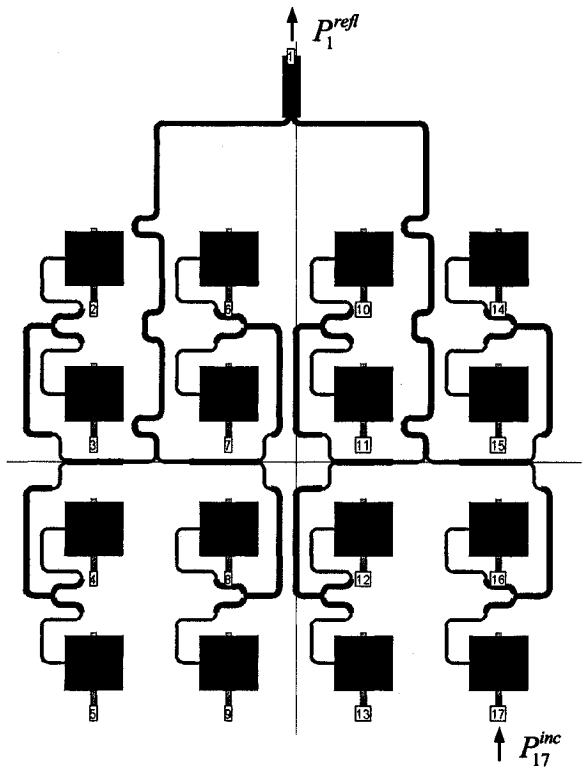

Figure 73 Excitation amplitude taper and phase progression numerical experiment geometry

All ports of the structure are 50Ω ports. Power incident on n^{th} port is given by $P_n^{inc} = \frac{|V_n^+|^2}{2Z_0}$, power reflected from the n^{th} port is given by $P_n^{refl} = \frac{|V_n^-|^2}{2Z_0}$, power accepted by the n^{th} port is then $P_n^{inc} - P_n^{refl}$. The relationship between the reflected and incident voltage waves is given by $[V^-] = [S][V^+]$. Ports 2 through 17 excite vertical polarization. For the purpose of our experiment port 1 is not excited and it is terminated in 50Ω load. The isolation between the orthogonally polarized signals is given by 4.3.3-1.

$$Iso = -10\log\frac{P_1^{refl}}{\sum_{n=2}^{17} P_n^{inc}} = -10\log\frac{|V_1^-|^2}{\sum_{n=2}^{17}|V_n^+|^2} = -10\log\frac{\left|\sum_{n=2}^{17} S_{1n}V_n^+\right|^2}{\sum_{n=2}^{17}|V_n^+|^2} \qquad 4.3.3\text{-}1$$

To implement the excitation amplitude taper we simply excited each of the aperture-coupled ports by signals of appropriate amplitude. The port isolation for various amounts of

excitation amplitude taper of the aperture-coupled signal is shown in Figure 74. In the section on Element Grouping and from the Figure 57 we have seen that the cancellation of the cross-coupling contributions from the ports symmetrical with respect to the horizontal axis of the geometry relies on the symmetry of the antenna geometry. Also the meandering of the non-mirrored vertical portion of the edge-coupled feed line is optimized under the condition of uniform amplitude excitation and zero phase progression. By implementing vertical excitation taper or phase progression the symmetry will be disturbed and the meandering of the non-mirrored vertical feed line will no longer provide optimal cancellation of the cross-coupling contributions from these ports resulting in the degradation of the port isolation performance. Similar effect was expected when horizontal taper was implemented but to our surprise the port isolation performance improved instead of getting worse. The graphical representation of the excitation amplitude taper effects on port isolation is given in Figure 74.

To implement the excitation phase progression each port was excited by signals with appropriate phase progression. When the vertical phase progression was implemented the port isolation performance suffered, however for certain combinations of horizontal and vertical phase progression the port isolation performance gets significantly improved. The effects of the phase progression on the port isolation are shown in Figure 75.

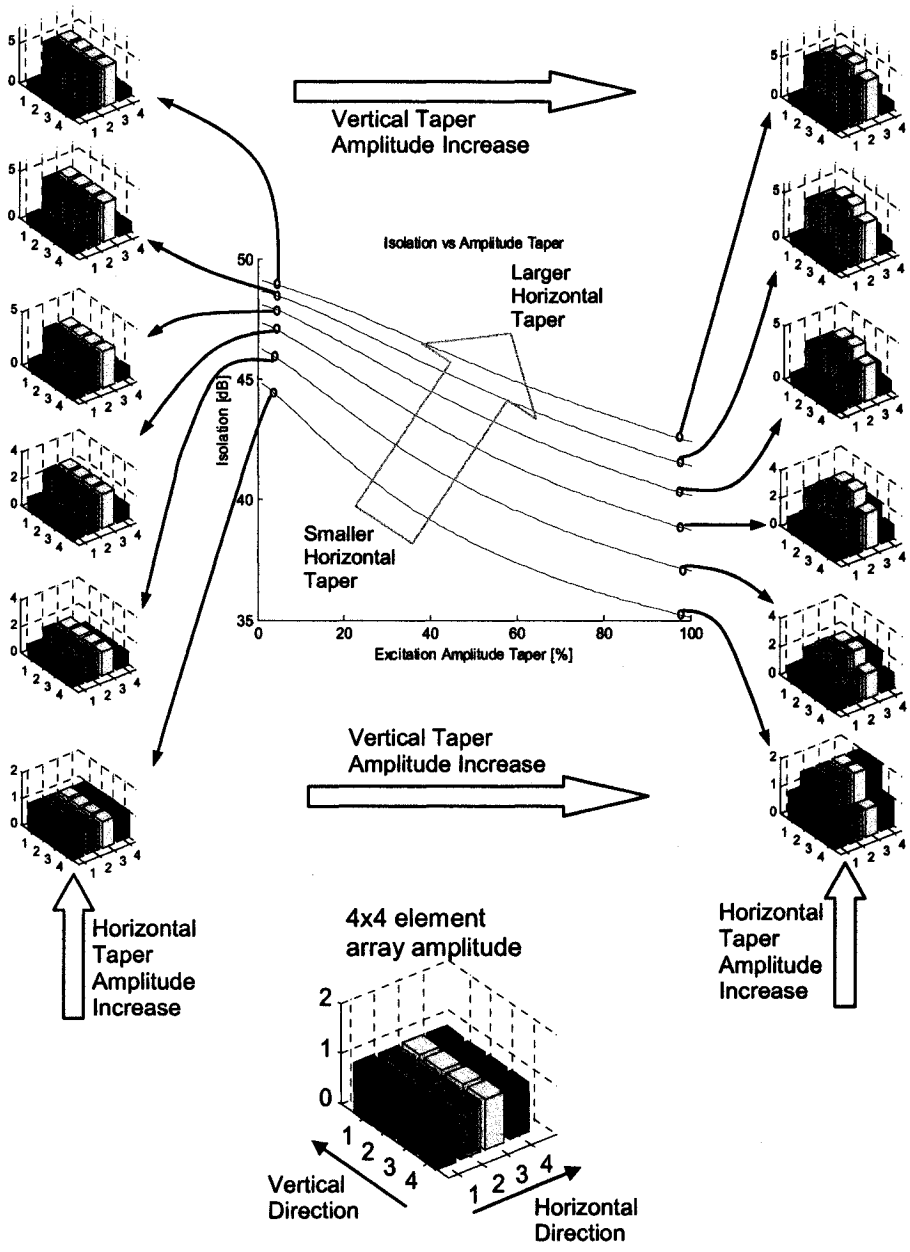

Figure 74 Effects of excitation amplitude taper on port isolation performance

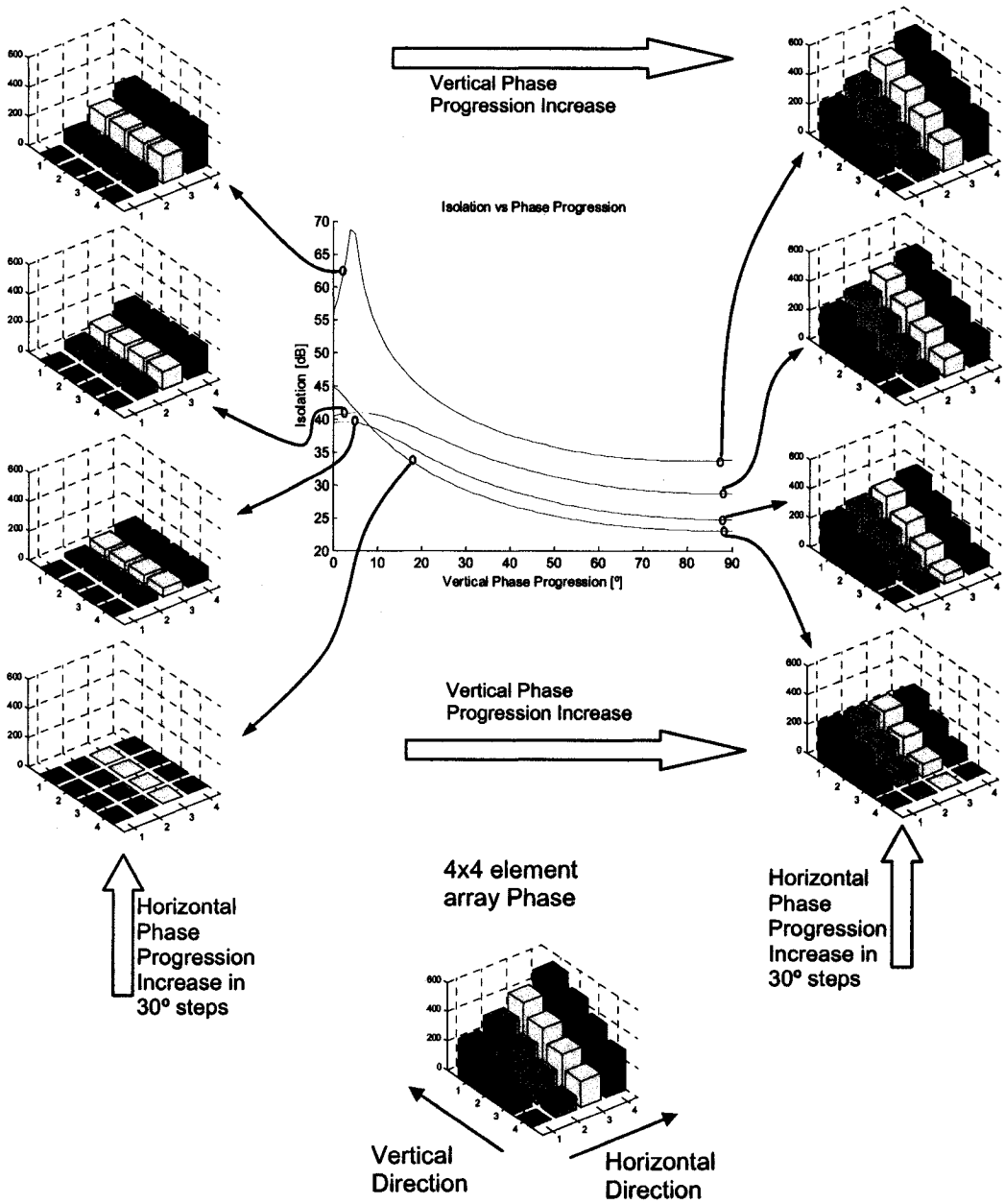

Figure 75 Effects of excitation phase progression on port isolation performance

In the future we will investigate effects of simultaneously implementing the excitation amplitude taper and the phase progression along the vertical and the horizontal axis of the geometry for both the vertical and the horizontal polarization.

4.6 Near Field Comparisons and Possible Design Clues

Throughout the thesis we used S-parameters to characterize dual-polarized microstrip antennas, or more specifically to evaluate the port isolation between orthogonally polarized ports. The performance of the antenna prototypes expressed via S-parameters allowed for the optimization of the antenna geometry that led to a successful design. However, the S-parameters only provide an insight into the performance of the geometry under test by lumping the effects of all constituent parts of the geometry into a single complex number. The cumulative nature of such an analysis confines the designer to an optimization routine that allows the change of one aspect of the geometry at the time and does not provide indication to specific parts of the geometry that require modification to achieve a desired performance.

To obtain some spatial indication about how to route certain portions of the antenna feed network we used the magnetic field calculated in the vicinity of the desired portion of the feed network. In Section 4.2.3 we determined that non-mirrored vertical portions of the edge-coupled feed network have detrimental effects on the port isolation unless special precautions are taken, therefore the non-mirrored vertical section of the feed network was a perfect candidate for testing the usefulness of the analysis technique described below.

The reference magnetic field is obtained from the layout without the non-mirrored vertical portion of the edge-coupled feed (Figure 57). Only the vertical port of the array is excited which sets up vertically oriented currents on the patches. In the case of the reference geometry there is no metallization in the region of interest and the magnetic field observed is due to the vertically oriented current distribution on the radiating patches. Since we were interested in the current flow along the transmission line we will create a spatial magnitude plot of the component of the magnetic field tangential to the surface of the conductor and perpendicular to the current direction. The magnitude of the x-component of the magnetic field is calculated for all the points of the substrate surface delimited by the red rectangle in the Figure 76.

In order to provide comparison between the case with and the case without the non-mirrored section of the feed network we point-wise normalized the magnitude of the x-component of the magnetic field of the geometry with the transmission line metallization by the magnitude of the corresponding field component for the geometry without the metallization and obtained the 2D plot in Figure 76. The red regions on the plot indicate that the magnetic field x-component of the structure with metallization has higher magnitude than the reference field; the blue regions indicate the opposite situation.

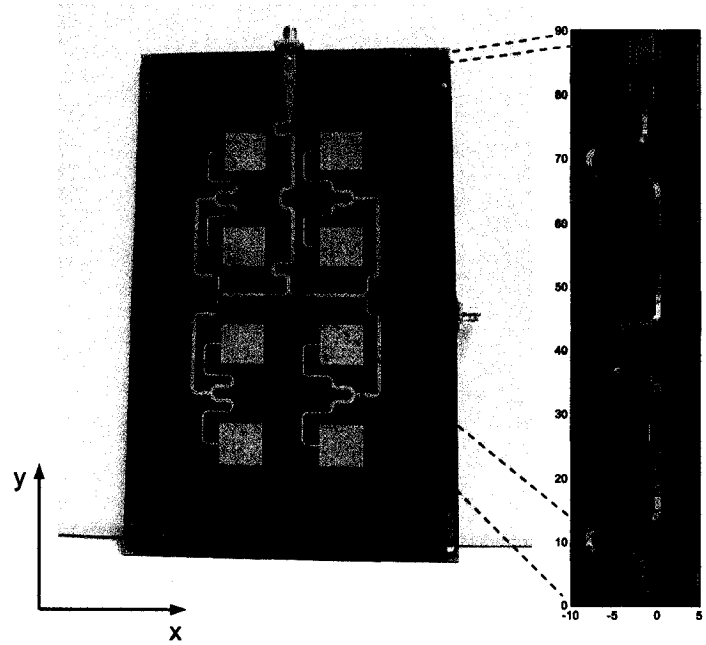

Figure 76 Normalized x-component of the magnetic field at the surface of the substrate

Normalized plots of the x-component of the magnetic field for various geometry layouts compared to the reference field obtained for the geometry with no metallization in the region of interest are shown in Figure 77. The reference magnetic field would induce a current in the metallization if there were any present (Figure 57). The only metallization that we intend to put in the space between the radiating elements is the transmission line which will start guiding the coupled energy instead of reradiating it into space. The coupling contributions picked up at one section of the line might combine constructively or destructively with contributions from another section depending on the phase and magnitude of the individual contributions which in turn depend on the geometry of the

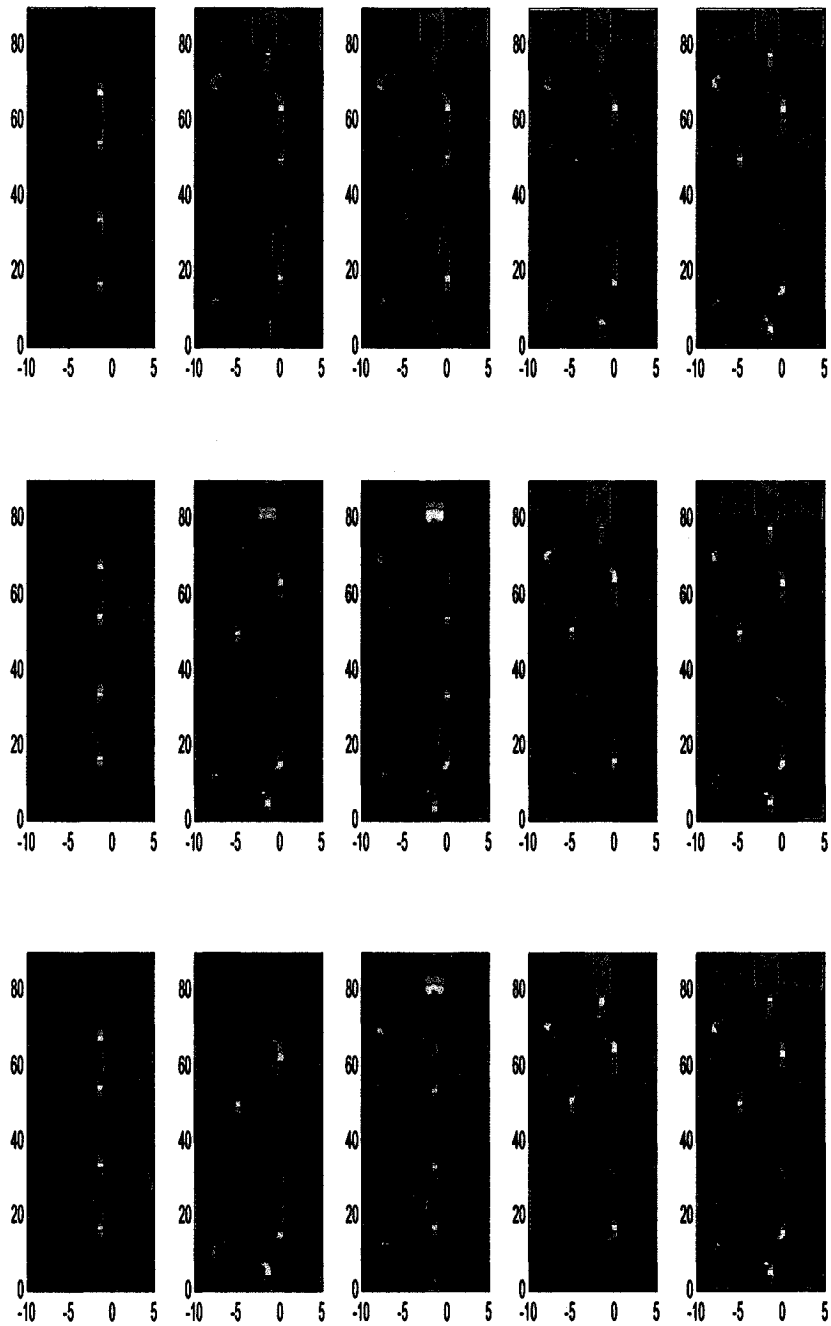

Figure 77 Normalized x-component magnitude of the test magnetic field

radiating element, the placement of the elements within the array and the geometry of the feed network transmission line passing between the elements. Since we cannot change the geometry of the radiating element or the lattice of the array without affecting the radiation patterns we altered the routing of non-mirrored section of the feed network transmission

line in order to achieve destructive combining of the cross-coupling contributions from neighboring radiating elements to the feed network. By analyzing plots in Figure 77 an antenna designer can directly observe the effects produced by altering the routing of the feed network transmission line and devise a layout that maximizes the port isolation performance of the array. The best meandering shape would need to be determined through an automated optimization process. The meandering presented in the rightmost column of the Figure 77 represents the best performing meandering of the non-mirrored feed network section we obtained in the course of the design process.

Since the magnitude of the magnetic field tangential to the conductor is proportional to the electric current magnitude we can reach some conclusions about the isolation performance of the feed network layout under test compared to the reference case which exhibited satisfactory isolation performance. This method is useful in the integration of sub-array segments into full sized arrays. The horizontal section of the feed network connecting two sub arrays is almost perfectly aligned with a null of the x-component of the magnetic field obtained in the simulation of the 2x4 array with an extended non-mirrored vertical section of the feed network. A significant deviation from this position may result in lower port isolation levels for a 4x4 array. The simulated field distribution of the extended version is superimposed on the physical layout as shown in Figure 78. Further investigation into the reliability of this type of analysis might prove its usefulness.

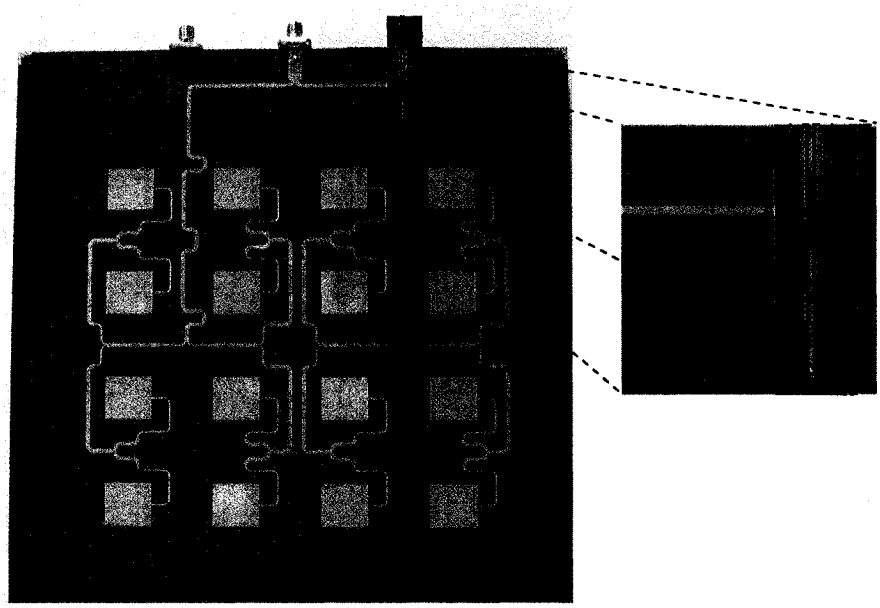

Figure 78 Normalized x component of the magnetic field in the vicinity of the meandered portion of the feed network

4.7 Concluding Remarks

We identified and discussed the aspects of the antenna geometry that cause the decrease in the port isolation. From the analysis of the radiating element positioning, the radiating element grouping and the effects of non-mirrored vertical sections of the edge-coupled feed network on port isolation, we managed to draw the conclusions that led to a successful design of the 2x4 dual-polarized sub-array with port isolation exceeding 40dB over the impedance bandwidth. An excellent agreement between the measured and simulated results was observed indicating that our port isolation enhancing techniques are viable. We used a 2x4 sub-array as a building block to obtain the 4x4 dual-polarized array with expectations to retain the good port isolation performance exhibited by its 2x4 sub-array building blocks. The measured port isolation for the 4x4 element array was better than 50dB at resonance exceeding the port isolation performance of its 2x4 element sub-array building block. The measured port isolation of the 4x4 element array surpassed the targeted port isolation specification of 40dB over the impedance bandwidth by a margin of up to 10dB. Again, the measurements matched simulated results to a high degree thus increasing our confidence that manufacturable designs of even larger arrays may be obtained through "fine tuning" done using a full-wave electromagnetic simulator. The effects of the excitation amplitude taper and phase progression were examined. Depending on the amount of excitation amplitude taper and phase progression, and the axis along which they are implemented we found that the port isolation can be significantly degraded or improved. It was also discovered that the negative effects on port isolation of the amplitude taper and phase progression along one axis can to some extent be cancelled by applying proper amplitude taper and phase progression along the orthogonal axis thus providing a designer with another degree of freedom in the design procedure.

References

[24] A. Petosa, "Antenna and Arrays", ELEC 5607 Course Notes, Spring 2005, Carleton University, Ottawa, Canada

[25] J. Kim and F. S. Barnes, "Dielectric Slab Rotman Lens with Tapered Slot Antenna Array", IEE Proc.-Microw. Antennas Propag. Vol. 152, No. 6, December 2005

[26] Ronald D. Esman, Michael Y. Frankel, J. L. Dexter, L. Goldberg, M. G. Parent, D. Stilwell, and D. G. Cooper, "Fiber-Optic Prism True Time-Delay Antenna Feed", IEEE Photonics Technology Letters, Vol. 5, No. 11, p1347-1349, November 1993

Chapter 5

Conclusions

The port isolation performance of existing dual-polarized microstrip patches ranges from 25dB to 40dB and for the arrays between 19dB and 35dB. In Chapter 3 we have shown that using two different feeding mechanisms and implementing specific routing of the feed network are important techniques for increasing the port isolation of a dual-polarized microstrip patch. We have devised a dual-polarized microstrip radiating element with a feed line geometry that does not significantly degrade port-to-port isolation by its presence, and yet is compatible for use in an array environment. Three geometries were designed, built, and measured and the performance was studied through the comparison to that of an idealized element (which does not permit incorporation into an array) and a "simplistic" element which simply bends the feed lines of the idealized element in order to force it to into the planar array layout. Proper routing of the element feed lines in the vicinity of the patch was found to be essential. Comparison between the measured and simulated results was shown to be excellent. This allowed us to conclude that the effects of altering the feed line routing observed during simulations were not due to the peculiarities of the computational electromagnetics method used but are indeed physically real. We were able to infer why the new array-compatible element provides a port isolation performance that is better than that of the poorly-performing simplistic element and only slightly worse than the idealized (but impractical) element, and then utilized the electromagnetic simulator in a rather novel way to verify this conjecture. The best performance is exhibited by the element with straight feeds with the measured port isolation performance better than $44dB$ over the $1GHz$ span centered at $5.5GHz$.

The worst performance was measured for the "simplistic" element with a single bend in the edge-coupled feed with port isolation performance better than $16dB$ over the $1GHz$ span centered at $5.5GHz$. The measured port isolation performance for the element with folded edge-coupled feed was found to be better than $36dB$ over the impedance bandwidth which is about $7dB$ lower port isolation performance than that of the idealized element with the straight feed. Radiating element with the folded edge-coupled feed can be readily integrated

into an array thus combining the good port isolation observed in the case of the element with the straight feed with an array compatible geometry.

In Chapter 4 we identified and discussed the aspects of the antenna geometry that cause the degradation in the port isolation performance. From the analysis of the radiating element positioning, the radiating element grouping and the effects of non-mirrored vertical sections of the edge-coupled feed network on port isolation, we managed to draw the conclusions that led to successful design of the 2x4 dual-polarized sub-array with port isolation exceeding 40dB over the impedance bandwidth. We used a 2x4 sub-array as a building block to obtain the 4x4 dual-polarized array with expectations to retain the good port isolation performance exhibited by its 2x4 sub-array building blocks. The measured port isolation for the 4x4 element array was better than 50dB at resonance exceeding the port isolation performance of its 2x4 element building block (port isolation bandwidth-wise). The measured port isolation of the 4x4 element array surpassed the targeted port isolation specification of 40dB over the impedance bandwidth with up to 10dB of margin. The measurements matched simulated results to a high degree thus increasing our confidence that manufacturable designs of even larger arrays may be obtained through "fine tuning" done using a full-wave electromagnetic simulator.

Depending on the amount of excitation amplitude taper and phase progression, and the axis along which they are implemented we found that the port isolation can be significantly degraded or improved. It was also discovered that the negative effects on port isolation of the amplitude taper and phase progression along one axis can be cancelled to some extent by applying proper amplitude taper and phase progression along the orthogonal axis thus providing a designer with another degree of freedom in the design procedure.

The main contributions within the thesis are:

- The design of a high port isolation single dual-polarized microstrip radiating element with the matching network that can be integrated into an array was presented
- The dual-polarized array design with corporate feed network implementation for each polarization was demonstrated.
- The geometry sections of the critical importance for a high port isolation performance of the array were identified and the guidelines for an effective design of these sections were proposed.
- The effects of the excitation amplitude taper and the phase progression on the port isolation performance of the array were analyzed and the guidelines for the excitation amplitude taper and phase progression that yield higher port isolation performance were presented.
- The spatial analysis of the feed network geometry in search for design clues based on the analysis of the near fields was suggested as future research.

The future work suggestions include:

- Further investigation of cross-coupling effects that diminish the port isolation.
- Increasing the impedance bandwidth of the array from 2.7% to around 10% while maintaining high port isolation performance. The increase in impedance bandwidth is to be accomplished by adding vertically-stacked parasitic patches. In an attempt to increase the impedance bandwidth of the array we would also test the robustness of the port isolation enhancement techniques introduced in this thesis and their sensitivity to geometry modifications such as parasitic patch stacking.
- Once a good understanding of the cross-coupling mechanisms is obtained and the port isolation degradation mitigating techniques are fully developed a design algorithm can be devised that would optimize the feed network routing to maximize the port isolation and the whole design process could be automated.